SANDIA REPORT

SAND2014-0712
Unlimited Release
Printed January 2014

SMART Wind Turbine Rotor: Data Analysis and Conclusions

Jonathan C. Berg, Matthew F. Barone, and Nathanael C. Yoder

Prepared by
Sandia National Laboratories
Albuquerque, New Mexico 87185 and Livermore, California 94550

Sandia National Laboratories is a multi-program laboratory managed and operated by Sandia Corporation, a wholly owned subsidiary of Lockheed Martin Corporation, for the U.S. Department of Energy's National Nuclear Security Administration under contract DE-AC04-94AL85000.

Approved for public release; further dissemination unlimited.

Issued by Sandia National Laboratories, operated for the United States Department of Energy by Sandia Corporation.

NOTICE: This report was prepared as an account of work sponsored by an agency of the United States Government. Neither the United States Government, nor any agency thereof, nor any of their employees, nor any of their contractors, subcontractors, or their employees, make any warranty, express or implied, or assume any legal liability or responsibility for the accuracy, completeness, or usefulness of any information, apparatus, product, or process disclosed, or represent that its use would not infringe privately owned rights. Reference herein to any specific commercial product, process, or service by trade name, trademark, manufacturer, or otherwise, does not necessarily constitute or imply its endorsement, recommendation, or favoring by the United States Government, any agency thereof, or any of their contractors or subcontractors. The views and opinions expressed herein do not necessarily state or reflect those of the United States Government, any agency thereof, or any of their contractors.

Printed in the United States of America. This report has been reproduced directly from the best available copy.

Available to DOE and DOE contractors from
U.S. Department of Energy
Office of Scientific and Technical Information
P.O. Box 62
Oak Ridge, TN 37831

Telephone: (865) 576-8401
Facsimile: (865) 576-5728
E-Mail: reports@adonis.osti.gov
Online ordering: http://www.osti.gov/bridge

Available to the public from
U.S. Department of Commerce
National Technical Information Service
5285 Port Royal Rd.
Springfield, VA 22161

Telephone: (800) 553-6847
Facsimile: (703) 605-6900
E-Mail: orders@ntis.fedworld.gov
Online order: http://www.ntis.gov/help/ordermethods.asp?loc=7-4-0#online

SAND2014-0712
Unlimited Release
Printed January 2014

SMART Wind Turbine Rotor:
Data Analysis and Conclusions

Jonathan C. Berg and Matthew F. Barone
Wind Energy Technologies Department
Sandia National Laboratories
P.O. Box 5800
Albuquerque, New Mexico 87185-MS1124

Nathanael C. Yoder
ATA Engineering
11995 El Camino Real, Suite 200
San Diego, California 92130

Abstract

The Wind Energy Technologies department at Sandia National Laboratories has developed and field tested a wind turbine rotor with integrated trailing-edge flaps designed for active control of the rotor aerodynamics. The SMART Rotor project was funded by the Wind and Water Power Technologies Office of the U.S. Department of Energy (DOE) and was conducted to demonstrate active rotor control and evaluate simulation tools available for active control research. This report documents the data post-processing and analysis performed to date on the field test data.

Results include the control capability of the trailing edge flaps, the combined structural and aerodynamic damping observed through application of step actuation with ensemble averaging, direct observation of time delays associated with aerodynamic response, and techniques for characterizing an operating turbine with active rotor control.

ACKNOWLEDGMENTS

The SMART rotor project was funded by the U.S. Department of Energy (DOE) Wind and Water Power Technologies Office (director Jose Zayas) under the office of Energy Efficiency and Renewable Energy (EERE, assistant secretary David Danielson).

The authors gratefully acknowledge all those who contributed to this project, including the following:

USDA-ARS staff at Bushland Test Site

- Adam Holman
- Byron Neal

Testing

- Wesley Johnson
- Bruce LeBlanc
- Nate Yoder (ATA Engineering)

Data Acquisition System programming

- Juan Ortiz-Moyet (Prime Core)

Blade Modification

- David Calkins
- Mike Kelly
- Bill Miller

Blade Manufacture by TPI Composites

SMART blade design

- Matt Barone
- Dale Berg
- Jonathan Berg
- Gary Fischer
- Josh Paquette
- Brian Resor
- Mark Rumsey
- Jon White

Consultation

- Derek Berry (TPI Composites)
- Mike Zuteck (MDZ Consulting)

CONTENTS

Executive summary 9

1. Introduction 13
    1.1 Motivation 13
    1.2 SMART Rotor Experiments 14
    1.3 Structure of This Report 15

2. Aeroelastic Modeling 17
    2.1 Aerodynamic Modeling Considerations for SMART Rotors 17
        2.1.1 Time Scales 17
        2.1.2 Unsteady Aerodynamics 19
    2.2 Aerodynamic Model Choices for SMART Rotors 20
        2.2.1 Blade Sectional Models 21
        2.2.2 Rotor Wake Models 22
    2.3 Conclusions 25

3. Field Test Data Analysis 27
    3.1 Flap Control Capability 27
    3.2 Time-Average Response to Step Actuation 29
    3.3 Rotor Dynamics 36
        3.3.1 Sine Sweep with Rotor Stopped 36
        3.3.2 Sine Sweep during Power Production 37
    3.4 Flap Drive System Dynamics 39
        3.4.1 Flap Drive with Rotor Stopped 39
        3.4.2 Flap Drive during Power Production 44
    3.5 Power Curves 47
    3.5 Conclusions 50

4. Data Acquisition System 51
    4.1 Introduction 51
    4.2 Channel List 52
    4.3 Time Synchronization 56
    4.4 Data Dropouts 58

5. Data Post Processing 59
    5.1 Scale and Offset 59
    5.2 Coordinate Systems and Transformations 61
    5.3 Time-Synchronized Resampling 62

6. On-Ground Calibration 67
    6.1 Preliminary Blade Modal Properties 67
    6.2 Preliminary Beam Model Updating 69
    6.3 Blade Strain Calibrations 72

7. Blade Surface Geometry 75

8. References 81

Appendix A: ATLAS Configuration Settings 87

Distribution 94

FIGURES

Figure ES.1 The SMART rotor with photo inset of trailing edge flaps. 9
Figure ES.2 Average strain response showing flap control capability. 10
Figure ES.3 Logarithmic sweep excitation of flapwise acceleration frequencies. 11
Figure 3.1 Strain response tracking with flap step sequence. 28
Figure 3.2 Average strain response as a function of wind speed and flap angle.......................28
Figure 3.3 Ensemble average strain response to 20 degree flap step. 30
Figure 3.4 Detail of strain oscillations in step response. 30
Figure 3.5 Ensemble average generator power response to 20 degree flap step. 31
Figure 3.6 Ensemble average response of rotor fore-aft IMU to 20 degree flap step. 32
Figure 3.7 Ensemble average strain response at 6.75 m span. 33
Figure 3.8 Ensemble average generator power response. 34
Figure 3.9 Ensemble average rotor IMU response, fore-aft component. 35
Figure 3.10 Parked rotor spectrogram of flapwise acceleration with log sine sweep. 36
Figure 3.11 Parked rotor PSD of flapwise acceleration with log sine sweep excitation. 37
Figure 3.12 Power production spectrogram of flapwise acceleration with log sine sweep. 38
Figure 3.13 Power production PSD of flapwise acceleration with log sine sweep excitation. ...38
Figure 3.14 Sequence of video frames showing blade tip motion during one flap cycle. 39
Figure 3.15 Motor current demand during sinusoidal flap motion at 1 Hz. 40
Figure 3.16 Flap drive simulation with primarily Coulomb damping. 42
Figure 3.17 Flap drive simulation with primarily viscous damping. 42
Figure 3.18 Flap drive simulation with numerical instability at two points. 42
Figure 3.19 Motor shaft angle response to log frequency sweep. 43
Figure 3.20 Amplitude gain and phase shift between motor shaft response and command. 43
Figure 3.21 Amplitude gain and phase shift between motor current and shaft angle. 44
Figure 3.22 Motor current demand for various frequencies of sinusoidal motion. 45
Figure 3.23 Hinge moment coefficient at 7.8 m span. 46
Figure 3.24 Flap drive simulation with aerodynamic hinge moment included. 47
Figure 3.25 Power curve at 0 degree flap compared to unmodified rotor. 48
Figure 3.26 Power curve of each flap setting compared to 0 degree setting. 49
Figure 4.1 Example of samples acquired at different rates. 56
Figure 4.2 Example of sample rate determination. 57
Figure 5.1 Orientation of accelerometers with respect to blade coordinate system. 61
Figure 5.2 Pattern of residuals about straight-line fit to GPS time. 63
Figure 5.3 Schematic of subsystem clock delays and channel offsets. 64
Figure 6.1 Simple beam element model used to display the experimental mode shapes...........68
Figure 6.2 Edgewise blade pull on calibration fixture. 73
Figure 7.1 Creaform's handheld optical scanning system. 75
Figure 7.2 Point cloud from scan of entire blade surface. 75
Figure 7.3 Detail of SMART blade tip with flaps positioned at -20 degrees. 76
Figure 7.4 Comparison of chord distributions. 77
Figure 7.5 Comparison of twist distributions. 77
Figure 7.6 Cross sections at 3 meter span align almost perfectly. 78
Figure 7.7 Cross sections at 5 meter span show variation in thickness. 78
Figure 7.8 Cross sections at 7.2 meter span annotated with SMART blade alterations. 79

Figure 7.9 Cross sections at 7.9 meter span with variations annotated. 79

TABLES

Table 2.1 Time scales associated with AALC for the Sandia 115kW test turbine. 18
Table 3.1 Damped free vibration parameters calculated from strain response. 31
Table 4.1 Data acquisition subsystem channel groups. 53
Table 4.2 Channel List 54-55
Table 5.1 Summary of post-processing offsets and multipliers. 60
Table 5.2 Mapping of accelerometer channels to blade coordinate system. 61
Table 5.3 Subsystem sample periods in seconds. 62
Table 5.4 Channel offsets relative to subsystem clocks. 65
Table 6.1 Free-free natural frequency and damping values. 69
Table 6.2 Comparison of the free-free experimental results and model correlation. 70
Table 6.3 Calculated flapwise stiffness distribution. 70
Table 6.4 Calculated edgewise stiffness distribution. 71
Table 6.5 Average free-free frequencies of experiment and model compared. 71
Table 6.6 Blade strain calibration results. 72

EXECUTIVE SUMMARY

The Wind Energy Technologies department at Sandia National Laboratories has developed and field tested a wind turbine rotor with integrated trailing-edge flaps, seen in Figure ES.1, designed for active control of rotor aerodynamics. Analysis of the field test data has focused on addressing the following goals of the project:

- Demonstrate the control capability of the trailing-edge flaps.
- Evaluate the accuracy of simulation tools in predicting results of active rotor control.
- Develop procedures for characterizing an operating wind turbine which has active rotor control.

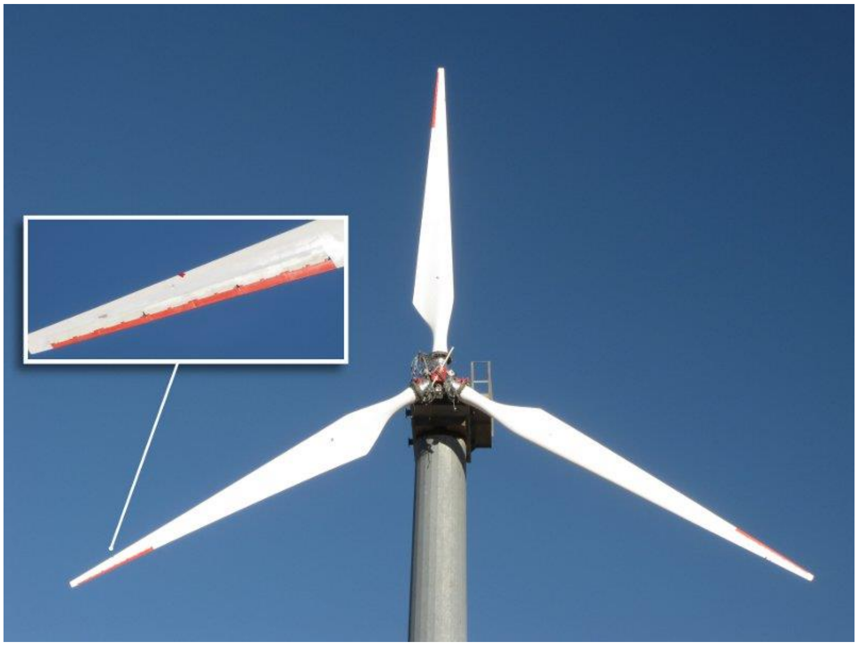

Figure ES.1 The SMART rotor consists of three 9-meter blades with trailing edge flaps spanning 20% of each blade length. The photo inset is a closer look at the flaps on one blade.

Control capability of the trailing-edge flaps was observed in the blade strain response. Figure ES.2 shows how the change in microstrain with wind speed shifts up or down by about 40 microstrain when the flaps are positioned at the +20 or -20 degree actuation limits. This change in strain at 6.75 m span is roughly equivalent to the amount of strain induced when the turbine goes from parked to operational. In 9 m/s wind, the blade strain at 6.75 m span during power production differs from the non-operational strain by 35 microstrain. Thus, the average observed control capability (measured at three-quarters blade span) with maximum flap deflection was roughly 114% of the strain that results from typical flapwise loading during power production.

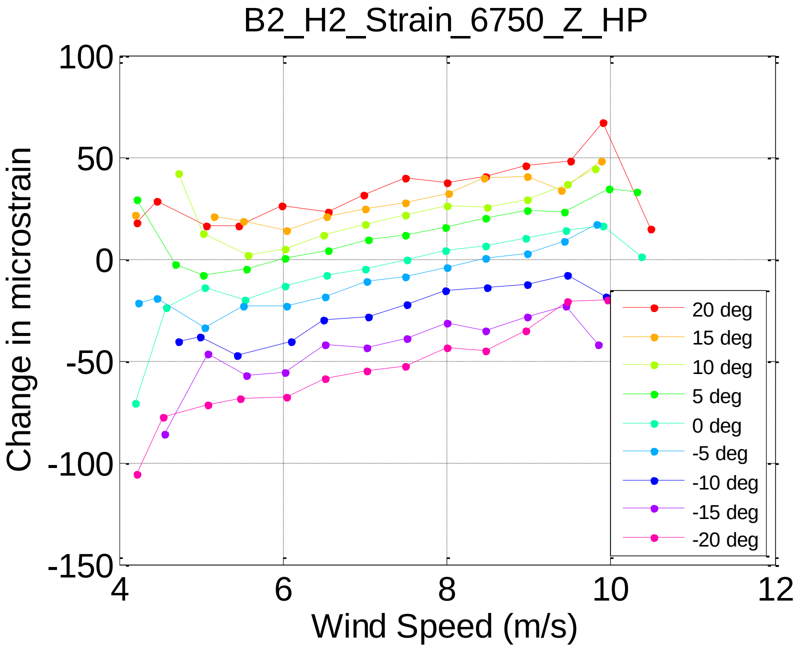

Figure ES.2 Average strain response as a function of wind speed shifts up and down with flap actuation angle.

The transient response of the wind turbine to step motions of the flaps was observed for the purpose of comparison to the response predicted by simulation tools. Analysis of blade strain step response revealed a combined aerodynamic and structure damping on the order of 1% to 3% of critical damping. Damping added by aerodynamic forces is typically difficult to quantify and this result shows step excitation is an effective method of system characterization.

Analysis of response time delays revealed the generator power step response reached peak value about 0.3 seconds after the flap step transition occurred. In this amount of time the rotor turned about one-third of a revolution and the wake moved downwind approximately one-eighth of a rotor diameter (assuming the wake was travelling at 8 m/s). This observation and the overall character of the step response are important results for evaluating the accuracy of simulation tools which support active aerodynamic control research.

Analysis of response time delays revealed the blade strain step response was delayed by 0.02 seconds, which is consistent with the expected amount of time required for the local blade section airflow to adjust to perturbations. This result also supports evaluation of simulation tools.

Aero-elastic system dynamics of the operational turbine system were observed in the frequency domain. Dynamics were heavily influenced by the effects of aerodynamic forces which add damping. Figure ES.3 shows the peak system response occurred at 4.4 Hz when the logarithmic sine sweep crossed this frequency at around 500 seconds. The vertical lines are multiples of the turbine’s rotational frequency (55 rpm or 0.92 Hz). The logarithmic sine sweep was shown to be a useful tool for system characterization.

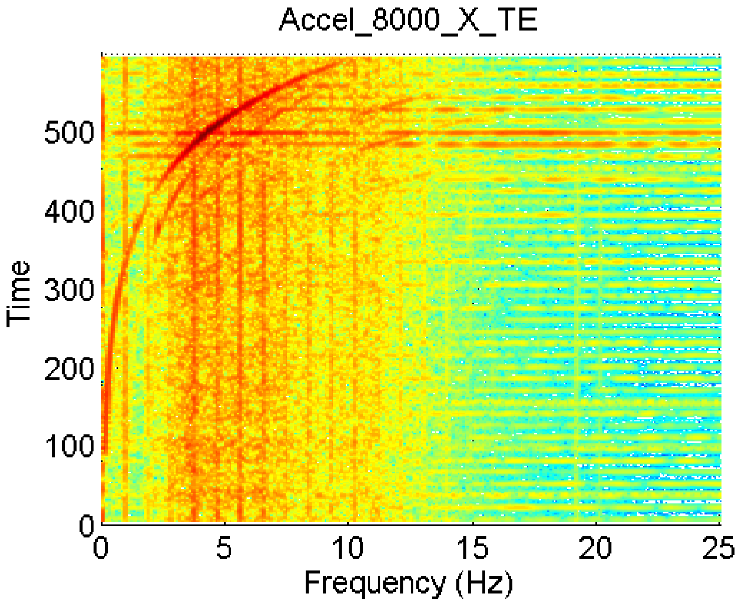

Figure ES.3 Excitation of flapwise acceleration frequencies over time with logarithmic sine sweep of flaps showing peak system response at 4.4 Hz.

Flap drive system dynamics were analyzed by using actuator current as an approximate measurement of the aerodynamic hinge moments acting on the flaps. A simple actuator model revealed the role of Coulomb (friction) and viscous damping in the flap drive system response. Frequency response of the flap actuation system was calculated and discussed in relation to the reduced frequency of unsteady aerodynamic response. These observations are important for the success of future closed-loop active rotor control.

Power curves for the SMART rotor were measured and compared to the power curve of a baseline CX-100 rotor. Effect of flap position on power was observed. These results are important to understand tradeoffs between energy capture and active aerodynamic load control.

NOMENCLATURE

AAD	active aerodynamic device
AALC	active aerodynamic load control
ATLAS	Accurate GPS Time-Linked Acquisition System
chordwise	in the direction of airfoil chord and perpendicular to blade span
dB	decibel
DOE	Department of Energy (U.S.)
edgewise	similar to chordwise but used to describe blade loads and deflections
flapwise	perpendicular to edgewise and in the direction of blade “flapping” motion
GBU	Ground-Based Unit (data acquisition subsystem)
GPS	global positioning system
HP	high-pressure (the nominally upwind surface of a HAWT blade)
IMU	inertial measurement unit
inboard	toward the root end of a wind turbine blade
LE	leading edge of wind turbine blade
LP	low-pressure (the nominally downwind surface of a HAWT blade)
outboard	toward the tip of a wind turbine blade
PID	proportional-integral-derivative
PSD	power spectral density
RBU	Rotor-Based Unit (data acquisition subsystem)
R&D	research and development
SFID	sequential frame ID
SMART	Structural and Mechanical Adaptive Rotor Technology
SNL	Sandia National Laboratories
spanwise	in the direction of the blade length
TE	trailing edge of wind turbine blade
TEF	trailing edge flaps

1. INTRODUCTION

1.1 Motivation

As the United States seeks to establish a diverse portfolio of clean and renewable energy systems, continued development of wind energy technology is essential to reaching renewable energy deployment goals. The Report on the First Quadrennial Technology Review (QTR), published by the U.S. Department of Energy in September 2011, was written to “establish a framework for thinking clearly about a necessary transformation of the Nation’s energy system” [1]. The QTR was a first step in developing guiding principles for DOE to prioritize investment of R&D funds. Within the “Clean Electricity Generation” strategy outlined in the report, wind energy is described as a fairly mature technology which is cost competitive at good wind sites and continues to expand market deployment. At a high-level assessment, the report states the technical headroom for additional research and development exists mainly in grid integration and subsystem reliability as well as tapping into the offshore wind resource.

The 20% Wind Energy by 2030 report [2], published in July 2008, provides a more detailed assessment of the technical headroom for additional R&D. The core opportunities it identifies include reducing capital costs, increasing capacity factors, and mitigating risk through enhanced system reliability. The rotor itself is highlighted as a key target for technology improvement because it is the source of all energy captured and of most of the structural loads entering the system. Increasing rotor size while controlling rotor loads will directly impact the capacity factor and the life of components within the main load path. The report mentions both passive load control in which the structural and material properties of the blades are tailored to passively mitigate loads and active load control in which a control system senses rotor loads and actively responds by driving aerodynamic actuators.

Reducing ultimate and oscillating (or fatigue) loads on the wind turbine rotor can lead to reductions in loads on other turbine components such as the main bearings, gearbox, and generator. This, in turn, is expected to reduce maintenance costs and may also allow a given turbine to use longer blades to capture more energy. In both cases, the ultimate impact is reduced cost of wind energy. With the ever increasing size of wind turbine blades and the corresponding increase in non-uniform loads along the span of those blades, the need for more sophisticated load control techniques has produced great interest in the use of aerodynamic control devices (with associated sensors and control systems) distributed along each blade to provide feedback load control (often referred to in popular terms as ‘smart structures’ or ‘smart rotor control’). A review of concepts and inventory of design options for such systems have been performed by Barlas and van Kuik at Delft University of Technology (TU Delft) [3]. Active load control utilizing trailing edge flaps or deformable trailing edge geometries is receiving significant attention because of the direct lift control capability of such devices. Researchers at TU Delft [4-5], Risø/Danish Technical University Laboratory for Sustainable Energy (Risø/DTU) [6-12] and Sandia National Laboratories (SNL) [13-19] have been active in this area over the past decade.

1.2 SMART Rotor Experiments

The Sandia SMART rotor project was conducted to demonstrate active control of wind turbine rotor aerodynamics and evaluate the simulation tools which support research in this area. The design and construction, which took place in 2010 and 2011, are documented in reference [20]. This report describes the results of the field test which was conducted in 2012.

The SMART rotor was tested on a modified Micon 65/13 which is a single-speed stall controlled (fixed-pitch) turbine. Each SMART blade was 9 meters long and was equipped with trailing edge flaps which spanned 20% of the blade length. The rigid flaps were hinged at 20% of chord and were actuated by electric motors. See reference [20] for additional information on the test site and test turbine.

Similar full scale turbine experiments were conducted by Risø DTU in collaboration with Vestas Wind Systems A/S on a V27 wind turbine [21, 22]. The Vestas V27 is a dual-speed pitch controlled turbine with 13 meter long blades and a nominal power output of 225 kW. One of the three blades had been equipped with trailing edge flaps (TEF) which spanned 15% of the blade length. The TEF were flexible in the first round of tests conducted in 2010 as described in reference [21]. As mentioned in reference [22], the TEF were changed to a stiff hinged flap design for the tests conducted in 2011.

Reference [21] describes three types of measurement configurations that were used:

- Trailing edge flaps fixed in neutral positions.
- Trailing edge flaps fixed in alternating low lift and high lift configurations.
- Trailing edge flaps actuated at a given frequency.

Testing showed the flap motions could alter the blade root flap-wise bending moment by 1 to 2% of the mean flap-wise moment. The flexibility of the flaps in the first round of tests increased modeling uncertainty because the TEF shape could deflect under aerodynamic load. Actuation at a given frequency increased the blade root moment power spectral density at the excitation frequency and also produced a coupled response in the other two blades at a slightly higher frequency.

Reference [22] describes closed-loop control of the TEF with a frequency-weighted model predictive controller. Technical issues prevented operation of the two inner flaps and so the one working flap spanned only 5% of the blade length. An average load reduction of 14% was reported for a test 38 minutes in duration.

1.3 Structure of This Report

The primary information, analysis, and conclusions are contained in Chapters 2 and 3 with additional explanation and supporting information in the subsequent chapters and appendix. Chapter 2 discusses aero-elastic modeling considerations and choice of models for simulation of active aerodynamic rotor control. Chapter 3 presents analysis of the field test data and resulting conclusions. Chapters 4 and 5 describe the data acquisition system and required data post processing. Chapters 6 and 7 describe ground test model calibration data and blade surface geometry scans.

2. AEROELASTIC MODELING

Simulation strategies and design tools have evolved to allow rapid prediction of performance and loads for modern horizontal-axis wind turbines. The aerodynamic components of these models, while not uniformly accurate for every turbine operating condition, have been in use for some time, and their behavior and regions of validity are fairly well-understood. The SMART rotor concept involves a fundamental change in rotor aerodynamic characteristics, since now aerodynamic properties may be dynamically changed at different locations along the blade span by active aerodynamic load control (AALC) devices. Also, the time scale of AALC device actuation is shorter than that of variable full-blade pitch. These differences may require modifications to existing wind turbine aerodynamic analysis tools, and may possibly require the development of new models of aerodynamic phenomena specific to AALC operation.

This chapter considers the aerodynamics of SMART rotor technology and implications for aerodynamic modeling. Existing aerodynamic modeling approaches are surveyed, and modifications or areas of need for new approaches are identified. This work does not provide a detailed review of all available modeling approaches for wind turbine aerodynamics. There are several good reviews from the past decade that cover this subject, including [23] and [24]. The emphasis here is on models capable of predicting:

- Aerodynamic loads that contribute to fatigue loading under turbulent wind conditions
- Blade aerodynamic response to AALC device actuation.

2.1 Aerodynamic Modeling Considerations for SMART Rotors

2.1.1 Time Scales

There are several relevant physical time scales, or groups of time scales, involved in wind turbine load control using AALC devices. Understanding these time scales gives insight into the underlying physical processes as well as the ability to assess the validity of various modeling approaches.

The first group of time scales is associated with excitation of the wind turbine aero-elastic system. The excitation inputs to the system include both the turbulent wind input and actuation of the AALC devices. The wind turbulence contains broadband velocity fluctuations, with energy distributed over a continuous range of time scales (and spatial scales). Some of this fluctuation energy occurs at time scales comparable to the wind turbine aero-elastic time scales. This leads to efficient excitation of the wind turbine structure, resulting in dynamic deflections of the blades and tower along with associated fatigue loads. Spatial variations in the mean wind speed due to wind shear, as well as low-frequency turbulent fluctuations that vary in space across the rotor plane, also lead to excitation of the wind turbine at multiples of the rotational frequency.

The device actuation time scale, on the other hand, is associated with the frequency of operation of the AALC device. The achievable range of the device actuation time scale is device-dependent. However, for effective load control the device time scale range needs to include the time scales of important excitation inputs, including the rotational frequency, its harmonics and possibly higher frequency wind events.

The second set of time scales is associated with the structural modes of the wind turbine system; these modes include blade modes (flapwise, torsional, edgewise), tower modes, coupled modes, and full system modes. Each mode has a natural frequency with an associated time scale. Typically, the lowest-frequency structural modes are the most important in determining dynamic response and loads. In application of AALC devices, reduction of flapwise fatigue loads is usually a primary goal, although care must be taken to avoid excessive excitation of torsional and edgewise modes by the AALC system.

The third set of time scales is associated with aerodynamic phenomena on actively controlled blades. A local blade section flow time scale is associated with the time for a particle to travel the local chord length at the local relative flow velocity, or $t_f = c/U_{rel}$. A related aerodynamic time scale is the time for the local two-dimensional flow over a blade section to adjust to a sudden perturbation, such as an instantaneous change in angle of attack or AALC device deployment. This time scale is usually at least several times the local section flow time scale. A third aerodynamic time scale is the wake response time, or the time for the velocity field induced by the rotor trailing vorticity to adjust to a sudden change in blade aerodynamic load distribution. When considering the wake response of a load change on the entire rotor, this time scale is usually much longer than the local section flow time scale, since it is proportional to the ratio of rotor radius to the wind velocity.

Table 2.1 shows estimates of various time scales for the Sandia 115kW test turbine operating at 55 RPM with a wind speed of 8 m/s. The center of the AALC flapped section is located at 89% of the rotor radius, which is where the local section flow time scale is estimated. The range of AALC device actuation time scales is assumed to include the period of the first two blade flapwise modes, as well as the periods associated with the rotational frequency and two harmonics of the rotational frequency (1P,2P,3P). It is assumed the AALC devices are actuating in response to wind fluctuations that cause structural excitation at these frequencies.

Table 2.1 Time scales associated with active aerodynamic control for the Sandia 115kW test turbine.

Process	Time Scale Definition	Time Scale
AALC Device Actuation	Actuation Period	0.09 – 1.1 sec
Response to Rotationally Sampled Wind	1P,2P,3P periods	0.3 - 1.1 sec
Dynamic Structural Response	Period of First Two Blade Flap Modes	0.09 - 0.22 sec
Local Section Flow	Chord / Relative Flow Velocity	0.004 sec
Local Section Flow Adjustment	5-10x Section Flow Time Scale	0.02 - 0.04 sec
Wake Response	Rotor Radius / Wind Speed	1.2 sec

2.1.2 Unsteady Aerodynamics

The interactions between wind turbulence, aerodynamic loads, and structural dynamics give rise to the fatigue loads that AALC devices seek to control. The turbulent wind and AALC device actuation serve as inputs to the overall aero-elastic system. Aerodynamic forces and moments (aerodynamic loads) are generated in response to these inputs. The aerodynamic loads, in turn, excite the structural dynamic modes, which lead to structural fatigue loading. Structural modes may also couple with one another, changing the structural loading. Further, structural motion modifies the aerodynamic loads, resulting in a two-way coupled system.

To simplify the arguments, consider only a one-way coupling in which inputs lead to aerodynamic loads, which in turn lead to dynamic structural loads. A key question is whether assumptions of large separation of the aerodynamic and structural dynamic time scales are valid. If these time scales are sufficiently far apart, then the aerodynamics can be assumed to occur nearly instantaneously (termed a quasi-steady assumption), simplifying the required aerodynamic models.

Recall that there are several aerodynamic time scales, two of which are most relevant to the present discussion: the local flow adjustment time scale, and the wake response time scale. Consider first the local flow adjustment time scale. At first glance, for the Sandia 115kW test turbine, the flow appears to adjust fairly quickly compared to the actuation and structural time scales (0.04 second versus 0.09-1.1 seconds). However, this qualitative observation is not sufficient to ensure that a quasi-steady assumption of the aerodynamic loads is valid. What also must be determined is whether the aerodynamic response to an unsteady excitation is quasi-steady. In other words, are the amplitude and phase of the aerodynamic loads in response to wind turbulence or AALC device actuation well-approximated by the steady-state response at each point in time during the transient?

This question can be answered by examining the reduced frequency of the excitation. The reduced frequency k is defined by

$$k \equiv \frac{\omega c}{2U_{rel}} \tag{2.1}$$

where ω is the circular frequency of the excitation, c is the local blade chord length, and U_{rel} is the local flow velocity relative to the blade section. The reduced frequency is essentially a scaled ratio of the flow time scale to the excitation time scale. The aerodynamic response to unsteady excitation is a function of the reduced frequency. For small reduced frequencies, the response is essentially quasi-steady, while for large reduced frequencies the response is highly unsteady and deviates substantially from the quasi-steady response, both in phase and amplitude. Leishmann [23] states that an unsteady aerodynamic system can only be considered quasi-steady for $k < O(0.01)$. For $k < 0.05$, errors due to the quasi-steady assumption are likely acceptable for wind turbine aero-elastic system modeling. Note that this implies the flow time scale must be almost two orders of magnitude less than the excitation time scale for the quasi-steady assumption to hold. For higher reduced frequencies, the unsteady aerodynamic loading will differ from that of the quasi-steady case, with possibly important implications for determining structural loads and aero-elastic stability.

The reduced frequency range of the AALC excitation for the Sandia test turbine at 89% radius is calculated as $0.01 < k < 0.2$. The low end of the estimated reduced frequency range is associated with the 1P disturbance, which can be caused by wind shear or tower shadow. Note that 1P loads can be effectively reduced using individual blade pitch control [25]. If the primary action of the AALC devices is to control 1P loads, then a quasi-steady aerodynamic model is probably sufficient. If the AALC devices are actuating on time scales associated with blade mode natural frequencies, or 3P or higher rotational harmonics, the estimate indicates that the quasi-steady assumption is not strictly valid ($0.06 < k < 0.2$). In this case, an unsteady aerodynamic model for the response to turbulent wind and AALC device actuation should be used.

The rotor wake response is seen to occur over a time scale of about 1.2 seconds. Note that this corresponds to roughly one rotor revolution; it may actually take five or more rotor revolutions for the wake, once perturbed, to settle into a steady state. The relevant reduced frequency for this case uses the rotor radius and wind speed to non-dimensionalize the frequency, rather than the blade chord and local relative velocity. A caveat is that wake and inflow time scales vary along the blade, and are shorter for the outboard part of the blade than for the inboard part. This can be accounted for in an approximate way by using the wake time scale distribution function from the wake model of Snel [26]. Another consideration is that only the outboard part of the blade, the part containing the AALC devices, is undergoing unsteady aerodynamic changes. Thus, a more relevant length scale for computing reduced frequency is the AALC device span. Assuming a device span of 20% of the blade centered about $r/R = 0.89$ for the SMART rotor, the reduced frequency of the wake response using the expected AALC actuation frequency is in the range $0.25 < k < 2.5$. The reduced frequencies are again such that the quasi-steady assumption is poor. This means a dynamic wake model is necessary to resolve changes in blade aerodynamic loading due to turbulent wind and/or AALC device actuation.

In summary, estimates for reduced frequency associated with wind turbine structural excitation and AALC actuation indicate:

- A quasi-steady aerodynamic model may be sufficient for excitation at the rotational frequency.
- For excitation at higher harmonics of the rotational frequency, or direct excitation of blade modes by high frequency turbulent energy, an unsteady aerodynamic model is required.
- For modeling of the effect of aerodynamic wake response to wind turbulence or AALC device actuation, a dynamic wake model is required.

2.2 Aerodynamic Model Choices for SMART Rotors

The aerodynamic modeling of a wind turbine rotor is usually divided into two components: blade sectional modeling and wake modeling. The blade sectional models predict local aerodynamic forces and moments for two-dimensional sections of the blades given local flow properties such as angle of attack and relative velocity. The wake models (also called “inflow models”) predict the velocity induced by the trailing vorticity in the rotor wake. The two models are coupled since the wake model affects the inputs to the sectional aerodynamic model, while the section model provides aerodynamic load distributions that determine the strength and shape of the wake.

The previous section outlined the need for dynamic models for both the blade section and the wake aerodynamics. This section discusses some of the available models and their appropriateness for SMART rotor applications.

2.2.1 Blade Sectional Models

In the usual blade element approach, the blade is divided into airfoil sections, or elements, and the static two-dimensional aerodynamic characteristics of each element are described using lift, drag, and pitching moment tables defined across the relevant range of angle of attack and chord Reynolds number. For airfoil sections with AALC devices, tables also need to be derived for the static performance of the airfoils with devices deployed. Unsteady aerodynamic effects can be accounted for by using thin-airfoil theory and the relevant potential flow solutions [23]. For airfoil sections with trailing edge AALC devices, the theory can be modified to account for unsteady actuation of the devices. This has been done for devices that change trailing edge camber (flaps or morphing trailing edge) [27] as well as for miniature Gurney flap (or “micro-tab”) devices [28].

For large device actuation amplitude and frequency, or for large or rapid changes in the incident angle of attack, a nonlinear model describing the dynamic stall process must be included. There is some question regarding the importance of modeling dynamic stall properly for SMART rotors. Under turbine operating conditions with small yaw error and “usual” stochastic atmospheric turbulence levels, the outboard region of a variable-pitch rotor should not be stalled, either statically or dynamically. This assumption has been justified by full system aero-elastic simulations [25]. In these conditions, modeling of dynamic stall is not important in determining the ability of AALC devices to reduce fatigue loads. However, when analyzing the performance of AALC devices and a SMART rotor control system under non-ideal operating conditions, such as at large yaw angle, properly modeling dynamic stall is important. Dynamic stall models for some AALC devices, including a morphing trailing edge and microtabs, have been developed [28, 29].

Various three-dimensional flow effects must be accounted for by modification of the two dimensional airfoil models for analysis of wind turbine blades. Rotational augmentation [30] increases lift and delays stall to higher angle of attack, due to the effects of blade rotation on the boundary layer. This effect is most important on the inboard portion of the blade, and is of secondary importance to modeling the aerodynamics of AALC devices, which will most likely be placed on the outboard part of the blade. The three-dimensional flow induced by the blade tip vortex does affect the outboard part of the blade. Models for this effect are available in the form of “tip-loss” models (see, e.g., [31]), although these do not account for the presence of outboard control surfaces. The AALC devices themselves can generate trailing vortices which may interact with the tip vortex and thus change the local aerodynamic behavior. More analysis and/or experimentation is needed to determine the importance of this effect and appropriate modeling strategies.

In summary, the primary components of blade sectional aerodynamic models for SMART rotor fatigue analysis include:

1. Static airfoil performance tables with and without AALC device deployment
2. Unsteady airfoil aerodynamic model (from thin airfoil theory, for example)
3. Unsteady AALC device aerodynamic model (modification to thin airfoil theory)
4. Dynamic stall model for airfoil with AALC devices, for analysis of non-ideal operating conditions
5. Tip-loss model, possibly modified for interaction with AALC devices

2.2.2 Rotor Wake Models

Wake models for SMART rotors must include dynamic wake effects, as discussed in Section 2.1.2. This precludes the use of an equilibrium wake model such as the classical Blade Element Momentum (BEM) model. Variants of the BEM model have been developed that include dynamic wake effects. One such model is presented in [26], where the wake is approximated by a cylindrical vortex sheet extending from the rotor plane to an infinite distance downstream of the turbine. A dynamic equation for induction velocity at the rotor plane is derived using vorticity/velocity relationships and balancing changes in blade forces with changes in trailed vorticity. This results in a relatively simple differential equation model for unsteady induced velocity at the rotor axis; it can also be modified to give an induced velocity distribution across the rotor disc. There are some theoretical limitations to models based on the BEM foundation. For the model in [26], the blade load distribution is assumed to be linear with radius, which leads to a constant load per swept area. Further, implementations of this type of model assume the momentum balance takes place in an averaged sense over an annular region of the rotor. It is not clear that this approach is valid for analysis of a wind turbine operating in turbulent wind, where significant instantaneous variations in wind speed may occur across the rotor.

Dynamic Inflow Models

An alternative approach to wake modeling follows the method of “Dynamic Inflow” (DI) initiated by Pitt and Peters [32]. The DI modeling framework has led to a family of models, including the Finite State Induced Flow model [33]. A particular implementation of this type of model is the Generalized Dynamic Wake (GDW) model, described in [34], and implemented in the Aerodyn code [35].

Both the DI and GDW models are based on the actuator disc concept. An actuator disc is an infinitesimally thin region, coincident with the rotor plane, over which aerodynamic forces are assumed to act on the surrounding flow. The actuator disc concept itself is fairly general, in that it only provides a means for modeling the action of aerodynamic blade loads. The flow dynamics are then modeled using any number of methods, ranging from simple potential flow models to numerical solutions of the Navier-Stokes equations. The DI and GDW models are based on the linearized momentum equation (and continuity equation) governing inviscid, incompressible flow.

The momentum equation is linearized about a uniform free-stream, and solutions are found for the induced flow distribution normal to the rotor plane. Because of the linearization, the induced flow is assumed to be a small perturbation to the free-stream flow. For a wind turbine, this means the model is strictly valid only for small values of the axial induction factor, $a << 1$.

The pressure field for linearized, inviscid, incompressible flow satisfies LaPlace's equation. The pressure field in the DI and GDW models is based on the work of Kinner (see [36]), who found solutions to LaPlace's equation that contain a discontinuity in pressure across a circular disc. A general solution for pressure can be expanded in an infinite sum involving products of Legendre polynomials and azimuthal Fourier components. The aerodynamic blade loads are similarly expanded in a spectral basis, and are used to force the surrounding pressure field solution.

The GDW model has the advantage that it is derived from the momentum equation, so in this sense it is a first-principles approach, within the constraints of the applied linearization. While the model is not explicitly based on vortex dynamics, the Kinner solution field in the wake will include vorticity [36]. However, due to the linearization, the model is essentially a prescribed wake method and will not describe non-linear behavior such as vortex roll-up.

The assumption of small induction factor involved in the linearization of the momentum equation is the primary limitation of the model. The model would be expected to be accurate for lightly-loaded rotor conditions. Unfortunately, wind turbine induction factors are usually relatively large, with the optimum induction factor for an ideal rotor being $a = 1/3$.

The GDW model is quite general in allowing for arbitrary blade loadings and induced velocity distributions. Practically, the allowable loadings and velocity distributions are limited by the number of terms retained in the pressure field, velocity field, and blade load expansions. Thus, sharp flow features that may occur due to step changes in spanwise loading, such as occurs at the blade tips or at the edge of aerodynamic control surfaces, will not be captured precisely unless a very large number of terms is included. The implementation of the GDW model in Aerodyn includes four azimuthal harmonics and four Legendre polynomials in the radial direction. The number of polynomials would likely need to be increased in order to model SMART rotors, increasing the cost and complexity of the model.

Free Vortex Wake Models

The flow in the wake of a lifting surface such as a wind turbine blade is often best described in terms of vortices and their dynamics. This motivated the relatively simple wake model discussed earlier [26], in which the wake is modeled as a semi-infinite vortex sheet. A vortex sheet is an example of a singular potential flow solution used to describe part of a wake flow; other potential flow elements include vortex filaments and vortex particles. When the position of the potential flow elements is kept fixed at pre-determined positions in space, the model is called a prescribed wake model. Prescribed wake models require advance knowledge of the wake shape, which in the general case must be determined experimentally. For relatively simple configurations, such as a turbine in steady, uniform, axial flow, prescribed wake models can be very accurate. However, for more complex flow conditions, uncertainty in the geometry of the wake leads to inaccuracies.

A prescribed wake model may not make a good choice for modeling a turbine with active aerodynamic load control. First, the model would need to provide an accurate description of the wake under turbulent wind conditions in order to furnish fatigue load predictions. Under turbulent wind conditions, the wind velocity varies across the rotor disc and as a function of time, which may cause local distortions of the wake geometry that are not accounted for in the prescribed wake method. Second, the AALC devices may induce local changes in aerodynamic blade loading that cause perturbations to the wake geometry. For small enough perturbations this effect may be negligible, but this should be verified by comparisons to a more accurate wake model.

An alternative is to use methods where the wake geometry is free to evolve in space and time. These methods usually use vortex elements as the computational building blocks, and are called free vortex methods (FVM). Free vortex methods have been popular in the rotorcraft community for some time [37], and have also been applied to horizontal axis wind turbines [38 – 42]. In one variant, the vortex filament method, vorticity in the wake of a turbine blade is tracked using curved filaments representing concentrations of vorticity. This includes the important tip vortex, trailed from the blade tips, as well as weaker trailing vortices resulting from non-uniform circulation (along the span). Changes in local section circulation produce shed vortices, oriented parallel to the blade trailing edge. Non-uniform circulation and unsteady sectional lift both occur under turbulent wind conditions. Non-uniform spanwise circulation can occur when AALC devices are actuated, creating step change in blade loadings. All of these effects, in principle, are addressed by the FVM.

Other FVM's besides the vortex filament method include the vortex particle method [38], vortex sheet method [43], and hybrids that include some combination of vortex elements [38, 43]. Usually, the FVM is combined with a lifting line method for describing the distribution of loading along the blade. The lifting line is a bound vortex fixed to the blade that models the lift distribution, and from which the trailing and shed vortex elements emanate. It can be tied to sectional airfoil models such as those described in Section 3.1 that account for unsteady sectional aerodynamics, dynamic stall, and unsteady AALC device actuation. The FVM can also be combined with a Navier-Stokes CFD solution in the near field of the rotor blades, as described in [44]. Although this method may result in computational savings over a CFD model of the entire rotor flow-field, it is not yet practical for design or fatigue load calculations.

One detail of potential flow wake models that may be important for SMART rotors is the issue of non-planar wake behavior. The wake of a blade or wing just downstream of the trailing edge is usually well-described by a thin, planar sheet attached to the trailing edge. An AALC device may perturb the wake such that the wake is no longer planar. An example is the wake of a trailing edge flap with non-flapped blade sections on either side of the flap. The flap displaces the wake above or below the unflapped wake position, resulting in a discontinous wake geometry. A planar wake assumption in this case can lead to inaccuracies in blade load predictions. This limitation can be overcome by incorporating a non-planar wake method [45].

One aspect of the FVM that has hindered widespread use in wind turbine design is its computational cost. For a simulation with N vortex elements, the computational cost is proportional to N^2, since the induced velocity from each element must be calculated at every other element position. There are algorithms for computing the velocity field that scale linearly with N, such as the fast multipole method [46]. This method was applied to vortex particle simulations in [43], but can also be applied to vortex filament methods [47]. Some run times were reported in [43] for various FVM methods. It is not clear if FVM methods are yet practical for running wind turbine fatigue load cases (multiple 10-minute turbulent wind simulations, for example). A study of the required computational resources to accomplish this would be very useful.

Summary of Wake Models

In summary, the following are important considerations for choice of a rotor wake model for simulating SMART rotors:

- Models based on BEM theory usually employ averaging over annular regions of the rotor disc, and may not properly resolve important instantaneous spatial variations in blade loading.
- Dynamic inflow models, within the constraints of the assumption of small induction factor, can simulate arbitrary inflow distributions associated with turbulent wind excitation and/or AALC device actuation. However, the method converges relatively slowly with increases in degrees-of-freedom (DOFs) and may become inefficient when enough DOFs are retained to resolve the wake of AALC devices.
- Free vortex wake models offer a general framework for describing SMART rotor wake dynamics, and their use in this application would be limited primarily by considerations of computational cost.

2.3 Conclusions

The analysis of Section 2.1.2 indicates that unsteady aerodynamic models are needed for SMART rotor analysis. This is not surprising given that much of the rationale for using unsteady aerodynamic models for SMART rotors is relevant for analysis of turbulence-induced fatigue loads, a standard design case. Other considerations particular to SMART rotor modeling have been identified, however. These include airfoil sectional models that incorporate unsteady aerodynamic modeling of the device actuation, as well as dynamic wake models that are able to account properly for the shed and trailed vorticity generated by the devices. The sectional models are currently available for some devices, but may need to be tailored to the particular device geometry of interest. The required wake models are also available, but selection of a particular model involves tradeoffs between accuracy and computational expense. The free vortex wake methods involve fewer assumptions than other techniques and therefore offer the potential for greater accuracy, but care must be taken that they can be efficiently employed in fatigue analyses which may involve long simulation times.

3. FIELD TEST DATA ANALYSIS

Analysis of the field test data has focused on addressing the following goals of the project:

- Demonstrate the control capability of the trailing-edge flaps.
- Evaluate the accuracy of simulation tools in predicting results of active rotor control.
- Develop procedures for characterizing an operating wind turbine which has active rotor control.

This chapter references the concepts of aerodynamic time scale and reduced frequency which were presented in Chapter 2.

3.1 Flap Control Capability

The primary type of flap motion that was used to characterize the control capability of the flaps was a sequence of step motions between the 0 degree position and ± 5, 10, 15, and 20 degrees. The duration of each step assumed one of two configurations. First, the duration was 2.18 seconds which is nominally two rotor revolutions. In this configuration, all the flap positions were cycled through quickly which allowed a rapid characterization of the overall control capability. Second, the duration of each step was extended to 30 seconds so that transient aerodynamic response would reach steady state before another step motion was initiated.

Figure 3.1 shows the strain response of the most outboard foil strain gage located at 6.75 m span. Overlaid on the strain response is the commanded flap position (to facilitate comparison, the strain data has been scaled to be of similar magnitude). The correlation between change in strain and change in flap angle is clearly visible, although turbulent wind conditions had a pronounced effect on strain as well. The curves in Figure 3.2 were produced by binning the data according to wind speed and then averaging the strain response for each flap position. The zero degree flap curve shifts up or down by about 40 microstrain when the flaps are positioned at the +20 or -20 degree actuation limits. This change in strain at 6.75 m span is roughly equivalent to the amount of strain induced when the turbine goes from parked to operational. In 9 m/s wind, the blade strain at this span during power production differs from the non-operational strain by 35 microstrain. Thus, the average observed control capability (measured at three-quarters blade span) with maximum flap deflection was roughly 114% of the strain that results from typical flapwise loading during power production.

The overall character of these curves matched the expectations from simulation. Simulation predicted that the control capability on the positive flap angle side would be somewhat less than the control capability on the negative flap angle side due to the upper limit on lift coefficient and the initiation of stall with high positive flap angles. This effect can be seen in Figure 3.2 where the change in strain for the -20 and +20 degree settings relative to the 0 degree setting are respectively 50 and 33 microstrain.

Similar results were obtained for the other three strain gage locations but with decreasing ranges of change in strain. For the -20 and +20 degree settings, one-half blade span saw changes of 44.7

and 31.6 microstrain, one-quarter blade span saw changes of 25 and 14.6 microstrain, and the root saw changes of 4.3 and 2.9 microstrain. The decreasing range was largely the result of blade stiffness increasing toward the root. At the root, average strain during power production differs from the non-operational strain by about 8 microstrain. Because the strain at a particular span location results from all load outboard of that location, the active control portion of the blade contributes most of the load experienced at three-quarters span but contributes proportionally less at the root.

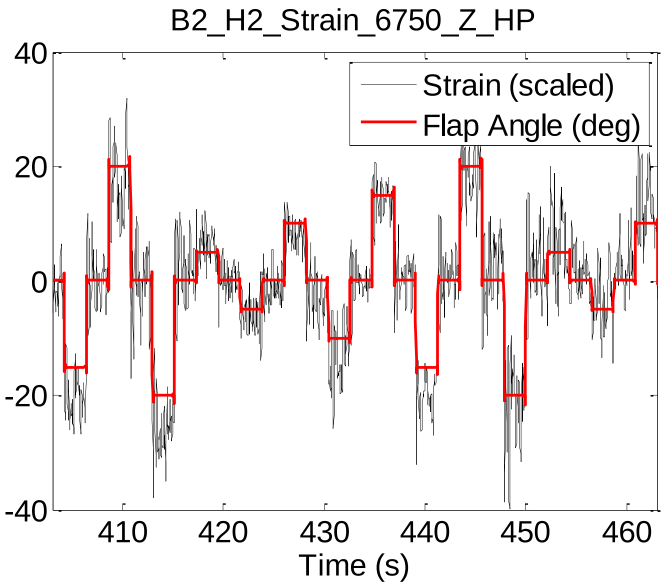

Figure 3.1 Strain response tracking with flap step sequence.

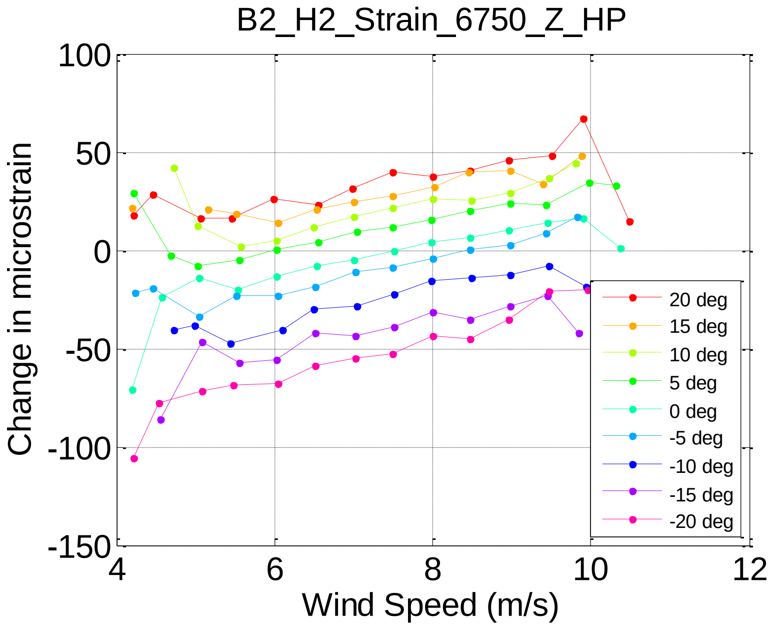

Figure 3.2 Average strain response as a function of wind speed shifts up and down with flap actuation angle.

3.2 Time-Average Response to Step Actuation

A sequence of step motions between the 0 degree flap position and ± 5, 10, 15, and 20 degrees was also employed to characterize the overall system response. The duration of each step was extended to 30 seconds so that transient aerodynamic response would reach steady state before another step motion was initiated. The strain response to each step with the 30 second duration is similar to the results observed in Figure 3.1 for the shorter duration steps.

The ensemble average of many such responses to the same flap motion revealed the mean flap response hidden beneath the stochastic wind excitation responses. This time-averaging was accomplished by first aligning the signals with a “trigger window” centered on the flap angle signal at a specified trigger level. Then the signals were resampled with a consistent time vector and averaged.

The following results are focused on the 20 degree flap step response and used a trigger level of 19 degrees. The time axis is aligned so that the flap angle passes through the trigger level at 0.0 seconds. Rise time for the flap step motion was around 0.1 seconds with an average actuation rate of about 200 degrees per second and a maximum rate of 330 degrees per second.

Figure 3.3 shows the strain signals of 29 individual responses to the 20 degree step motion. Although the random wind excitation produced a wide band of data which is plotted in gray, consistent structure in the data is evident in the first second after the step transition. The structure was clearly revealed in the average of these 29 responses which is plotted as the thin black line. Figure 3.4 focuses on the first 1.5 seconds of this mean response. The time delay between the flap motion and strain response was about 0.02 seconds, which appears to be consistent with the aerodynamic time scale associated with local section flow adjustment. Although the response was not strictly a “damped free vibration” due to the presence of both constant and random wind excitation, application of the theory for damped free vibration provided some insight into the response. First, the frequency of vibration was calculated from the time between peaks to be 4.17 Hz which matches the first flapwise blade bending mode. Second, the damping ratio ζ for damped free vibration can be calculated from the logarithmic decrement [48], here denoted by δ in equation (3.1). The logarithmic decrement is simply the natural logarithm of the ratio u_i / u_{i+1} of two successive peak values. If ζ is small such that the denominator in the right hand expression of equation (3.1) is approximately 1, then the damping ratio can be easily calculated from equation (3.2). Using these equations, a damping ratio on the order of 1% to 3% of critical was calculated from the peaks seen in Figure 3.4 using the information contained in Table 3.1. Damping added by aerodynamic forces is typically difficult to quantify and this result shows step excitation is an effective method of system characterization.

$$\delta = ln\frac{u_i}{u_{i+1}} = \frac{2\pi\zeta}{\sqrt{1-\zeta^2}} \tag{3.1}$$

$$\zeta \approx \frac{\delta}{2\pi} \tag{3.2}$$

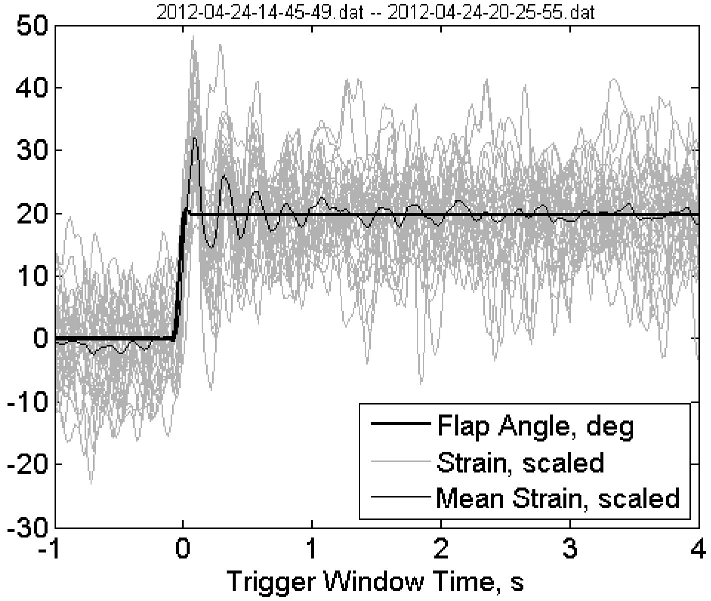

Figure 3.3 Ensemble average strain response to 20 degree flap step.

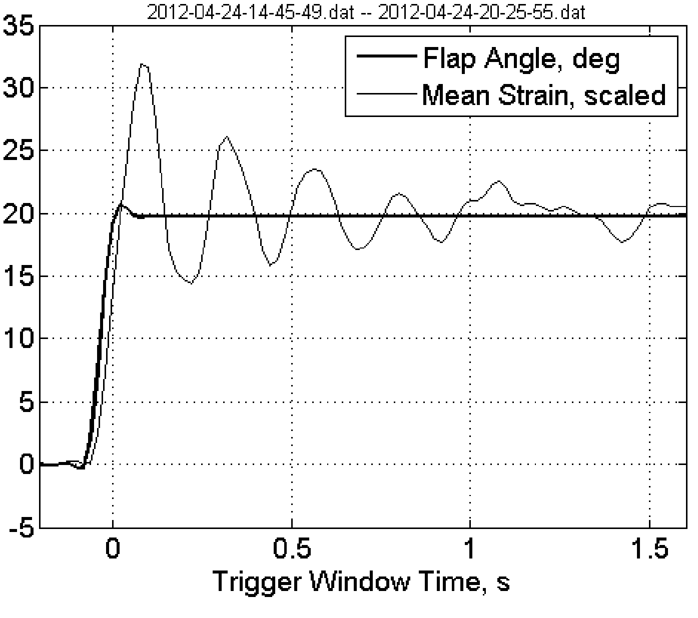

Figure 3.4 Detail of strain oscillations in step response.

Table 3.1 Damped free vibration parameters calculated from strain response.

Peak	Maximum	Time, s		Peaks	Log Decrement	Damping Ratio	Time Difference, s	1/ ΔT, s^{-1}
u_1	30.38	0.0799		$u_2 - u_1$	0.202	0.032	0.2396	4.17
u_2	24.83	0.3195		$u_3 - u_2$	0.097	0.015	0.2397	4.17
u_3	22.54	0.5592		$u_4 - u_3$	0.080	0.013	0.2396	4.17
u_4	20.81	0.7988						

Using the same time-averaging procedure, the ensemble average response of generator power seen in Figure 3.5 reveals a subtle jump in power output which begins to rise at approximately 0.15 seconds on the trigger window time axis and reaches peak value at 0.3 seconds. In 0.3 seconds the rotor turned about one-third of a revolution and the wake moved downwind approximately one-eighth of a rotor diameter (assuming the wake was travelling at 8 m/s). This time delay observation and the overall character of the step response are important results for evaluating the accuracy of simulation tools which support active aerodynamic control research.

Looking at the individual power output signals plotted in gray in Figure 3.5, the jump is visible in many of them; however, the amount of variation between signals suggests that attempting to draw any additional conclusions from the mean response may be asking too much. It is likely that more than 29 response signals need to be averaged and the variation in wind speed needs to be taken into account in order to accurately identify other repeatable dynamics being exhibited here.

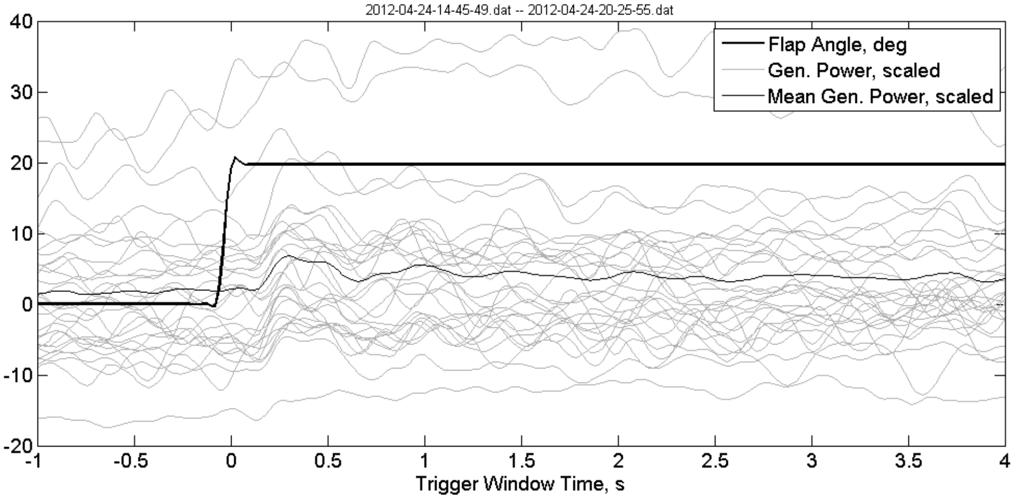

Figure 3.5 Ensemble average generator power response to 20 degree flap step reveals delayed jump in power output.

Signals from the inertial measurement unit (IMU) mounted on the rotor were also examined using the time-averaging approach. Plotted in Figure 3.6, the z-component, which senses fore-aft tower motion, shows that a substantial ringing was induced at tower top approximately 0.05 seconds after the flap step motion.

It is interesting to note that the rotor thrust response occurs before the generator power (and by implication the rotor torque) shows any sign of change. Temporal alignment of signals was double checked to verify the effect was real and not a post-processing error. Timing of the IMU signals were verified against the rotor azimuth. Timing of the channel which measured the generator power signal was verified through post-testing of the data acquisition system; however, phase shift possibly caused by the power transducer itself is unknown but believed to be zero. Barring a timing issue, the result indicates that rotor thrust is the cumulative effect of local section flow adjustment and therefore occurs along the same time scale. Rotor power and torque, however, appear to be directly tied to changes in the rotor wake which occur at the longer wake-response time scale. The change in induction factor resulting from the delayed wake response may explain the small reversal of oscillation observed in Figure 3.6 from 0.2 to 0.5 seconds, but the reversal might also be simply a secondary frequency of tower top motion.

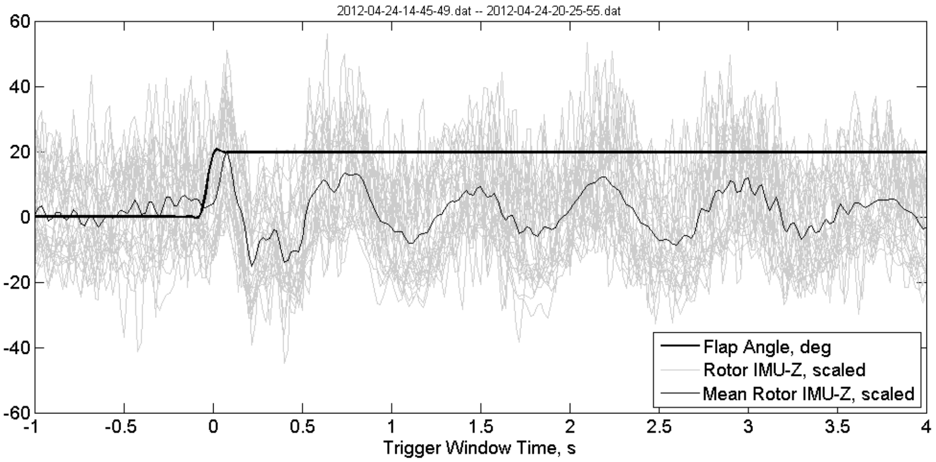

Figure 3.6 Ensemble average response of fore-aft (axial) component of rotor IMU to 20 degree flap step.

Ensemble averages were computed for strain, power, and rotor IMU acceleration at the other flap step magnitudes and are shown in Figures 3.7 through 3.9. Results followed the same trends as seen previously with similar time delays. The -20 degree flap steps just happened to sample wind with less speed fluctuation and the individual responses are seen to be tightly grouped with a rather clean ensemble average, particularly in the case of generator power.

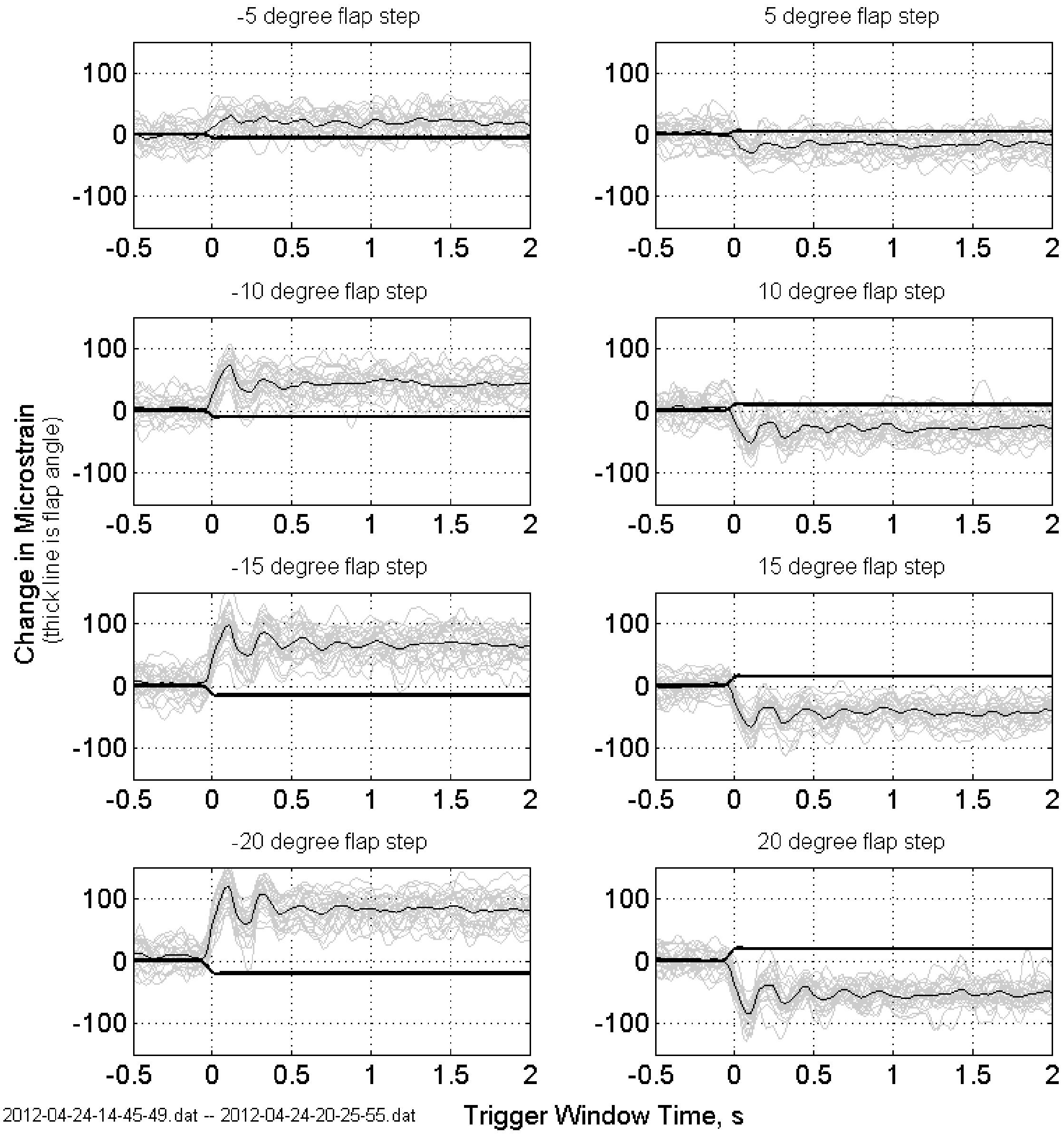

Figure 3.7 Ensemble average strain response at 6.75 m span.

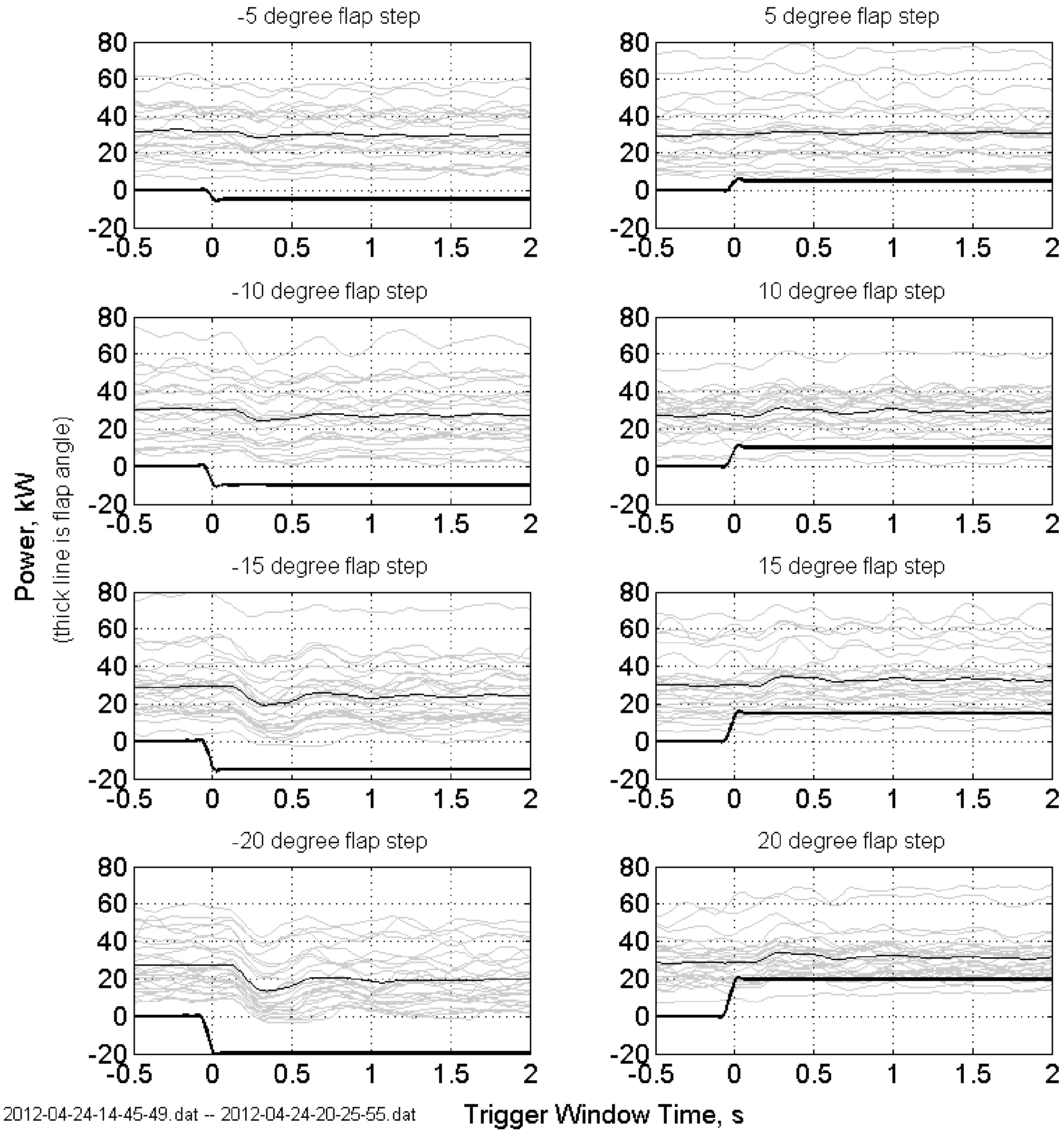

Figure 3.8 Ensemble average generator power response.

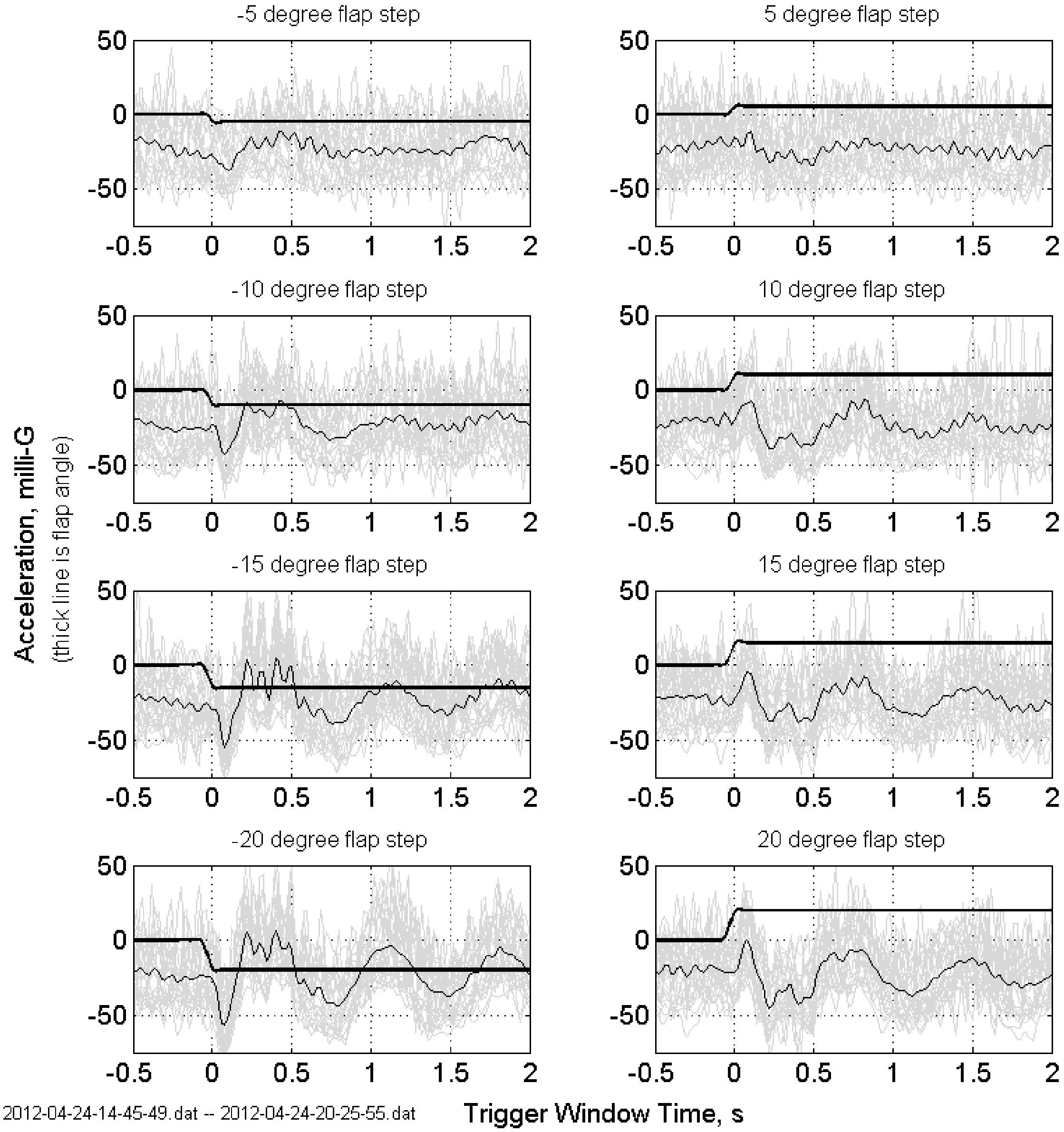

Figure 3.9 Ensemble average rotor IMU response, fore-aft (axial) component.

3.3 Rotor Dynamics

3.3.1 Sine Sweep with Rotor Stopped

Sinusoidal flap motion with logarithmic sweep of frequency was used to provide a driving force over a range of frequencies. With the rotor parked, the inertia of the flap motion generated the controlled frequency input while the ambient inflow created a small random buffeting input on the flat of the blade. Figure 3.10 is the spectrogram of flapwise acceleration during a test which swept over the frequency range 0.1 to 10 Hz in 500 seconds. The main red portion is the logarithmic frequency input and the vertical lines are structural resonance frequencies. The other curves following the shape of the red curve are harmonics of the main input frequency. Broadband frequency input up to about 15 Hz is visible in the background due to the random wind buffeting. The power spectral density (PSD) of this same test for all three blades, given in Figure 3.11, shows a more refined view of the individual frequency response peaks.

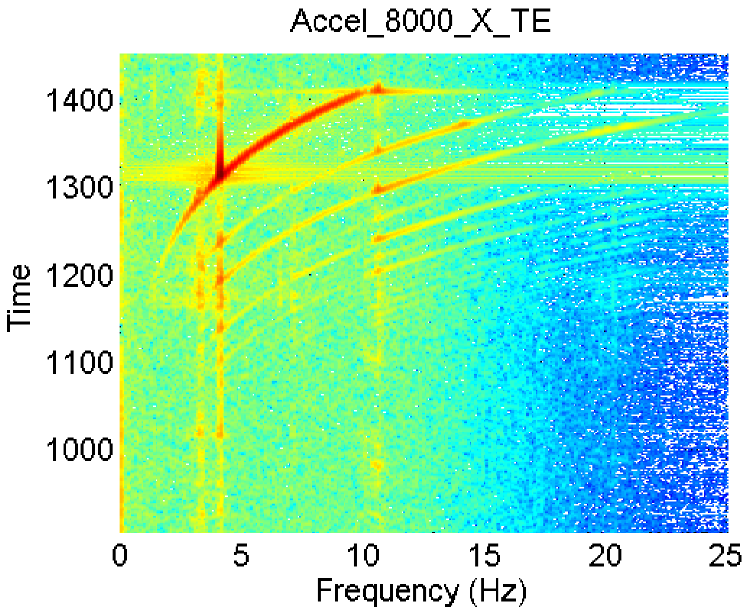

Figure 3.10 Parked rotor spectrogram (waterfall plot) of flapwise acceleration at 8000 mm span with logarithmic sine sweep excitation.

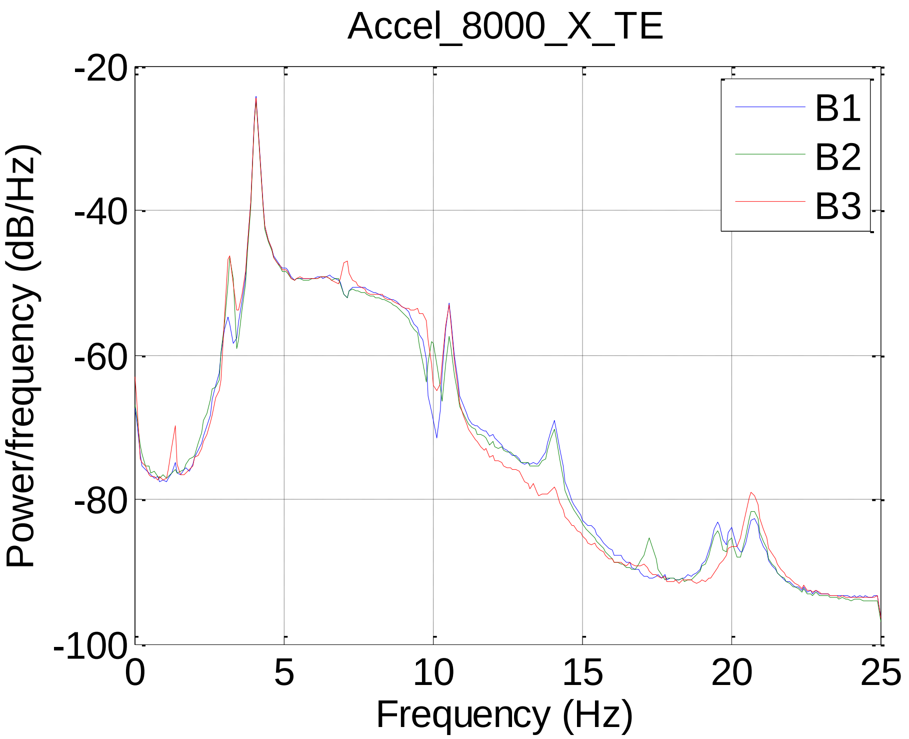

Figure 3.11 Parked rotor PSD of flapwise acceleration at 8000 mm span with logarithmic sine sweep excitation.

3.3.2 Sine Sweep during Power Production

Similar sinusoidal flap motion with logarithmic sweep of frequency was applied while the rotor was turning at 55 rpm and the generator was producing power. As seen in Figure 3.12 and Figure 3.13, the primary structural resonance is present but the peak is much wider which indicates increased damping resulting from the addition of aerodynamic damping forces. An upshift in this peak's frequency is observed from 4.1 Hz in the non-rotating test to 4.4 Hz in the power production test. This upshift is likely due to rotational stiffening of the blades. The spectrogram has a number of vertical lines at regular intervals which are multiples of the rotational frequency (55 rpm or 0.92 Hz).

Logarithmic sweep of the flap excitation frequency was a useful tool for system characterization in both the parked and power production cases.

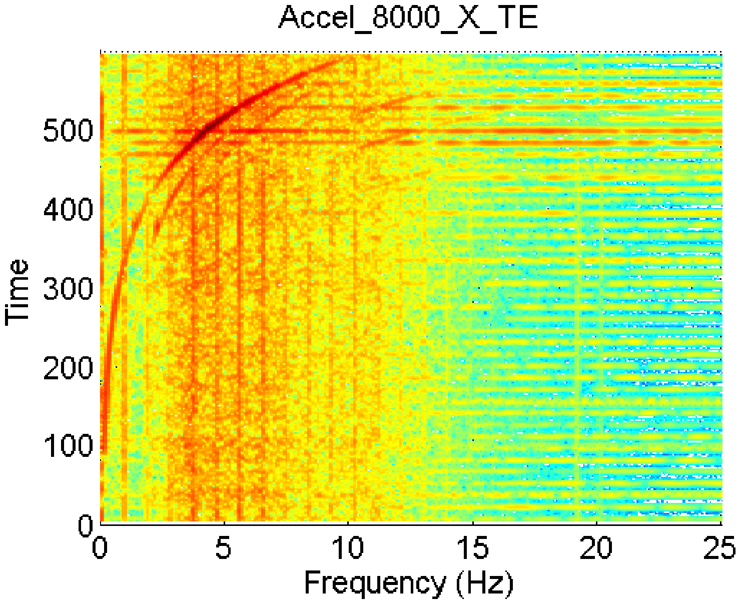

Figure 3.12 Power production spectrogram (waterfall plot) of flapwise acceleration at 8000 mm span with logarithmic sine sweep.

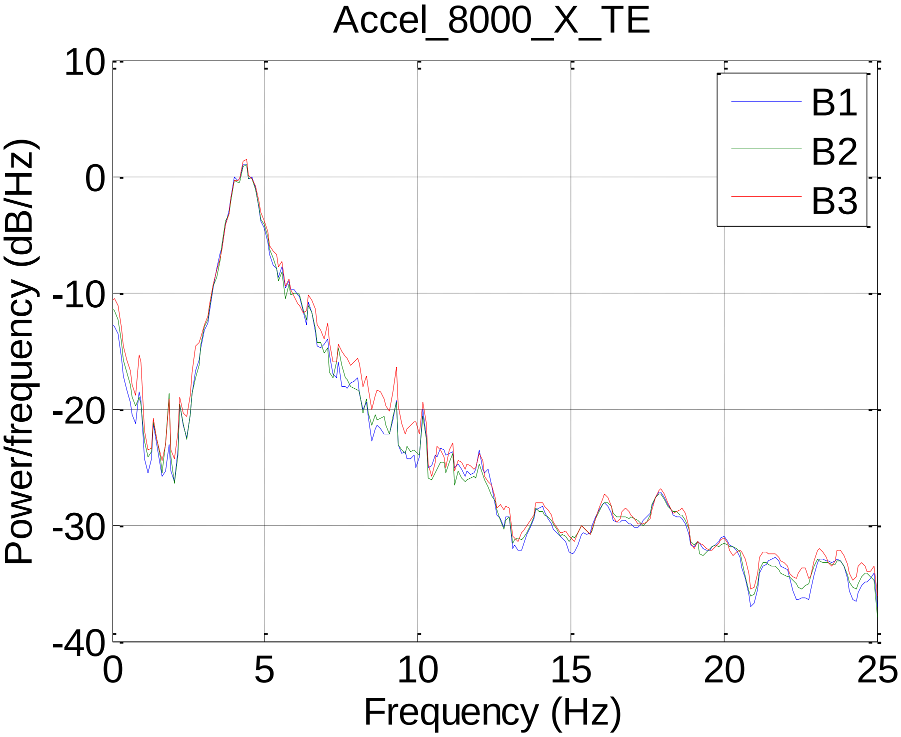

Figure 3.13 Power production PSD of flapwise acceleration at 8000 mm span with logarithmic sine sweep.

Hub mounted video cameras pointed toward the blade tips were used to capture the tip motion during some of the test runs including one power production sine sweep test. Figure 3.14 is a sequence of still images over one flap cycle when the blade was excited at the main resonance frequency. The blade tip is initially downwind or to the left (frame 1) when the flaps begin moving toward the lower pressure surface. The reduced lift results in tip movement upwind or to the right (frame 5). As the flaps move back to their initial position, the blade tip also moves back to the initial position (frame 9).

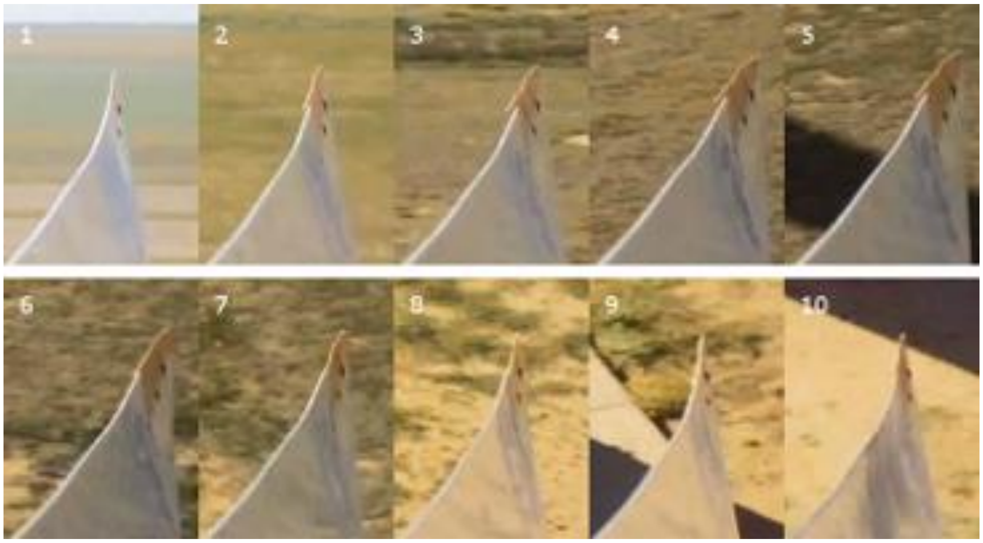

Figure 3.14 This sequence of video frames of a sinusoidal flap motion shows the blade tip moving from a downwind position (1) to an upwind position (5) and back to the downwind position (9) during one flap cycle.

3.4 Flap Drive System Dynamics

The flaps were actuated in various motions, both with and without the rotor spinning, to characterize the motor drive system.

3.4.1 Flap Drive with Rotor Stopped

A simple sinusoidal flap motion of fixed amplitude and frequency was the first step to obtain the loads on the flap motors in the absence of significant aerodynamic forces. The electrical current demanded by the motor controllers was expected to result mainly from the torque required to overcome friction and accelerate the flaps to track the desired flap position.

Figure 3.15 plots the motor current demand against motor shaft angle during a 1 Hz sinusoidal motion with 5 degree amplitude. (The empty subplots indicate data acquisition failures.)

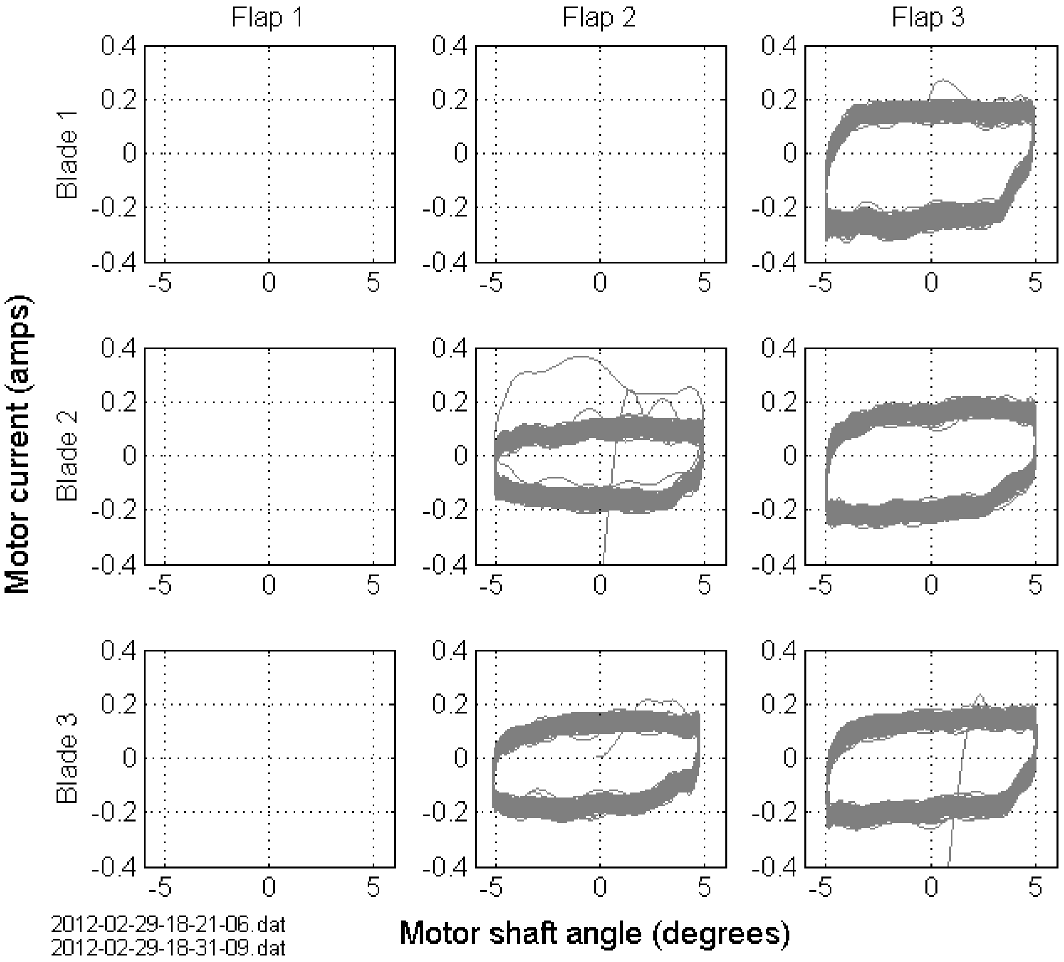

Figure 3.15 Motor current demand during sinusoidal flap motion at 1 Hz frequency and 5 degree amplitude (with parked rotor).

A simple mass-spring-damper model of the flap drive system was constructed to help understand the key parameters contributing to the observed behavior. The equation of motion for this one degree-of-freedom rotational system was obtained by application of Newton’s second law:

$$J\ddot{\theta} = \Sigma T$$
$$J\ddot{\theta} = -c_{viscous}\dot{\theta} - c_{coulomb}sign(\dot{\theta}) - T_{aero}(\theta) + T_{motor}$$

The flap angle, speed, and acceleration are represented by $\theta, \dot{\theta},$ and $\ddot{\theta}$ respectively. The acceleration term coefficient, *J*, represents the lumped rotational inertia of the flap and other rotating components. The first damping term coefficient, $c_{viscous}$, represents viscous-type damping proportional to the rate of angular motion. The second damping term coefficient, $c_{coulomb}$, represents Coulomb-type damping which depends only on the direction of angular motion. The “spring force” term, T_{aero}, was chosen to represent the aerodynamic hinge moment acting on the flap and was given by a nonlinear function. Although other spring-like forces could exist they can be treated as negligible or rolled into the aerodynamic torque term. The final term, T_{motor}, is the torque applied by the motor and it is determined by a PID controller which regulates the motor shaft position.

The electrical current required by the motor is proportional to its shaft torque and depends on the following motor parameters:

- Motor torque constant, k_m = 0.0346 Nm/A
- Gear ratio, N = 66.22
- Gearhead efficiency, $\eta = 0.7$

$$I_{motor} = \left(\frac{1}{k_m}\right)\left(\frac{1}{N\eta}\right)T_{motor}$$

The relative contribution of viscous and Coulomb damping was estimated by varying each damping coefficient in the model. The aerodynamic hinge moment term was set to zero for any simulations with the turbine rotor stopped.

Figure 3.16 shows how the flap drive model responded to changes in Coulomb damping. In the absence of any significant viscous damping, the shape of the current-angle cycle was rectangular. The upper left and lower right corners of the cycle have small oscillations where the flap motion was changing directions. (The oscillation at 0 degree shaft angle was a startup transient in the simulation.)

Figure 3.17 shows how the flap drive model responded to changes in viscous damping. In the absence of any significant Coulomb damping, the shape of the current-angle cycle was elliptical. Viscous damping tended to reduce oscillations and improve numerical stability of the model.

The field test results given in Figure 3.15 show a mostly rectangular cycle which indicates that Coulomb damping was likely the primary force involved and $c_{coulomb}$ must be about 0.3 to make the simulation model match the results. However, there were obviously other dynamics involved to produce the observed results. Wind loading may have been a factor and the motor controller itself may have produced some of the oscillatory behavior. In the simulation model, gains of the PID controller were tuned and scaling parameters were adjusted until some additional features appeared in the cycle. Figure 3.18 shows one case in which the controller tended to respond a bit chaotically at the upper left and lower right corners of the cycle. This somewhat matches the observed behavior but was likely the result of numerical stability issues. Additional modelling efforts would be required to obtain a tuned simulation model.

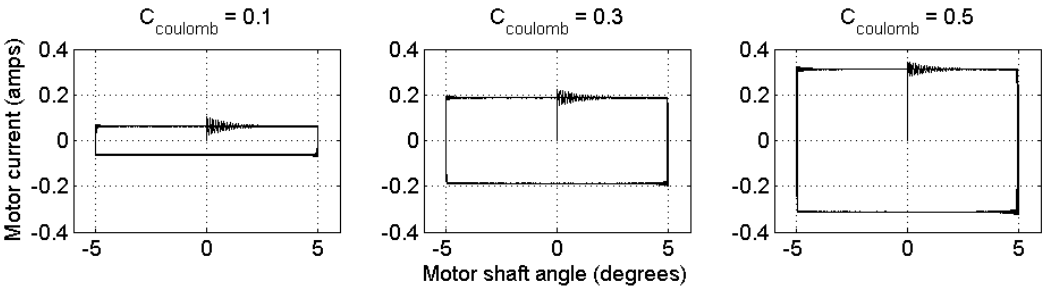

Figure 3.16 Flap drive simulation with primarily Coulomb damping forces.

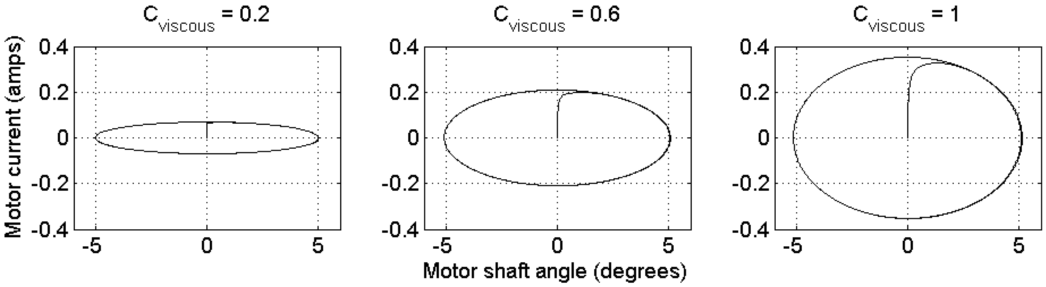

Figure 3.17 Flap drive simulation with primarily viscous damping forces.

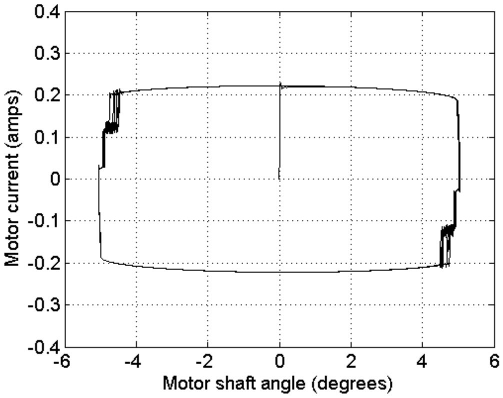

Figure 3.18 Flap drive simulation with numerical instability at two points in cycle.

A sinusoidal flap motion with logarithmic sweep of frequency was a simple and effective means of exciting system dynamics and determining the frequency-response of the motors. Figure 3.19 shows the motor shaft angle response to a 0.1 – 10 Hz logarithmic sweep command. Towards the end of the sweep, a flap drive resonance was excited and the amplitude rose above the commanded value and then tapered off quickly. Frequency domain analysis results, which are plotted in Figure 3.20, show that the peak amplitude gain between the motor shaft angle and the angle setpoint command occurred at 6.5 Hz. The phase shift between the flap command and shaft response deviated from zero degrees above 6 Hz, which means that the useful actuation frequency range of the motor flap drive system was 0 to 6 Hz.

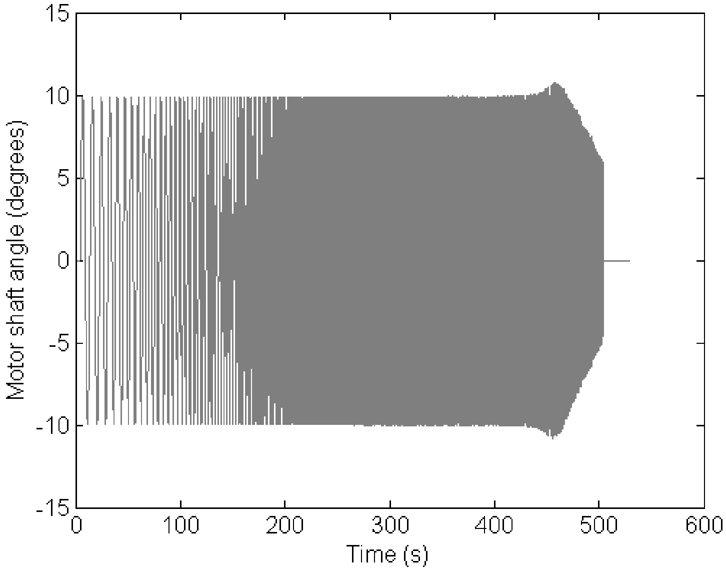

Figure 3.19 Motor shaft angle response to logarithmic frequency sweep.

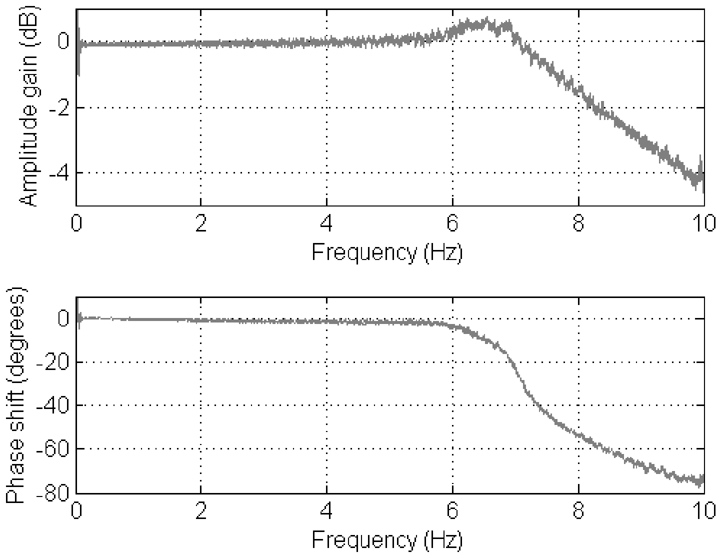

Figure 3.20 Amplitude gain and phase shift between motor shaft response and angle command.

Figure 3.21 shows the amplitude gain and phase shift between the motor current and motor shaft angle. Additional motor current was required above 3 Hz and the phase shift began to increase at around 1 Hz. This onset of phase shift at a rather low frequency is unfortunate because the excitation frequency for breakdown of the quasi-steady aerodynamic assumption is also near 1 Hz for the SMART rotor. If the motor current phase shift had been constant out to a higher frequency then any phase shift caused by unsteady aerodynamics forces would have been more easily identified.

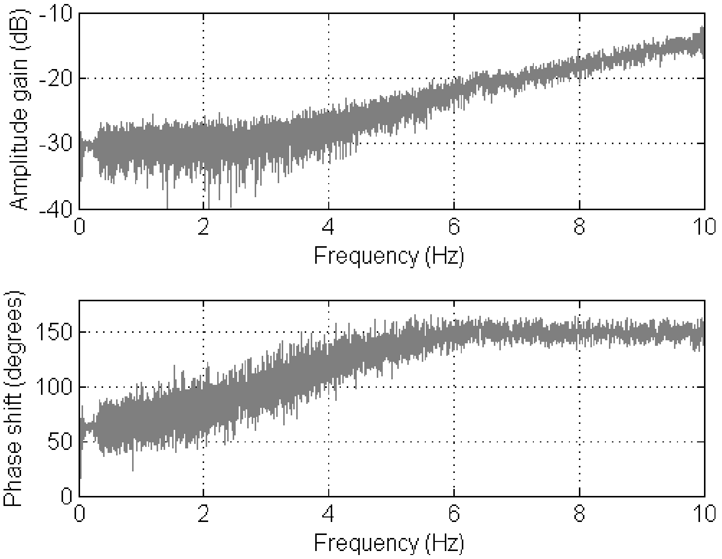

Figure 3.21 Amplitude gain and phase shift between motor current and motor shaft angle.

3.4.2 Flap Drive during Power Production

With the rotor spinning and producing power, the flap controller was stepped through a series of sinusoidal flap motions each with a different frequency. The electrical current demanded by the motor controllers was expected to be a combination of aerodynamic forces and other effects such as friction in the flap drive system.

Figure 3.22 plots the motor current demand against motor shaft angle for Blade 3. Frequency of the sinusoidal motions ranged from 0.1 Hz to 6 Hz and the amplitude was 5 degrees. A transition occurs in the shape of the current-angle cycles between the actuation frequencies of 0.8 and 1.5 Hz. The reduced frequency of the flap excitation was calculated as described in Section 2.1.2 to be $0.001 < k < 0.08$. The 0.8 Hz sinusoidal motion has a reduced frequency of about 0.01 which corresponds to the upper limit $O(0.01)$ for a quasi-steady aerodynamic assumption. However, it must be noted again that the phase shift between motor current and motor shaft angle also begins to increase at around 1 Hz excitation frequency and thus the onset of unsteady aerodynamic behavior cannot be easily identified from motor current phase. Additional testing must be performed with appropriate measurements; these measurements may include aerodynamic inflow, surface pressure, or actuator current (assuming the actuator’s inherent phase relationship can be chosen to avoid interference).

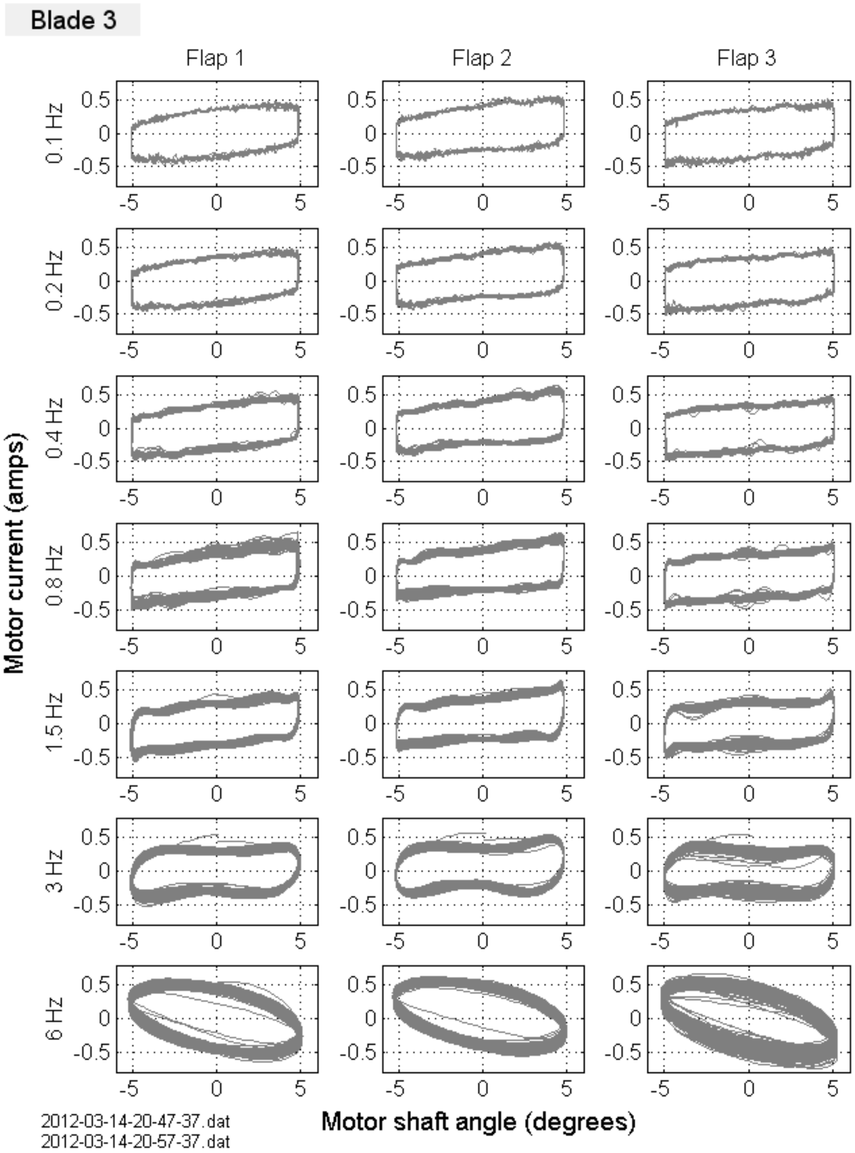

Figure 3.22 Motor current demand for various frequencies of sinusoidal motion (during power production).

At low frequencies, the rectangular shape caused by Coulomb damping was again the predominant characteristic. However, with aerodynamic forces involved, the rectangle became a rhomboid which was skewed along a trendline with positive slope.

The aerodynamic hinge moment in the simulation model was represented by a nonlinear function of the flap angle. Using XFOIL [49], the hinge moment about the flap hinge line was estimated for a range of operating conditions and flap angles. Figure 3.23 shows the hinge moment coefficient at three angles of attack for the airfoil at 7.8 m span. Similar results were obtained inboard and outboard of this span location and so, for simplicity, only one equation for the moment coefficient was carried forward. The quadratic fit line is given by equation (3.3).

$$f(\theta) = (-5.6989 \times 10^{-6})\theta^2 + (4.5118 \times 10^{-4})\theta + 0.0052 \quad (3.3)$$

The hinge moment varies with span according to equation (3.4), where ρ is the air density, V is the local air velocity, and c is the chord length.

$$\text{Hinge moment per unit span} = \frac{1}{2}\rho V^2 c^2 \cdot f(\theta) \quad (3.4)$$

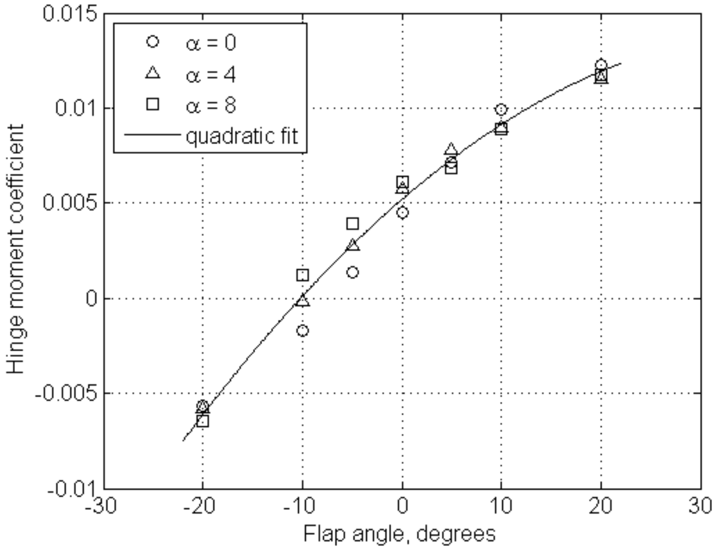

Figure 3.23 Hinge moment coefficient at 7.8 m span.

In the flap drive simulation model, the following fixed parameters were chosen:

- Air density ρ = 1.088 kg/m^3
- Chord c = 0.2613 m
- Wind speed of 9 m/s, which produces a local air velocity (at 8.6 m radius) of V = 50.32 m/s
- Total scale factor $\frac{1}{2}\rho V^2 c^2 = 94$ Nm (per meter span)

The length of each flap was 2 feet or 1.8288 meters.

Combining these parameter values with equations (3.3) and (3.4), the flap drive simulation model produced a similar rhomboid shape for motor current versus shaft angle. However, the result was offset by about 0.5 amps in the positive direction on the vertical axis. Zeroing out the last term in equation (3.3) brought the results back down into the range observed in Figure 3.22. It is not clear why the predicted offset in motor current did not appear in the data. One possibility is that the flap angle differs from the motor shaft angle measurement and therefore equation (3.3) must be offset with respect to the flap angle argument rather than zeroing out the constant offset term. An offset of -10 degrees between the motor shaft angle and flap angle would shift the curve in Figure 3.23 to the right and produce roughly the same effect as shifting the curve down by

0.005 amps. Video of the flaps during turbine operation did reveal a flap offset in the negative angle direction but the amount of offset cannot be judged accurately.

Ideally, the angle of the flap itself would have been measured but the space constraints and project timeline prevented integration of dedicated angle sensors for the flaps. In addition, the linkage mechanism between the motor and flap could be redesigned to reduce the possibility of relative motion.

Having addressed the offset issue, the simulation parameters were then adjusted to obtain similar rhomboid side lengths. The Coulomb damping coefficient needed to be increased from 0.3 to 0.4, which could be explained by increased lateral force on the flap hinge causing the sleeve bearing friction to rise. A viscous damping coefficient in the range of 0.1 to 0.3 appeared to produce a similar rounded top to the rhomboid. Figure 3.24 shows the simulation result at three different frequencies of sinusoidal motion.

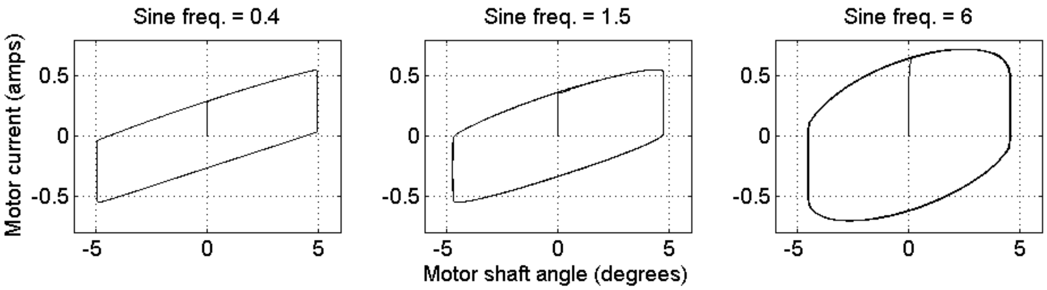

Figure 3.24 Flap drive simulation with aerodynamic hinge moment included.

The shape was roughly captured at lower actuation frequencies where the assumption of quasi-steady aerodynamics applies and the inherent motor current phase shift was small. Additional analysis and modelling efforts would be required to obtain a tuned flap drive simulation model which captures the observed frequency dependence.

3.5 Power Curves

The following power curves were obtained from 5 hours of test data acquired on a single day. The wind direction ranged from approximately 170 to 260 degrees with an average direction of 214.5 degrees which matches the site's prevailing wind direction of 215 degrees. Thus, the center meteorological tower was directly in line with the turbine.

The hub height wind cup, BAHHC, provided the wind speed measurement for the power curves. Computing the cross-correlation with the nacelle wind cup, the average time delay for the wind to reach the turbine was 3.62 seconds. This time delay was applied to the wind speed signal to minimize error when reporting the generator power measurements versus wind speed.

A sequence of step motions between the 0 degree flap position and ± 5, 10, 15, and 20 degrees was employed to spread the wind speed distribution evenly among the various flap positions.

The duration of each step was 30 seconds and the first 2 seconds of data after the step transition was discarded to remove the initial power transients.

Figure 3.25 compares the SMART rotor's generator power at the 0 degree flap setting with the generator power of a previous CX-100 test. A power loss ranging from 7 to 15% was experienced and early initiation of stall is evident at around 13 m/s. The bend in the power curve below 6 m/s was likely caused by inaccuracy of the wind cup at low wind speeds due to friction and inertia.

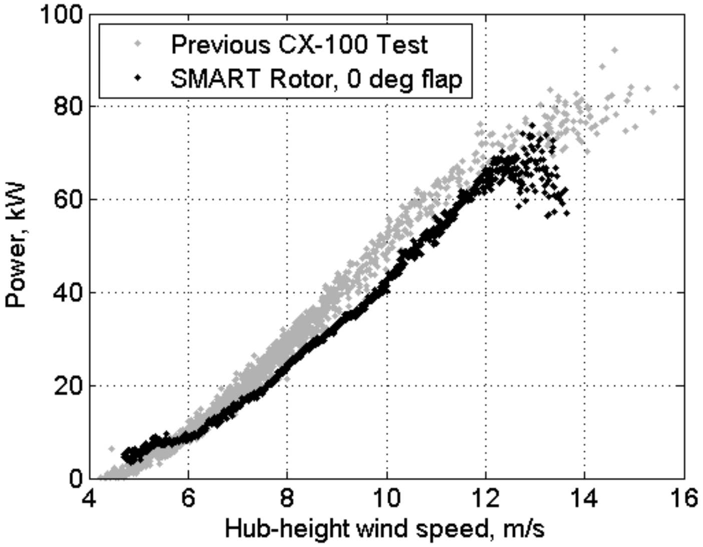

Figure 3.25 Power curve at 0 degree flap compared to unmodified rotor.

Figure 3.26 shows the power output at each flap position. Positive flap angles produced roughly the same power with some excursions having an 8 to 14% increase. Negative flap angles produced noticeable decreases in power ranging from -5 kW at -10 degree flap to -10 kW at -20 degree flap. Of particular interest are the stall behaviors observed for the 10 degree and -15 degree flap settings. It is not clear why the 10 degree setting consistently initiated an early blade stall whereas the 15 and 20 degree settings behaved much the same as the 0 degree setting.
The -15 degree setting appears to have three groups of points at stall which may be related to dynamic stall effects.

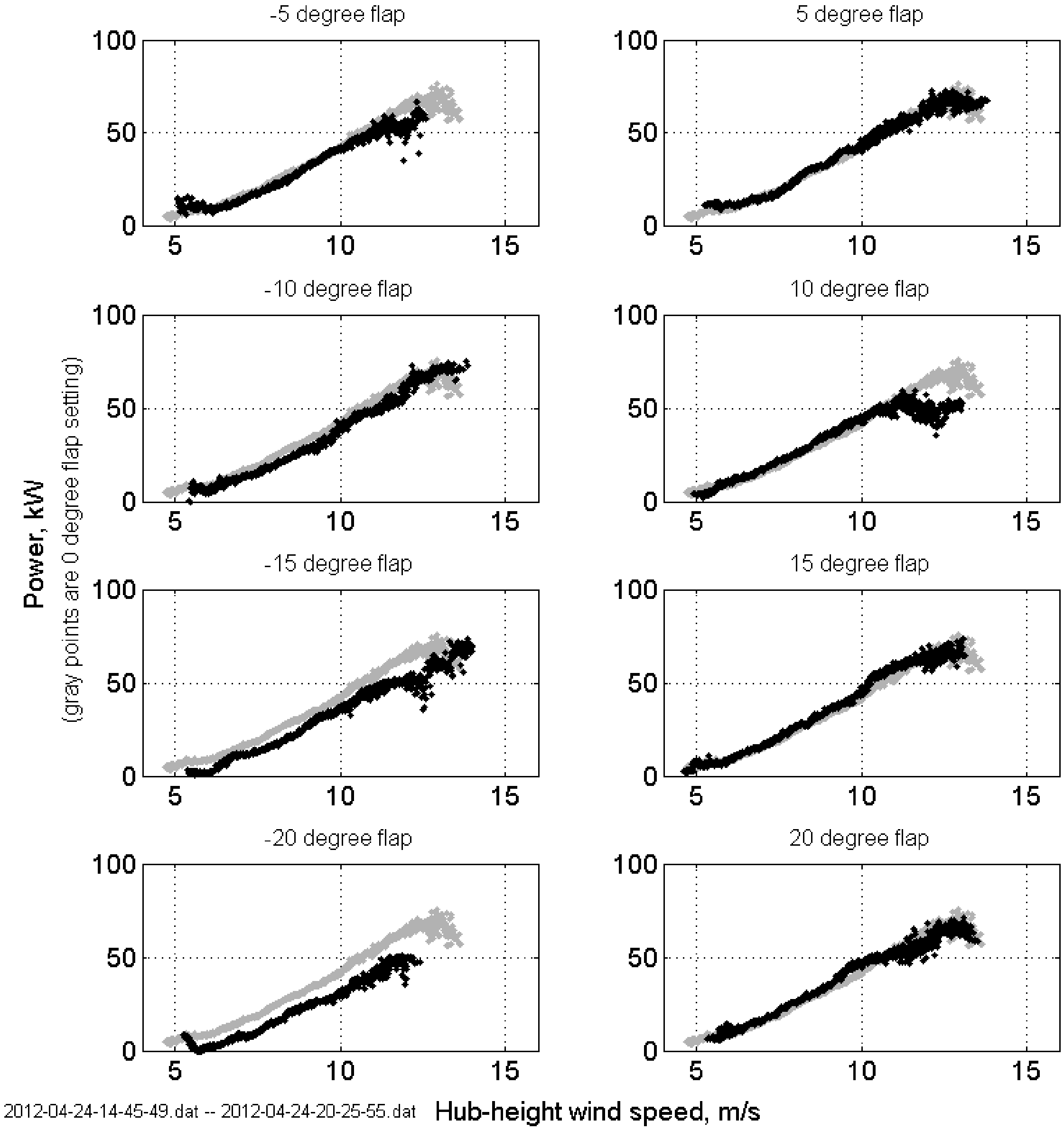

Figure 3.26 Power curve of each flap setting compared to the 0 degree setting.

3.5 Conclusions

The control capability of the trailing-edge flaps was observed in the blade strain response at three-quarters span and was shown to be roughly 114% of the strain at this span that results from power production thrust loads. Influence on strain at the blade root was roughly 50% of the strain that results from power production thrust loads.

Transient response of the wind turbine to step motions of the flaps showed that step excitation is an effective method of system characterization which revealed a combined aerodynamic and structure damping on the order of 1% to 3% of critical damping. Response time delays were observed which are important for evaluating the accuracy of simulation tools that support active aerodynamic research.

The logarithmic sine sweep was shown to be a useful tool for system characterization of both the operational turbine and the flap drive subsystem. Methods to obtain accurate models of the system dynamics are important for the success of future closed-loop active rotor control.

4. DATA ACQUISITION SYSTEM

4.1 Introduction

Understanding the architecture of the data acquisition system that was used in this project is critical for understanding the required signal processing. The system consisted of four acquisition subsystems each having an independent clock. Because the clocks were independent, the timing of data samples was not completely synchronized between the subsystems. In addition, within each subsystem some of the data channels exhibited an additional time offset relative to the other subsystem channels. All of these timing characteristics are documented in the following tables and discussion. The four subsystems are now described briefly and identified by name.

The first subsystem was physically located at ground level in the “ground-based-unit” or GBU. This unit acquired all signals on the non-rotating side of the turbine and also signals from the meteorological towers. The other three subsystems were physically located on the rotor in the “rotor-based-unit” or RBU.

The GBU subsystem hardware was a KAM-500 from ACRA Control [50] and was named “GBU”. The first of the three RBU subsystems was another KAM-500 unit which was named “ACRA” and the second RBU subsystem was a cRIO-9025 from National Instruments [51] which was named “cRIO”. The third RBU subsystem was an sm130 fiber optic interrogator from Micron Optics [52] which was named “Micron Optics Interrogator” or “MOI”. Additional information on the subsystem hardware modules and software configuration can be found in the Appendix A on ATLAS Configuration Settings.

In the turbine control building, a desktop computer running the ATLAS II software package [53] controlled the four subsystems and merged their four data streams together. “ATLAS” stands for “Accurate GPS Time-Linked Acquisition System” and the software had originally been developed to work with the ACRA-based hardware subsystems to enable time-linked acquisition from systems that could not be physically linked to each other. The idea was to use GPS technology to provide an accurate time source to synchronize data instead of a physical hardware “trigger”. Special hardware was developed for the ACRA subsystems to integrate GPS time into their data acquisition capabilities.

For the more recent Sensor Blade and SMART Rotor tests, ATLAS was modified to also incorporate data from the National Instruments cRIO-9025 and Micron Optics sm130. A S.E.A. [54] GSM / GPS Communication Module (cRIO Gxxx+) provided the GPS time source for the cRIO. Although the MOI does not have a GPS input, the cRIO handles its data acquisition and thus the two subsystems have essentially the same sample clock.

Although the GPS time-linking strategy implemented in ATLAS was adequate for the LIST campaign [55] – which relied mostly on ten-minute averages – it was discovered that the ATLAS software employed in the Sensor Blade and SMART Rotor tests did not provide direct sample-to-sample alignment between the four subsystem data streams. Fortunately, in the SMART Rotor test, some of the sensor signals where shared between the cRIO and ACRA to provide a way to re-align the data streams. In addition, the rotor’s inertial measurement unit (IMU) detected the rotor’s orientation with respect to gravity and thus provided a surrogate for the rotor azimuth signal measured by the GBU and a way to re-align the GBU and RBU subsystems.

4.2 Channel List

This section provides a brief overview of the list of channels acquired during the SMART Rotor field test. The purpose is to provide a point of reference for discussion of data channels in subsequent sections and to highlight the signals which are most important for the resampling and realignment post-processing steps.

Table 4.1 organizes the channels by the four subsystems previously described and, within each subsystem, identifies the following groups: GPS signals, Sync signals (data frame synchronization), general sensor signals, and specific sensor signals important for realignment. These alignment signals are the following: Azimuth and IMU, Blade 1 Strains (shared signals between ACRA and cRIO), and Impact Hammer (shared signal between ACRA and cRIO).

To distinguish between the subsystem clocks in data post-processing, each clock was given a “Clock ID” number ranging from one to three. The cRIO, ACRA, and GBU were given clock ID numbers 1, 2, and 3, respectively. Because the MOI sampling was handled by the cRIO, it also used Clock ID 1.

Table 4.2 presents the full list of channels.

Table 4.1 Data acquisition subsystem channel groups.

Subsystem	Channel	Description	Subsystem Clock ID
	1	TimeStamp	1
GBU	2 .. 5	<gbu sync>	3
	6 .. 21	<gbu signals>	
	22	AZIMUTH_ANGLE	
	23 .. 38	<gbu signals>	
	39 .. 43	<gbu gps>	
ACRA	44 .. 47	<acra sync>	2
	48 .. 54	B1 Strains	
	55 .. 97	<acra signals>	
	98 .. 100	DAQ_IMU	
	101	Impact Hammer	
	102 .. 106	<acra gps>	
cRIO	107 .. 110	<crio sync>	1
	111 .. 115	<crio gps>	
	116 .. 139	<crio signals>	
	140 .. 146	B1 Strains	
	147 .. 149	DAQ_IMU	
	150	Impact Hammer	
MOI	151 .. 186	<moi signals>	1

Table 4.2 Channel List

Index	Signal Name	Units
1	TimeStamp	Seconds
2	SYNC1	numeric
3	SYNC2	numeric
4	SFID	numeric
5	gbu_J2_enc_12345	numeric
6	BAHHATIU	m/s
7	BAHHATIV	m/s
8	BAHHATIW	m/s
9	BAHHATIT	C
10	BAHHC	m/s
11	BAHHV	deg.
12	BATP	C
13	BADTP	C
14	OHHC	m/s
15	OHHV	deg.
16	BAROMETRIC_PRESSURE	kPa
17	BA2mC	m/s
18	On_Off	volts
19	GENERATOR_POWER	kW
20	PLC_BRAKE_M	volts
21	YAW_ANGLE	degrees
22	AZIMUTH_ANGLE	degrees
23	ROTATIONAL_SPEED	rpm
24	PLC_BRAKE_e	volts
25	BTNACC	m/s
26	NACELLE_IMU_AX	G
27	NACELLE_IMU_AY	G
28	NACELLE_IMU_AZ	G
29	NACELLE_IMU_RX	deg/sec
30	NACELLE_IMU_RY	deg/sec
31	NACELLE_IMU_RZ	deg/sec
32	LSS_SPEED	rpm
33	TOWER_BENDING_FA	ustrain
34	TOWER_BENDING_SS	ustrain
35	BAHHEC	m/s
36	BAHHW_Sonic	m/s
37	BARTC	m/s
38	BARBC	m/s
39	TIME_GBU_GPS_Month_Day	counts
40	TIME_GBU_GPS_Year	counts
41	TIME_GBU_GPS_Hour_Minute	counts
42	TIME_GBU_GPS_Second	counts
43	TIME_GBU_GPS_Millisecond	counts
44	SYNC1	counts
45	SYNC2	counts
46	SFID	counts
47	ACRA_1_J2_enc_0	counts
48	B1_H1_Strain_0350_Z_HP	ustrain
49	B1_H1_Strain_0350_Z_LP	ustrain
50	B1_H1_Strain_2250_Z_HP	ustrain
51	B1_H1_Strain_4500_Z_HP	ustrain
52	B1_H1_Strain_6750_Z_HP	ustrain
53	B1_H1_Strain_0350_Z_TE	ustrain
54	B1_H1_Strain_0350_Z_LE	ustrain
55	B2_H2_Strain_0350_Z_HP	ustrain
56	B2_H2_Strain_0350_Z_LP	ustrain
57	B2_H2_Strain_2250_Z_HP	ustrain
58	B2_H2_Strain_4500_Z_HP	ustrain
59	B2_H2_Strain_6750_Z_HP	ustrain
60	B2_H2_Strain_0350_Z_TE	ustrain
61	B2_H2_Strain_0350_Z_LE	ustrain
62	B3_H3_Strain_0350_Z_HP	ustrain
63	B3_H3_Strain_0350_Z_LP	ustrain
64	B3_H3_Strain_2250_Z_HP	ustrain
65	B3_H3_Strain_4500_Z_HP	ustrain
66	B3_H3_Strain_6750_Z_HP	ustrain
67	B3_H3_Strain_0350_Z_TE	counts
68	B3_H3_Strain_0350_Z_LE	ustrain
69	H1_Strain_Z_Flap	counts
70	H1_Strain_Z_Edge	counts
71	H2_Strain_Z_Flap	counts
72	H2_Strain_Z_Edge	counts
73	H3_Strain_Z_Flap	counts
74	H3_Strain_Z_Edge	counts
75	B1_Motor1_Position	voltage
76	B1_Motor1_Current	voltage
77	B2_Motor1_Position	voltage
78	B2_Motor1_Current	voltage
79	B3_Motor1_Position	voltage
80	B3_Motor1_Current	voltage
81	B1_Motor2_Position	voltage
82	B1_Motor2_Current	voltage
83	B2_Motor2_Position	voltage
84	B2_Motor2_Current	voltage
85	B3_Motor2_Position	voltage
86	B3_Motor2_Current	voltage
87	B1_Motor3_Position	voltage
88	B1_Motor3_Current	voltage
89	B2_Motor3_Position	voltage
90	B2_Motor3__Current	voltage
91	B3_Motor3_Position	voltage
92	B3_Motor3_Current	voltage
93	Athena_AnalogOut1	voltage
94	Athena_AnalogOut2	voltage

Table 4.2 Channel List (continued)

Index	Signal Name	Units
95	Athena_AnalogOut3	voltage
96	Cntrlbx_Extra1	voltage
97	Cntrlbx_Extra2	voltage
98	DAQ_IMU_X	g
99	DAQ_IMU_Y	g
100	DAQ_IMU_Z	g
101	Impact_Hammer	voltage
102	Time_GPS_Month_Day	counts
103	Time_GPS_Year	counts
104	Time_GPS_Hour_Minute	counts
105	Time_GPS_Second	counts
106	Time_GPS_Millisecond	counts
107	SYNC1	counts
108	SYNC2	counts
109	SFID	counts
110	cRIO_1_J2_ctl_Id_12345	counts
111	cRIO_gps__Month_Day	counts
112	cRIO_gps__Year	counts
113	cRIO_gps__Hour_Minutes	counts
114	cRIO_gps__Seconds	counts
115	cRIO_gps__Milliseconds	counts
116	B1_H1_Accel_2000_X_HP	g
117	B1_H1_Accel_2000_Y_HP	g
118	B1_H1_Accel_2000_Z_HP	g
119	B1_H1_Accel_2000_X_TE	g
120	B1_H1_Accel_8000_X_HP	g
121	B1_H1_Accel_8000_Y_HP	g
122	B1_H1_Accel_8000_Z_HP	g
123	B1_H1_Accel_8000_X_TE	g
124	B2_H2_Accel_2000_X_HP	g
125	B2_H2_Accel_2000_Y_HP	g
126	B2_H2_Accel_2000_Z_HP	g
127	B2_H2_Accel_2000_X_TE	g
128	B2_H2_Accel_8000_X_HP	g
129	B2_H2_Accel_8000_Y_HP	g
130	B2_H2_Accel_8000_Z_HP	g
131	B2_H2_Accel_8000_X_TE	g
132	B3_H3_Accel_2000_X_HP	g
133	B3_H3_Accel_2000_Y_HP	g
134	B3_H3_Accel_2000_Z_HP	g
135	B3_H3_Accel_2000_X_TE	g
136	B3_H3_Accel_8000_X_HP	g
137	B3_H3_Accel_8000_Y_HP	g
138	B3_H3_Accel_8000_Z_HP	g
139	B3_H3_Accel_8000_X_TE	g
140	B1_H1_Strain_0350_Z_HP	volts

Index	Signal Name	Units
141	B1_H1_Strain_0350_Z_LP	volts
142	B1_H1_Strain_2250_Z_HP	volts
143	B1_H1_Strain_4500_Z_HP	volts
144	B1_H1_Strain_6750_Z_HP	volts
145	B1_H1_Strain_0350_Z_TE	volts
146	B1_H1_Strain_0350_Z_LE	volts
147	DAQ_IMU_X_cRIO	volts
148	DAQ_IMU_Y_cRIO	volts
149	DAQ_IMU_Z_cRIO	volts
150	Impact_Hammer_cRIO	volts
151	Ch0-S0	counts
152	Ch0-S1	counts
153	Ch0-S2	counts
154	Ch0-S3	counts
155	Ch0-S4	counts
156	Ch0-S5	counts
157	Ch0-S6	counts
158	Ch0-S7	counts
159	Ch0-S8	counts
160	Ch0-S9	counts
161	Ch0-S10	counts
162	Ch0-S11	counts
163	Ch1-S0	counts
164	Ch1-S1	counts
165	Ch1-S2	counts
166	Ch1-S3	counts
167	Ch1-S4	counts
168	Ch1-S5	counts
169	Ch1-S6	counts
170	Ch1-S7	counts
171	Ch1-S8	counts
172	Ch1-S9	counts
173	Ch1-S10	counts
174	Ch1-S11	counts
175	Ch2-S0	counts
176	Ch2-S1	counts
177	Ch2-S2	counts
178	Ch2-S3	counts
179	Ch2-S4	counts
180	Ch2-S5	counts
181	Ch2-S6	counts
182	Ch2-S7	counts
183	Ch2-S8	counts
184	Ch2-S9	counts
185	Ch2-S10	counts
186	Ch2-S11	counts

4.3 Time Synchronization

When a continuous analog signal is sampled by two different analog-to-digital converters, the output samples will most likely *not* align perfectly with each other. In the extreme case of two sampling frequencies widely separated from one another, as in Figure 4.1, it is obvious that the samples do not align. However, misalignment also occurs when sampling frequencies differ by only a fraction of a percent. For example, samples at 50 Hz and 50.02 Hz differ in sample spacing by only 8 microseconds. At the end of a 4-hour test, however, sample number 720,000 from each system will differ in timestamp by nearly 6 seconds.

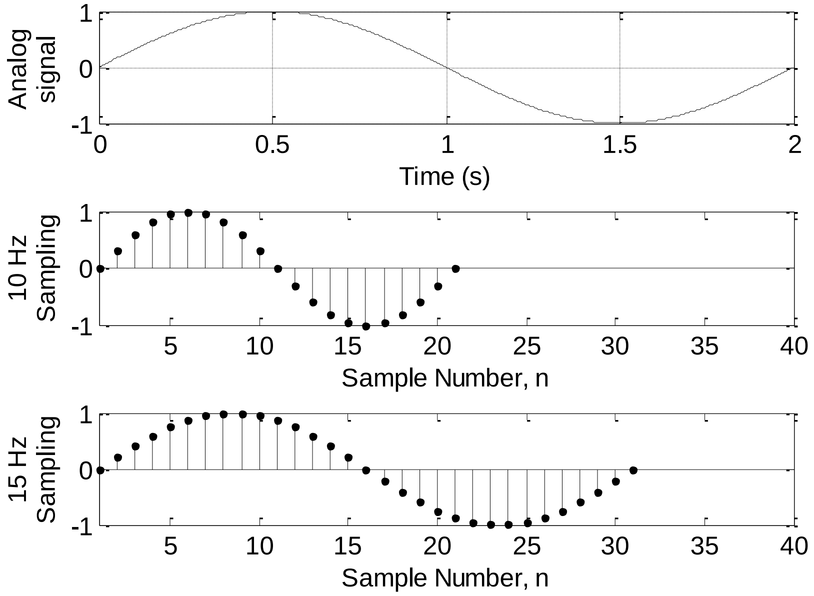

Figure 4.1 Example of samples acquired at different rates

This sample alignment problem is typically solved by triggering both systems to sample at the same instant. In the case of the SMART Rotor field test, implementing a reliable trigger across the nacelle-rotor boundary was not feasible, and so each subsystem in the full turbine data acquisition system samples at its independent clock frequency. Sample alignment occurs in post processing, either by resampling with a universal sample spacing or by generating independent time vectors (in cases where only temporal alignment is necessary and not direct sample-to-sample alignment).

Including an accurate time source such as GPS time in the data frames from each subsystem can be helpful in post processing to verify the exact sampling frequency. In essence, an exact time source provides a timed “window” with a constant and accurate width. The number of sample points falling within a series of 1-second windows will, on average, be equal to the sampling frequency. For example, in Figure 4.2 the 5.5 Hz sampling frequency produces six samples in the interval [0, 1) and five samples in the interval [1, 2)[1]. This 6-5 pattern repeats, and the long-term average is 5.5 samples per second. If the number of windows happens to match the repeating pattern then the answer will be exact. Otherwise, the number of samples included in the average must be great enough that cutting the repeating pattern before the end does not significantly change the average.

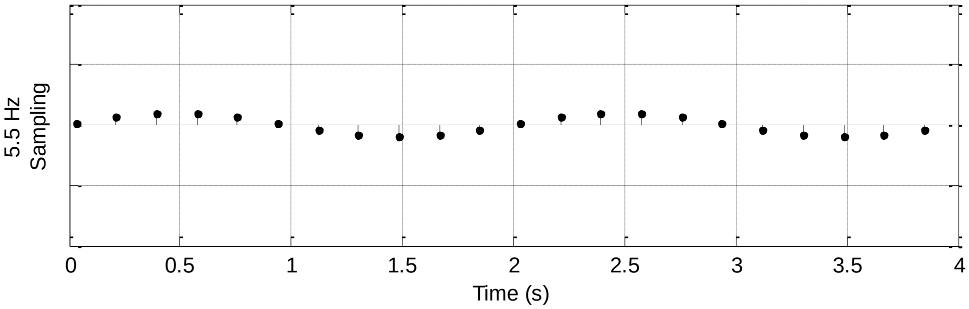

Figure 4.2 Example for sample rate determination

Instead of counting samples inside 1-second windows, it is likely more efficient to take the following approach. Given a series of samples, their GPS time stamps are converted into the number of seconds since the first sample. Plotting this array of time values against the sample number of each sample gives a line with a slope which corresponds to the sample period measured in seconds per sample. The line will have a stair-step appearance because the GPS time does not update with every sample. However, a least-square fit of a straight line will easily identify the slope which characterizes the stair-step.

After the sample period of each subsystem has been identified, it is possible to resample every data channel so that they have a common sample rate. This eliminates the sample drift caused by unequal sample spacing; however, the signals must still be synchronized in time.

GPS time is not very useful for temporal alignment of two signals because the update rate is typically 1 Hz and every sample receives the same timestamp until another GPS update occurs. To be useful for temporal alignment, the subsystem clocks need to be continually resynchronized to GPS time and sampling must begin at a known instant in time which is consistent across all subsystems.

In the absence of such a system directly controlled by GPS time, the sample clocks must be re-aligned using features within the data itself. This is why certain signals were measured by both the ACRA and cRIO. Calculating the cross-correlation of these signals identifies the amount of time shift required to maximize the agreement between the signals.

---

[1] The square bracket "[" is used to indicate that a sample at the interval boundary would be included in the interval and parenthesis ")" to indicate the sample would not be included.

4.4 Data Dropouts

Data dropouts, or the occasional loss of a frame of data, were experienced in the field test. In expectation of this possibility, the GBU, ACRA, and cRIO each created a “sequential frame ID” or SFID which was packaged with the data frames. The SFID was a counter which incremented every time the hardware acquired a frame of data. It was incremented whether or not the data was successfully transmitted back to the host computer running ATLAS. Thus, it is possible to detect data dropouts by looking for gaps in the SFID channels.

The GBU and ACRA subsystems generated 16-bit SFID values which range in value from 0 to 65535 and wrap around back to 0 after reaching the maximum value. The cRIO appears to generate a 32-bit SFID value, which would mean a maximum value of around 4.29 billion, but the SFID channel was never observed approaching the maximum and wrapping back to 0. When detecting dropouts, the algorithm must take into account the maximum SFID value for each subsystem and detect any data loss when the SFID wraps back to 0.

It was discovered after the field test that the cRIO’s SFID channel did not increment quite as expected. Instead, the same value would be repeated in groups and the groups would occur in patterns. The primary pattern was a group of three followed by a group of five which then repeats, such as:

2, 2, 2, 6, 6, 6, 6, 6, 10, 10, 10, 14, 14, 14, 14, 14, …

In this example the sequence should have been the numbers 1 through 16. As written above, the middle number in each group of three or group of five matches the true SFID. Numbers to the right or left of the middle of a group need to be incremented or decremented by their distance from the middle. It is not important to understand how this correction was applied to the cRIO’s SFID channel but rather that a correction needed to be made in post processing. It is not clear why the cRIO generated this pattern and in fact other patterns have been observed:

- 1, 3, 3, 3, 5, 7, 7, 7, 9, 10, 10, 10, … (a group of one, then three, repeating)
- 4 (seven times), 12 (nine times), 20 (seven times), …

For the most part, the cRIO did not have any data dropouts, in which case it was straightforward to correct for the patterns observed. However, when a dropout did occur it disrupted the pattern and made it difficult to automatically correct the SFID channel because it was impossible to know which one of the repeated numbers in a pattern group was the one that had been dropped. Therefore, when a disruption in the pattern was detected the SFID correction procedure was stopped and the rest of the data from that point on was ignored.

The GBU averaged about 13 dropouts per ten-minute file. The RBU averaged about 45 dropouts per ten-minute file. (A ten-minute file captured at 50 Hz contains 30,000 data frames.)

5. DATA POST PROCESSING

5.1 Scale and Offset

The scale and offset of a few data channels needed to be adjusted for various reasons outlined below. Table 4.1 lists the values of the offsets and multipliers.

- Channel 22, AZIMUTH_ANGLE, had an error in its channel configuration and needed to be multiplied by 2.
- Channel 32, LSS_SPEED, had an error in its channel configuration and needed to be divided by 10.
- Motor_Position channels (75, 77, 79, 81, 83, 85, 87, 89, 91) were output and recorded as a 0-10 volt signals which needed to be converted to motor shaft angle in degrees.
- Motor_Current channels (76, 78, 80, 82, 84, 86, 88, 90, 92) were output and recorded as a 0-10 volt signals which needed to be converted to current in amps.
- Athena_AnalogOut channels (93, 94, 95) were output as a 0-5 volt signals and recorded as a 0-10 volt signals which needed to be converted to commanded flap angle in degrees.
- Certain accelerometer channels needed to be swapped in specific data files (which were acquired prior to the time when the cable swap was corrected). Affected files include those acquired before 16-Feb-2012 and those acquired on 5-Apr-2012.
- DAQ_IMU_*_cRIO channels (147, 148, 149) needed to be converted from volts to acceleration (g). The multiplier and offsets were obtained from the IMU calibration report.
- Channels 140 through 146 needed to be converted from volts to microstrain. The multiplier and offsets were chosen to match the corresponding ACRA channels. Because the ACRA strain offsets were observed to drift, the offsets were chosen to match data from 24-Apr-2012 and 10-May-2012 which represent a major portion of the most useful operational data.

It is important to note that the offsets for all foil strain gage measurements were observed to drift over the duration of the field test. Thus the absolute magnitude of these strains is not directly available. However the relative changes in strain during a particular test day can be utilized because the drift can be assumed negligible over short time periods.

Table 5.1 Summary of post-processing offsets and multipliers applied according to Result = (Signal + Offset) x Multiplier

	Offset	Multiplier
LSS_SPEED	0	$\frac{1}{10}$
AZIMUTH_ANGLE	0	2
Motor_Position	-5	$-4 \times \left(\frac{10}{9.3}\right)$
Motor_Current	-5	$-\frac{1}{4}$
Athena_Analog	-2.5	$\frac{20}{2.5}$
DAQ_IMU_X_cRIO	-2.506	0.987
DAQ_IMU_Y_cRIO	-2.509	1.005
DAQ_IMU_Z_cRIO	-2.471	0.990
140 - B1_H1_Strain_0350_Z_HP	0*	91000
141 - B1_H1_Strain_0350_Z_LP	0.00062	91000
142 - B1_H1_Strain_2250_Z_HP	-0.20*	91000
143 - B1_H1_Strain_4500_Z_HP	-0.00380	91000
144 - B1_H1_Strain_6750_Z_HP	-0.00018	91000
145 - B1_H1_Strain_0350_Z_TE	-0.01*	91000
146 - B1_H1_Strain_0350_Z_LE	-0.00012	91000

* - corresponding ACRA channel was not working

5.2 Coordinate Systems and Transformations

The accelerometers were mounted to the internal blade structure using angled mounting blocks so that their axes of measurement would be roughly orthogonal with the desired blade coordinate axes. However, the tri-axial accelerometers were rotated in 90 degree increments to accommodate the ideal mounting orientation. In post-processing the channels were re-mapped to obtain the desired blade coordinates.

Figure 5.1 illustrates the orientation of each accelerometer with respect to the blade coordinate system and Table 5.2 provides the channel mapping into the blade coordinate system.

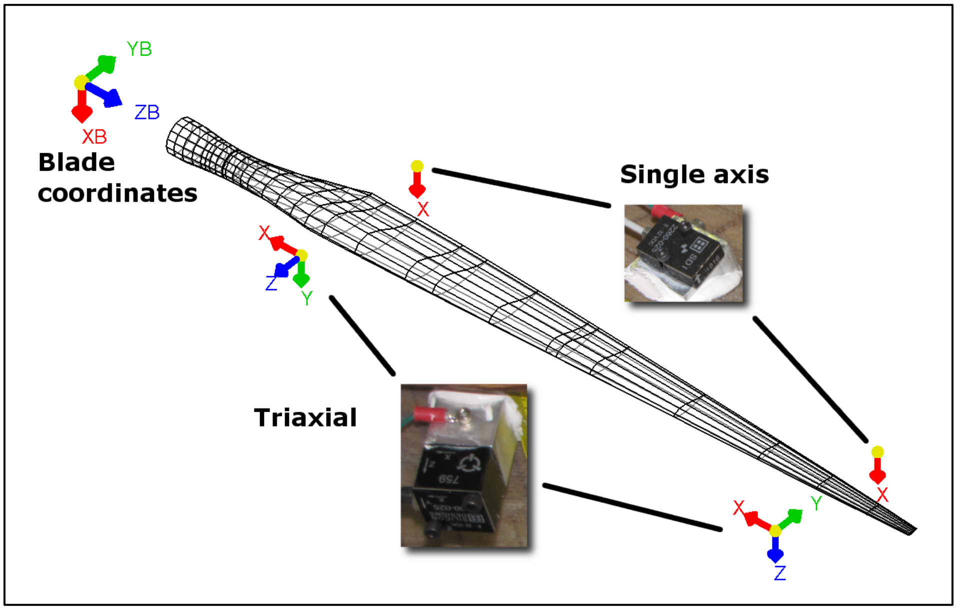

Figure 5.1 Orientation of accelerometers with respect to the blade coordinate system.

Table 5.2 Mapping of accelerometer channels to blade coordinate system

Original Accelerometer Channel	New Accelerometer Channel	Sign multiplier
Accel_2000_X_HP	Accel_2000_ZB_HP	-1
Accel_2000_Y_HP	Accel_2000_XB_HP	+1
Accel_2000_Z_HP	Accel_2000_YB_HP	-1
Accel_2000_X_TE	Accel_2000_XB_TE	+1
Accel_8000_X_HP	Accel_8000_ZB_HP	-1
Accel_8000_Y_HP	Accel_8000_YB_HP	+1
Accel_8000_Z_HP	Accel_8000_XB_HP	+1
Accel_8000_X_TE	Accel_8000_XB_TE	+1

The nacelle IMU coordinate system has Y pointed downwind, Z pointed towards the ground, and X completing a right-handed coordinate system.

The rotor IMU coordinate system has Z pointing along the rotor axis or roughly upwind with 5 degrees of rotor tilt. The X and Y axes are in the rotor plane. The phase angle difference between the AZIMUTH_ANGLE channel and the DAQ_IMU_X channel was found in post processing by comparing the sine of the azimuth angle to the sinusoidal signal output by the rotor IMU x-axis measurement of acceleration due to gravity. Adding 65.3 degrees to the azimuth angle brought the two sinusoids into phase.

5.3 Time-Synchronized Resampling

The first step in resampling the data was to verify the sample rate of each subsystem by using the procedure described in Section 4.3. Briefly, the procedure was to fit a straight line to the stair-step line of GPS time plotted against sample number. The slope of the line was the sample period. The residuals, or the difference between the straight-line fit and the actual points, are shown in Figure 5.2 for a single ten-minute file. The plot of residuals revealed how well the straight line fit accounted for the structure in the data, and in most cases the residuals stayed within the ±0.5 second band which indicated that the 1-second duration of the GPS time updates had remained consistent. The “sawtooth” appearance of the GBU and ACRA residuals occurred because their sample periods were steady but not wholly divisible into one second and therefore the sample positions slowly slide relative to the 1-second interval. The less regular appearance of the cRIO residuals indicates that its sample rate was somewhat irregular, although still quite accurate.

This procedure was repeated for all ten-minute data files and the averages (excluding obvious outliers) are given in Table 5.3 along with the values predicted by ATLAS based on the hardware configuration and also the values that were used for resampling. The sample period chosen for the cRIO does not exactly match the GPS average because better resampling alignment was possible using the adjusted sample period.

Table 5.3 Subsystem sample periods in seconds.

	GBU	ACRA	cRIO
GPS-fit average	0.019991996	0.019971008	0.020000411
Predicted by ATLAS	0.019992	0.019971	0.020008
Value for resampling	0.01999200	0.01997100	0.02000046

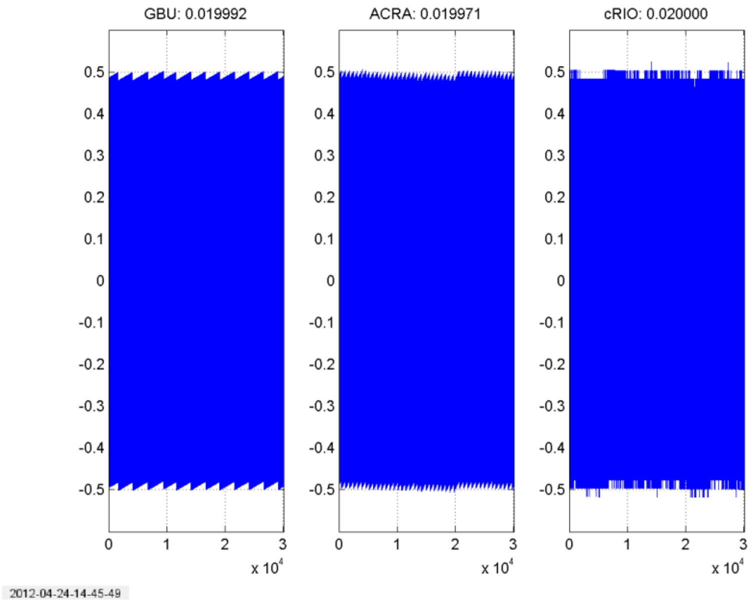

Figure 5.2 Pattern of residuals about straight-line fit to GPS time.

The next steps in resampling and aligning the data were to up-sample from the approximate 50 Hz sample rate to a common rate of 5000 Hz and then determine the amount of sample offset between the alignment channels (see Section 4.2). Resampling to this higher frequency improved the alignment resolution from 20 milliseconds to 0.2 milliseconds.

Resampling was accomplished with a frequency-domain technique described by Stearns and Hush [56] which is also equivalent to the “resample” command in the MATLAB© Signal Processing Toolbox™ [57]. Being a frequency-domain technique, care was taken to ensure the Nyquist-Shannon sampling theorem was satisfied. All channels, except the azimuth signal (22), were acquired with an input low-pass filter of at least one-half the sample rate and in most cases one-fourth the sample rate. One caveat was the data dropouts which needed to be filled in. Although there are techniques for resampling irregular-spaced samples, numerical issues were encountered when trying to apply them. So spline interpolation was used instead for data dropouts with the assumption that the sampling theorem would still be satisfied during resampling.

The azimuth signal was unique because it regularly “jumped” from 360 degrees to 0 degrees which looked like a high frequency event. This was why a low-pass filter was not used on the azimuth signal. Physically, however, the azimuth signal cannot have significant high frequency content due to the rotor inertia, and so it was assumed that the sampling theorem was satisfied. Resampling of the azimuth signal involved the following steps:

1. Transform the discontinuous signal into two continuous signals using sine and cosine functions
2. De-spike the two transformed signals (the azimuth sensor did not always produce clean output)
3. Resample both signals

4. Recombine the two signals using the inverse tangent function

The amount of time delay required for alignment was determined by calculating the cross-correlation between alignment channels. Figure 5.3 diagrams the relationship of clock delays between subsystems and channel offsets within subsystems.

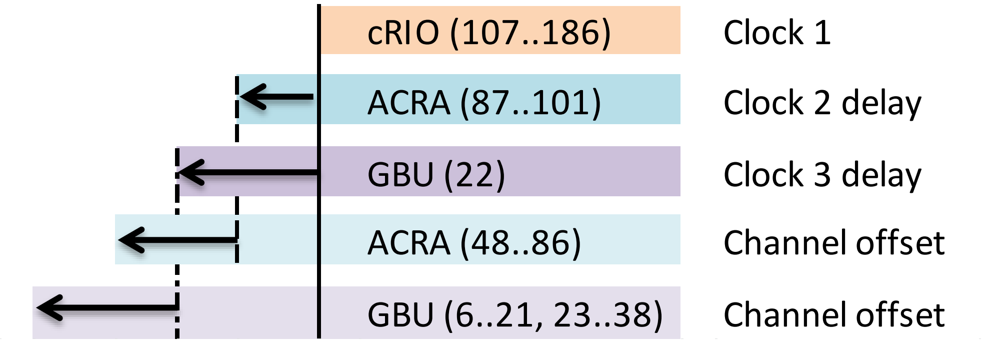

Figure 5.3 Schematic of subsystem clock delays and channel offsets

The beginning of the cRIO's data stream always occurred later in time than those of the ACRA and the GBU data streams. The result was that beginning segments of ACRA and GBU channels had to be discarded so that all of the first samples were in alignment. Because the cRIO's first data frame became the first one in the resampled data, it was convenient to reference the clock delays to Clock 1 (the cRIO).

The clock delays between subsystems changed every time a new data acquisition session began. These variable delays likely resulted from network communication lags and differences in system start-up time when ATLAS instructed each subsystem to begin acquiring data.

The channel offsets within each subsystem were constant and resulted from differences in input filter configuration or module function. These fixed channel offsets were verified with post-test measurements acquired with a common voltage signal routed to all sensor channels. Table 5.4 lists the measured offsets. Motor channels (75..92) were slightly different than the rest because extra hardware was required to obtain and convert these signals which produced offsets in addition to the inherent ACRA delays. The expected offsets for the motor channels are given but have not been directly verified.

The final step in resampling was to down-sample to 50 Hz by simple decimation (discarding data points).

Table 5.4 Channel offsets relative to subsystem clocks measured in number of samples at 5 kHz resampling

Channels	Clock ID	Channel offset (samples at 5 kHz)
22	3	0
6..21, 23..32, 35..38	3	5256
33..34	3	5275
48..74	2	3395
75, 81	2	3395 + 55
76, 82	2	3395 + 45
77, 83	2	3395 + 35
78, 84	2	3395 + 25
79, 85	2	3395 + 15
80, 86	2	3395 + 5
87	2	55
88	2	45
89	2	35
90	2	25
91	2	15
92	2	5
93..101	2	0

6. ON-GROUND CALIBRATION

ATA Engineering was contracted to assist with the blade modal test and analysis. The following sections are preliminary results of the modal characterization and model updating tasks. These results were calculated before the time synchronization issues were fully understood, but they should still be valid because the cRIO's signals were the focus of the modal analysis.

A subsequent update to these preliminary results was planned for the purpose of creating a well-tuned turbine model appropriate for closed-loop control design. However, with the project test window being cut short and the Bushland Test Site subsequently decommissioned, the final update was no longer a high priority.

The on-ground testing included impact test data while each of the blades was suspended using metal cables to mimic a free-free boundary condition as well as when the blade was cantilevered off of a fixed hub. Static pull testing in both the edge and flap directions was also performed when the blade was in the cantilevered configuration.

ATA Engineering's analysis utilized only the modal impact data acquired while the blade was in the free-free boundary condition for the initial modal characterization of the SMART blades and the model updating procedure. This subset of the data was selected because it was believed that assumption of the free-free boundary condition in the suspended configuration was more accurate than the assumption of the cantilever boundary condition when the blade was attached to the hub due to the residual rotational flexibility of the hub.

6.1 Preliminary Blade Modal Properties

To experimentally determine the modal properties of the SMART blades, each of the blades was excited using an instrumented modal impact hammer at nine different locations on each blade. The relatively small number of impact locations was due to the limited amount of time for testing and the fact that 60 seconds were needed to capture the response of the structure after each impact. Due to the sparse nature of the impact locations a simple beam model of the blade was used for displaying the mode shapes and is shown in Figure 6.1. At locations 21, 22, and 25 through 29 the blades were impacted in both the flap and edge directions. Rigid body completion was used to determine the Y-direction deformations of nodes 23 and 24. No axial deformations (in the Z-direction) were considered in this analysis.

A batch processing methodology was developed to ease future analyses of similar data sets. The data from each of the data files generated by ATLAS were unzipped and loaded into Matlab and the associated header files were parsed to obtain the pertinent information. These files were then concatenated so that a single set of time data was created for each test. Then the associated Excel modal test log was open and parsed using Matlab to determine the node number and direction of each impact on the blade.

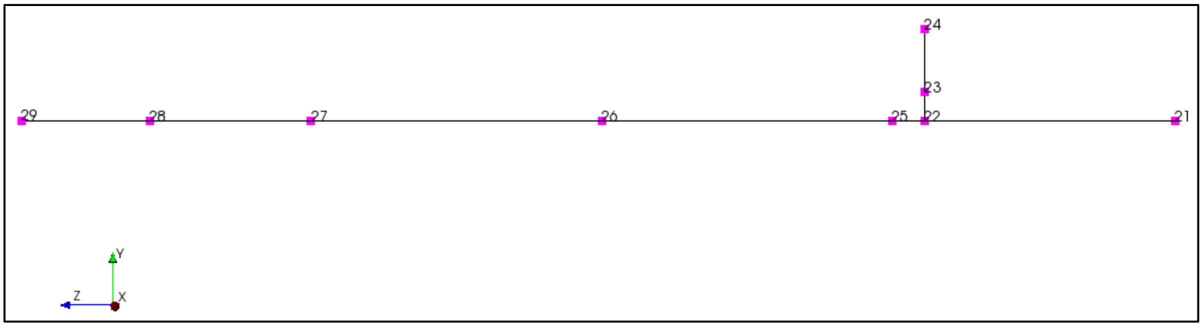

Figure 6.1 Simple beam element model used to display the experimental mode shapes.

The time histories were then converted into Frequency Response Functions (FRFs) using ATA's spFRF signal processing tool which calculated the average auto- and cross- spectral densities of the Impact Hammer and all eight response accelerometers for each of the impact locations. These auto- and cross-spectra were then used to estimate the systems FRFs using the H_1 estimator.

After the FRF matrix had been created using all 8 accelerometers and all 19 impact coordinates the systems natural frequencies and damping values were estimated using the alias-free polyreference algorithm. The alias-free polyreference technique, in ATA's AFPoly™ IMAT toolkit, employs a Laplace-domain, curve-fitting algorithm. Damping was estimated using the same polyreference FRF curve-fitting algorithm that was used to extract the resonant frequencies. The mode shapes were then calculated by refitting the FRFs using the extracted system poles and rigid body completion was used to estimate the deformation of the unmeasured degrees-of-freedom for visualization purposes.

Further investigation of the modal impact data revealed that rotation of the blades during testing caused a perturbation of the mode shapes and natural frequencies due to the varying stiffness of the boundary conditions. One way in which this is evident is through the shift in the resonant frequencies of the blade depending on the blade's orientation. For instance when the trailing edge of the Blade 3 was pointing upwards (as in Figure 5.1) the resonant frequency of the first flap bending mode was approximately 7.3 Hz and the second bending mode occurred at approximately 17.7 Hz. However, when Blade 3 was rotated so that its chord line was approximately horizontal these modes appeared to shift to approximately 7.5 and 20.3 Hz.

In an attempt to minimize the influence of this rotation on the extracted modal parameters, the poles of the system were extracted from the impacts and response measurements that were perpendicular to the direction of gravity (parallel to the weak axis of the supports). This means that the modal frequency and damping values were calculated using only the measurements from when the structure was closest to free-free in that direction for each mode. The calculated poles were then used to estimate the mode shapes using the impacts in both directions. However, because of the physical change in the system this means that the estimates of the mode shapes in the non-dominant direction of motion (edge-wise for flap bending modes and vice-versa) are likely much less accurate than the calculated mode shapes in the dominant direction of motion.

Therefore, ATA recommended that in future testing the metal cables be replaced with bungees and that at least one of the blades be impacted in both directions for both configurations. Metal cables were used in this test to avoid adding extra damping. An alternative approach may be to loop the blade using the metal cable and then connect these loops to the support truss through intermediate bungees. In this way the material in contact with the structure remains the same while the stiffness of the support system would be significantly reduced. If the boundary condition remains too stiff in the vertical direction it could also be modeled as grounded springs during the correlation process as long as impacts in both directions are obtained while the blade is in a single configuration.

Using the directional method described above to estimate the natural frequencies and damping values of all three of the blades, the values in Table 6.1 were calculated using the previously described Alias-Free Polyreference algorithm. The modal properties of the blades are relatively consistent with the standard deviation of the natural frequencies of the blades for the flexible modes all being less than 2.1% of the average natural frequency. In fact, other than the second flap bending edge bending mode, the standard deviation of the natural frequencies varied by less than 1% of the average for each mode.

Table 6.1 Free-free natural frequency and damping values for all three of the SMART blades. Five flexible modes were calculated in addition to three rigid body modes.

Mode	Blade 1		Blade 2		Blade 3		Average		Mode Shape
Number	Freq (Hz)	Damp (% Cr)	Freq (Hz)	Damp (% Cr)	Freq (Hz)	Damp (% Cr)	Freq (Hz)	Damp (% Cr)	Description
RB1	0.25	6.0	0.26	5.8	0.26	5.9	0.26	5.93	Rigid Body Horizontal Twist (about Y-Axis)
RB2	0.31	3.9	0.29	4.8	0.33	3.5	0.31	4.07	Rigid Body Vertical Twist (about X-Axis)
RB3	2.69	1.0	2.62	1.4	2.61	0.6	2.64	1.02	Rigid Body Longitudinal Twist (about Z-Axis)
1	7.28	0.5	7.19	0.5	7.21	0.6	7.23	0.53	First Flap Bending
2	15.91	1.1	15.63	1.0	15.74	1.2	15.76	1.12	First Edge Bending
3	17.92	1.0	17.57	0.9	17.73	1.0	17.74	0.96	Second Flap Bending
4	29.27	1.5	29.21	1.1	29.52	0.9	29.33	1.15	Third Flap Bending
5	36.68	1.5	35.93	1.7	37.44	0.4	36.68	1.22	Second Edge Bending

6.2 Preliminary Beam Model Updating

Initial beam model parameters were calculated from an ANSYS blade model using BPE. The mass densities per unit length that were calculated using BPE were left consistent but the mass densities were scaled so that the total mass of the blade was scaled to match the experimental average of the CX-100 blades. In order to account for the added mass of the lightning protection in the SMART blades a total of 5 kg was added evenly along the blade by increasing each of the mass densities accordingly. The planned final update to these analyses would have also included the change in mass distribution due to the addition of the flap modules.

For the correlation procedure only the edge- and flap-wise distributed stiffness values were modified. In order to update this model while maintaining realistic stiffness parameters constrained minimization was performed. Because both the distributed stiffness parameters of the beam were to be updated both the natural frequencies and the mode shapes of the model needed to be compared. Consequently, the optimization function was calculated using a weighted sum of the RMS of the differences in the natural frequencies and the RMS of one minus the modal assurance criteria calculated between the corresponding mode shape for the model and the experimental results (commonly referred to as the Cross-MAC). However, due to the difficulty in estimating the mode shapes in the non-dominant direction (edge-wise motion for flap dominant modes) mentioned above, the Cross-MAC was only calculated in the dominant direction of motion (only flap deflections were used for modes that were dominant in the flap direction).

Table 5.2 shows a comparison of the percent errors in the natural frequencies as well as the MAC values for each of the three different correlated models. As can be seen, a high degree of correlation was obtained for each of the three blades. The change in the stiffness values for each of the beam elements was then investigated and the changes in the flap-wise and edge-wise stiffness values along the length of the beam can be seen in Table 5.3 and Table 5.4 respectively. For both sets of stiffness values, by far the largest percent changes occurred near the tip of the blade. This was anticipated due to the changes in the SMART blade layup; however, these results would change somewhat if the flap module masses were fully accounted.

Table 6.2 Comparison of the free-free experimental results for each blade as well as the model correlated to each blade.

Mode	Uncorrelated	Blade 1 Results				Blade 2 Results				Blade 3 Results			
Number	Nat. Freq. (Hz)	Exp. (Hz)	Model (Hz)	% Err	MAC	Exp. (Hz)	Model (Hz)	% Err	MAC	Exp. (Hz)	Model (Hz)	% Err	MAC
1	7.08	7.28	7.28	0.0%	99.8%	7.19	7.19	0.0%	99.7%	7.21	7.22	-0.1%	99.7%
2	14.04	15.91	15.91	0.0%	98.7%	15.63	15.41	1.5%	97.7%	15.74	15.12	4.0%	97.9%
3	16.77	17.92	17.92	0.0%	99.8%	17.57	17.59	-0.1%	99.9%	17.73	17.76	-0.1%	99.7%
4	30.54	29.27	29.27	0.0%	99.7%	29.21	29.21	0.0%	99.8%	29.52	29.54	-0.1%	99.9%
5	33.82	36.68	36.68	0.0%	98.2%	35.93	35.76	0.5%	95.7%	37.44	37.81	-1.0%	96.7%

Table 6.3 Flapwise stiffness along the length of the blade (Bld Fract) calculated directly from BPE (Uncorrelated) and using each of the correlated models. The average stiffness values and the percent change between the average value and the initial value are also shown.

Flap-wise Stiffness (N-m^2)						
Bld Fract	Uncorrelated	Blade 1	Blade 2	Blade 3	Average	Ave % Change
1.4%	3.62E+07	3.62E+07	3.62E+07	3.62E+07	3.62E+07	0.01%
5.3%	1.16E+07	1.16E+07	1.16E+07	1.16E+07	1.16E+07	-0.03%
10.3%	3.99E+06	3.99E+06	3.98E+06	3.98E+06	3.98E+06	-0.04%
15.3%	3.48E+06	3.49E+06	3.48E+06	3.48E+06	3.48E+06	-0.04%
20.6%	2.92E+06	2.92E+06	2.91E+06	2.91E+06	2.92E+06	-0.12%
26.7%	2.19E+06	2.19E+06	2.19E+06	2.19E+06	2.19E+06	-0.09%
32.6%	1.52E+06	1.52E+06	1.52E+06	1.52E+06	1.52E+06	-0.08%
37.9%	1.06E+06	1.06E+06	1.06E+06	1.06E+06	1.06E+06	-0.10%
44.4%	6.82E+05	6.85E+05	6.82E+05	6.76E+05	6.81E+05	-0.15%
51.5%	4.19E+05	4.22E+05	4.18E+05	4.16E+05	4.19E+05	-0.03%
59.1%	2.40E+05	2.29E+05	2.22E+05	2.30E+05	2.27E+05	-5.60%
68.9%	1.07E+05	8.66E+04	8.30E+04	8.41E+04	8.46E+04	-20.85%
79.2%	3.51E+04	8.24E+04	1.00E+05	8.87E+04	9.05E+04	157.80%
87.5%	1.07E+04	1.60E+04	1.18E+04	1.22E+04	1.33E+04	24.62%
94.2%	2.25E+03	1.43E+03	1.58E+03	1.82E+03	1.61E+03	-28.38%
98.6%	4.17E+02	1.25E+03	1.24E+03	1.65E+02	8.85E+02	112.43%

Table 6.4 Edgewise stiffness along the length of the blade (Bld Fract) calculated directly from BPE (Uncorrelated) and using each of the correlated models. The average stiffness values and the percent change between the average value and the initial value are also shown.

Edge-wise Stiffness (N-m^2)						
Bld Fract	**Uncorrelated**	**Blade 1**	**Blade 2**	**Blade 3**	**Average**	**Ave % Change**
1.4%	4.19E+07	4.19E+07	4.19E+07	4.19E+07	4.19E+07	0.01%
5.3%	6.79E+06	6.79E+06	6.79E+06	6.79E+06	6.79E+06	0.04%
10.3%	1.96E+06	1.98E+06	1.97E+06	1.97E+06	1.97E+06	0.65%
15.3%	2.33E+06	2.36E+06	2.36E+06	2.34E+06	2.35E+06	0.82%
20.6%	3.56E+06	3.58E+06	3.57E+06	3.57E+06	3.57E+06	0.44%
26.7%	4.13E+06	4.16E+06	4.14E+06	4.13E+06	4.14E+06	0.35%
32.6%	3.52E+06	3.55E+06	3.54E+06	3.52E+06	3.54E+06	0.49%
37.9%	2.75E+06	2.81E+06	2.78E+06	2.76E+06	2.78E+06	1.08%
44.4%	2.04E+06	2.14E+06	2.09E+06	2.05E+06	2.09E+06	2.78%
51.5%	1.41E+06	1.54E+06	1.48E+06	1.42E+06	1.48E+06	5.17%
59.1%	9.05E+05	1.16E+06	1.03E+06	9.44E+05	1.04E+06	15.40%
68.9%	4.78E+05	9.34E+05	7.72E+05	6.41E+05	7.82E+05	63.64%
79.2%	2.06E+05	6.19E+05	6.19E+05	5.32E+05	5.90E+05	185.91%
87.5%	8.54E+04	7.02E+04	6.29E+04	1.82E+05	1.05E+05	22.85%
94.2%	3.02E+04	9.96E+03	9.96E+03	9.96E+03	9.96E+03	-67.00%
98.6%	1.11E+04	3.67E+03	3.67E+03	3.67E+03	3.67E+03	-66.99%

The average stiffness values in both the flap and edge direction were then calculated using all three models. The natural frequencies for this average model compared closely to the experimental average natural frequency across the three SMART blades as can be seen in Table 5.5 as the largest percent error in the natural frequencies was less than 2.5%.

Table 6.5 Average free-free experimental natural frequencies and the natural frequencies calculated from a beam model with the average stiffness values from each of the correlated models.

Mode Number	Average Nat. Freq. (Hz)	Ave Model Nat. Freq. (Hz)	Percent Error (%)
1	7.23	7.24	-0.14%
2	15.76	15.56	1.27%
3	17.74	17.84	-0.58%
4	29.33	29.47	-0.47%
5	36.68	37.58	-2.45%

6.3 Blade Strain Calibrations

Static pull testing in both the edge and flap directions was performed when the blade was in the cantilevered configuration. The blade root was bolted to a calibration fixture with the blade leading edge down and cantilevered parallel to the ground. The calibration fixture itself was a Micon 65/13 hub which had been attached to a support structure that also acted as a pull frame. A strain gage shunt calibration was performed first to zero the completion bridges and record the baseline strain values. The blade was then loaded in the both the edgewise and flapwise directions in six load steps up to 300 pounds-force. Flapwise loading was applied just inboard of the active control modules at 7 m span and edgewise loading was applied at 7.2 m span. Displacement measurements along the blade were obtained from a laser displacement transducer and string displacement potentiometers. Figure 6.2 is a photo of the edgewise blade pull. Table 6.6 contains the resulting strain calibration slopes and intercepts.

Table 6.6 Blade strain calibration. Measurement units for slope and intercept are (microstrain / lbf) and (microstrain), respectively.

	Flap Pull		Edge Pull	
	slope	intercept	slope	intercept
B1_H1_Strain_0350_Z_HP	0.0808	2.5114	-0.0122	-0.8714
B1_H1_Strain_0350_Z_LP	-0.0585	-1.9117	-0.0135	-1.1559
B1_H1_Strain_2250_Z_LP	-0.3285	-15.025	0.1358	-5.2972
B1_H1_Strain_4500_Z_LP	-0.6236	-23.779	0.1701	-4.4313
B1_H1_Strain_6750_Z_LP	-0.1784	-5.9871	0.0537	1.639
B1_H1_Strain_0350_Z_TE	-0.0043	4.5315	-0.1115	2.3311
B1_H1_Strain_0350_Z_LE	-0.0244	-9.5567	0.1409	-6.8395
B2_H2_Strain_0350_Z_HP	0.0678	2.1348	-0.0163	0.4519
B2_H2_Strain_0350_Z_LP	-0.0630	-1.9036	-0.0173	-1.7284
B2_H2_Strain_2250_Z_LP	-0.2967	-5.4967	0.1465	2.4077
B2_H2_Strain_4500_Z_LP	-0.5870	-15.541	0.1914	0.5457
B2_H2_Strain_6750_Z_LP	-0.1847	-9.3699	0.0683	-5.2529
B2_H2_Strain_0350_Z_TE				
B2_H2_Strain_0350_Z_LE	-0.0081	-6.7704	0.0738	-6.0823
B3_H3_Strain_0350_Z_HP	0.0532	-0.1968	-0.0102	-0.8004
B3_H3_Strain_0350_Z_LP	-0.0708	3.3771	-0.0084	-1.0359
B3_H3_Strain_2250_Z_LP	-0.3145	-29.356	0.171	-15.489
B3_H3_Strain_4500_Z_LP	-0.6658	-36.96	0.2568	-13.8
B3_H3_Strain_6750_Z_LP	-0.1794	-7.7114	0.1034	-1.1667
B3_H3_Strain_0350_Z_TE				
B3_H3_Strain_0350_Z_LE	0.0049	4.2217	0.0926	6.42

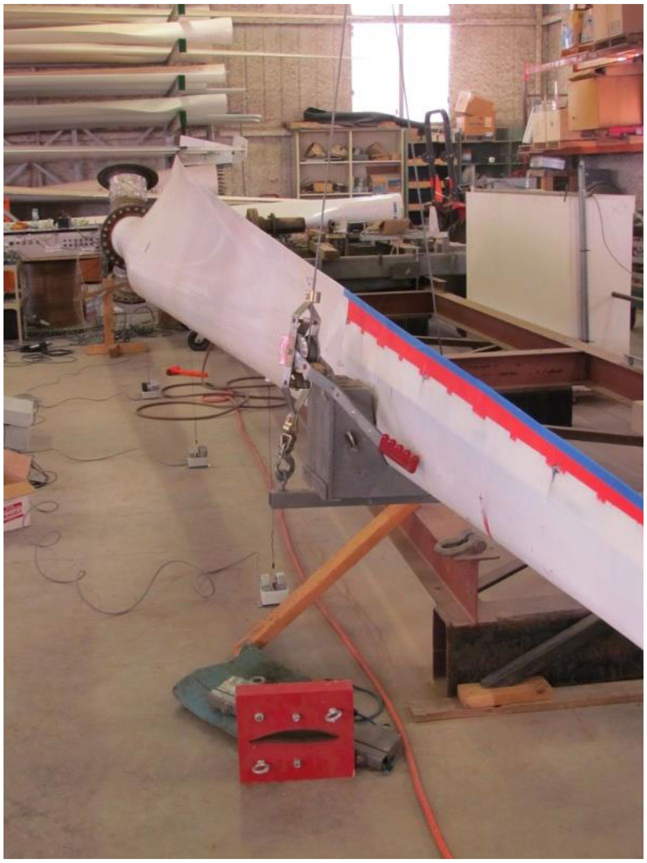

Figure 6.2 Edgewise blade pull on calibration fixture.

7. BLADE SURFACE GEOMETRY

The reduction in power output of the SMART rotor compared to a previous CX-100 field test (see Section 3.5) prompted an investigation into possible causes. One possibility was a difference in blade surface geometry. When the SMART rotor was built, the flap modules were designed and manufactured in parallel with the blades themselves. As a result, the flap modules, which were based on the geometry of an existing CX-100 blade tip, did not exactly match the geometry of the SMART blades. The mismatch was smoothed over with a flexible filler material.

To acquire a scan of the entire surface geometry, Creaform [58] was contracted to use one of their handheld optical scanning systems. Creaform chose to utilize their “MetraSCAN 3D” system, which is a combination of a handheld optical scanner and a stereo camera that locates the scanner in three-dimensional space. Figure 7.1 shows the scanning system and one SMART blade with optical targets scattered along the surface. Figure 7.2 is the resulting “point cloud” for one blade.

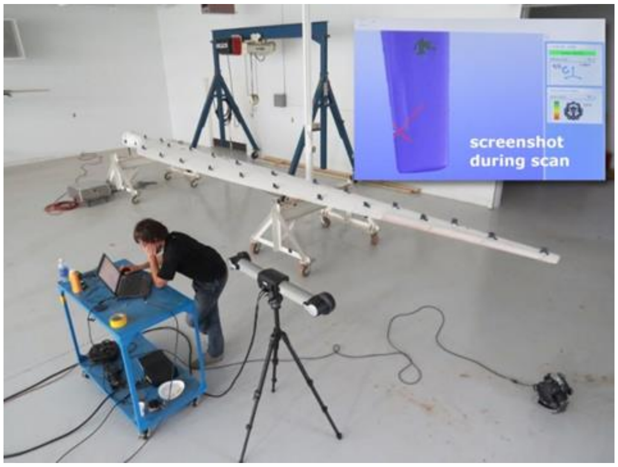

Figure 7.1 Creaform used their handheld optical scanning system to scan each blade.

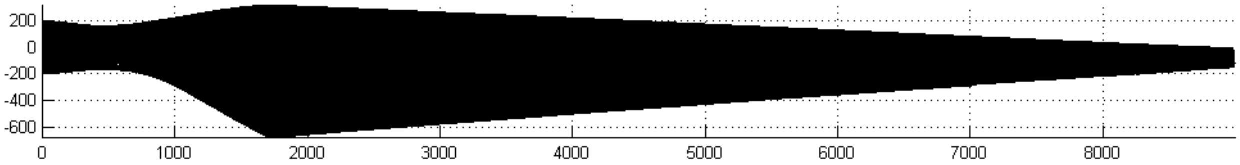

Figure 7.2 The entire surface of each blade was scanned, resulting in a high density “point cloud”.

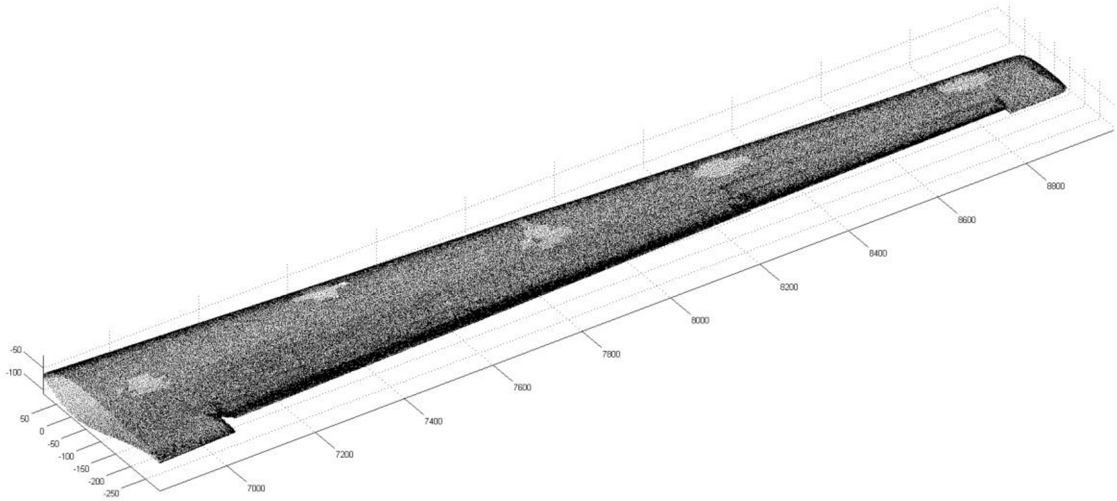

Figure 7.3 Detail of a SMART blade tip with flaps positioned at -20 degrees.

Figure 7.3 shows some of the detail captured at the tip of one SMART blade with the flaps positioned at -20 degrees. The five patches or voids are locations where an optical target was attached. The high density of points captured many of the surface geometry details that could perturb the air flow.

The entire blade surface was scanned so that the chord and twist distributions could be found and the exact location of any cross section would be known relative to the root. In addition to scans of the three SMART blades, a standard CX-100 blade was scanned.

Figure 7.4 compares the chord distributions of SMART Blade #2, the sample CX-100 blade, and the available CX-100 design information. The chord distributions of the two scans matched very well. The design chord distribution was off in the root transition region and the last half meter of the tip, which was expected because these areas of the blade mold were constructed “free-form” by hand and not measured until now.

Figure 7.5 compares the twist distributions of SMART Blade #2, the sample CX-100 blade, and the available CX-100 design information. The twist offsets of the two scans were adjusted to align their overall distributions with the design data. Also note that the measured twist distributions are somewhat noisy because identifying the chord line of a measured airfoil has some error involved which is amplified when calculating the chord line angle. However, it appears the sample CX-100 blade aligns well with the design data but the SMART blade has a deviation in twist starting just outboard of 6 meter span which results in on offset of -1.4 degrees at the tip.

This small change in twist distribution would tend to decrease power output but analysis predicted that the effect was relatively small and occurred mostly at higher wind speeds as the blade began to stall. The more significant geometry changes appear to be those which occurred locally on the airfoil cross section shapes.

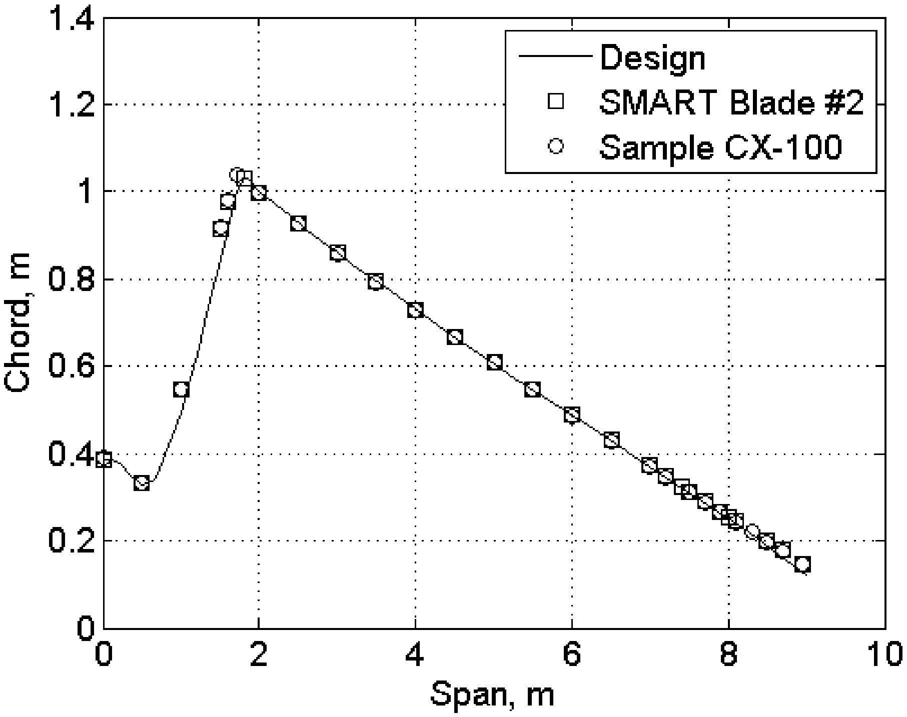

Figure 7.4 Chord distributions of SMART Blade #2, a CX-100 blade, and the available CX-100 design information.

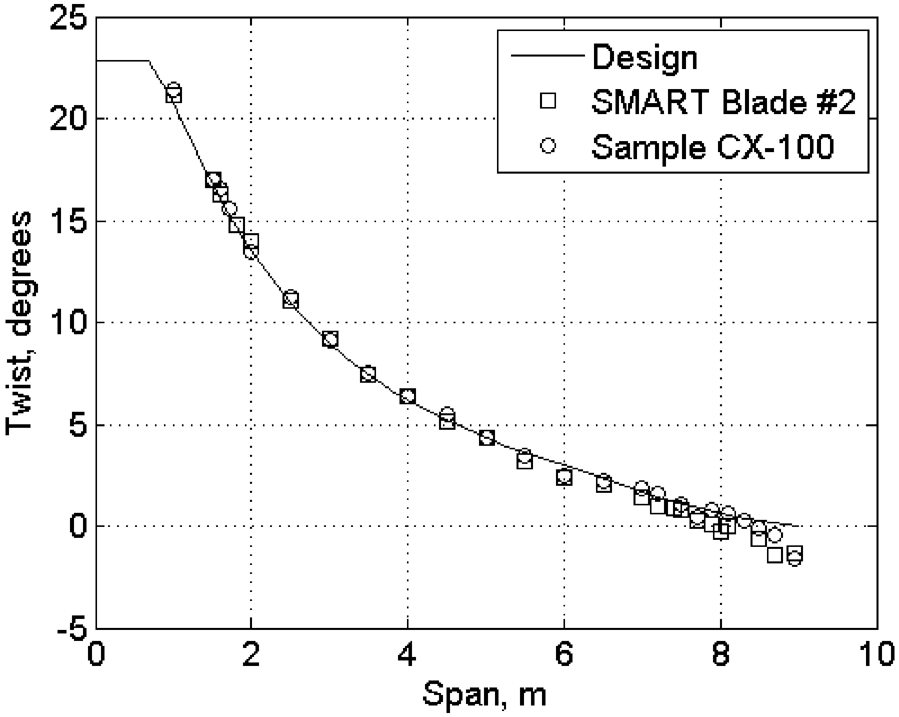

Figure 7.5 Twist distributions of SMART Blade #2, a CX-100 blade, and the available CX-100 design information.

Although all of the blades were manufactured from the same mold, comparison of SMART Blade #2 and the sample CX-100 blade reveal that the geometry matched almost exactly at some cross sections but had significant variation at others. Figures 7.6 through 7.9 exemplify the observed similarities and differences. Figures 7.8 and 7.9 illustrate how the geometry mismatch was corrected when the flap modules were interfaced to the blades. Note that the modules were thicker than the sample CX-100 blade, which indicates the blade tip on which the modules were based was also different from the CX-100 shown here. A strip of precurved mylar plastic was applied to the low-pressure surface of the blades along the flap hinge line. The plastic was bulged outward during the blade scans but should have lain down somewhat during turbine operation.

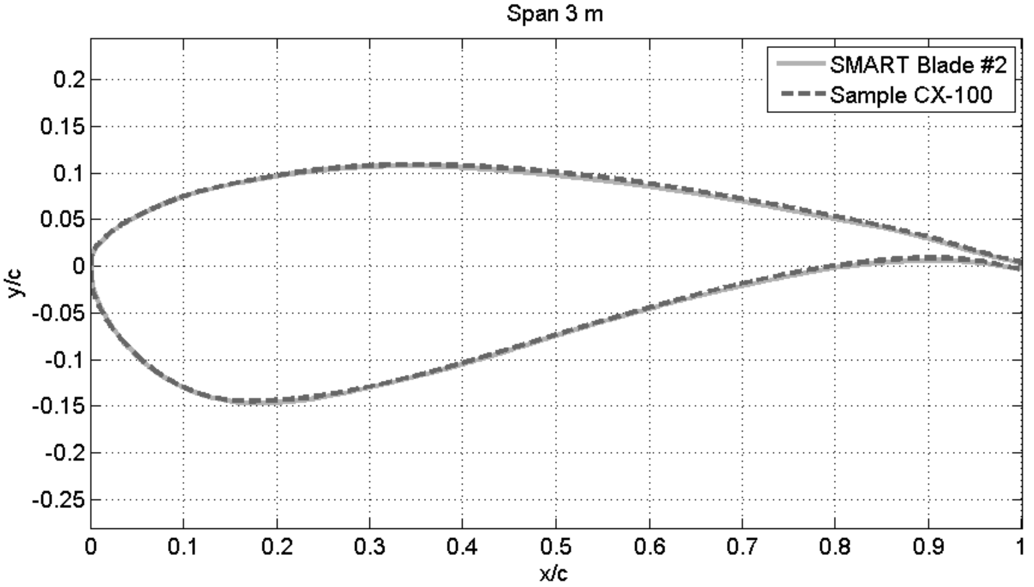

Figure 7.6 Cross sections at 3 meter span align almost perfectly.

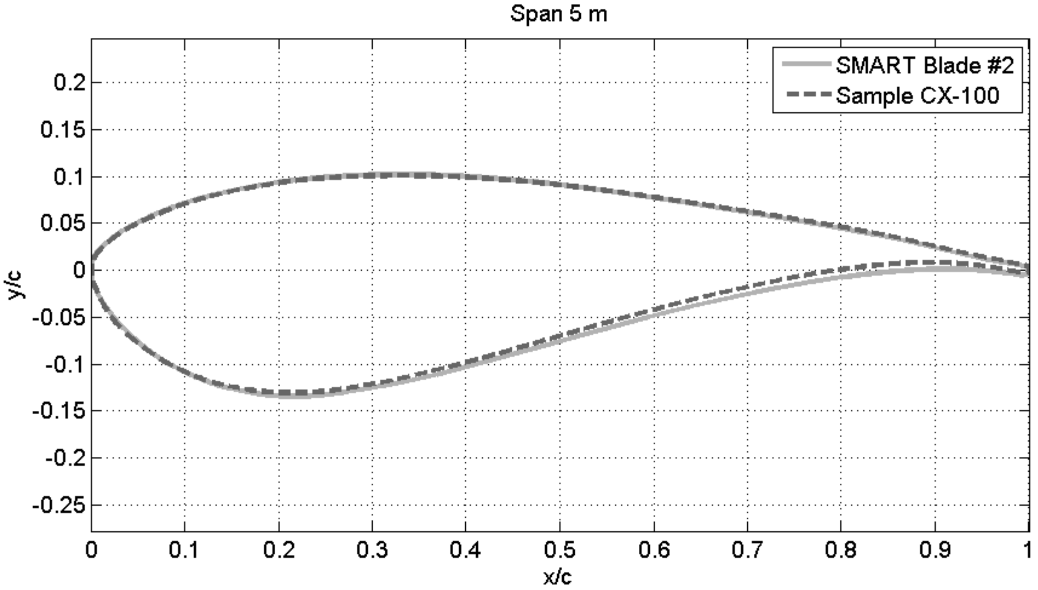

Figure 7.7 Cross sections at 5 meter span show variation in thickness.

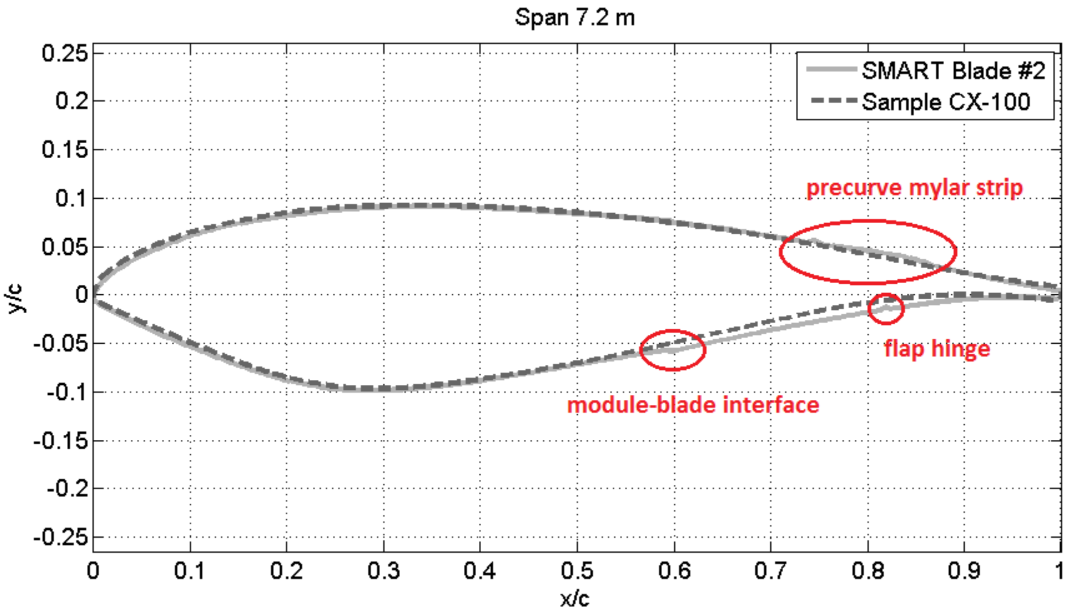

Figure 7.8 Cross sections at 7.2 meter span annotated with SMART blade alterations.

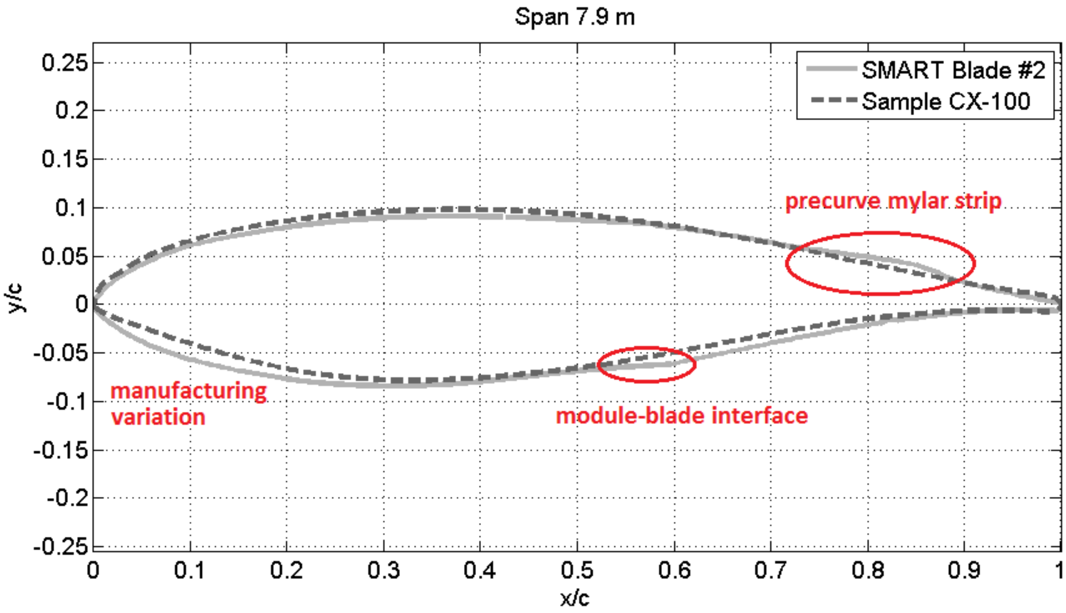

Figure 7.9 Cross sections at 7.9 meter span with variations annotated.

These cross section variations were likely contributors to the reduced power performance. The variations also highlight the difficulty of integrating additional hardware into a manufacturing process which can produce significant blade-to-blade variation.

8. REFERENCES

1. U.S. Department of Energy. “Report on the First Quadrennial Technology Review,” DOE/S-0001, Washington, DC, September 2011.

2. U.S. Department of Energy. “20% Wind Energy by 2030,” DOE/GO102008-2567, Washington, DC, July 2008.

3. T.K. Barlas and G.A.M. van Kuik. “Review of state of the art in smart rotor control research for wind turbines,” Progress in Aerospace Science (2009), doi:10.1016/j.paerosci.2009.08.002

4. J-W van Wingerden, A.W. Hulskapp, T. Barlas, B. Marrant, G.A.M. van Kuik, D-P Molenaar, and M. Verhaegen, “On the Proof of Concept of a ‘Smart’ Wind Turbine Rotor Blade for Load Alleviation”, Wind Energy, 2008; 11:265-80.

5. T. Barlas, J-W van Wingerden, A. Hulskamp, and G. van Kuik, “Closed-loop Control Wind Tunnel Tests on an Adaptive Wind Turbine Blade for Load Reduction,” Proceedings of the 46th AIAA/ASME, Reno, NV, USA, 2008.

6. N. Troldborg, “Computational study of the Risø B1-18 airfoil with a hinged flap providing variable trailing edge geometry.” Wind Engineering 2005, 29:89-113.

7. T. Buhl, M. Gaunaa, and C. Bak, “Load reduction potential using airfoils with variable trailing edge geometry,” Proceedings of the 43th AIAA/ASME, Reno, NV, USA, 2005.

8. T. Buhl, M. Gaunaa, and C. Bak, “Potential load reduction using airfoils with variable trailing edge geometry.” Solar Energy Engineering 2005, 127:503-16.

9. P. B. Andersen, M. Gaunaa, C. Bak, and T. Buhl, “Load alleviation on wind turbine blades using variable airfoil geometry,” Proceedings of the EWEC 2006, Athens, Greece.

10. P. B. Andersen, M. Gaunaa, C. Bak, and T. Buhl, “Wind tunnel test on wind turbine airfoil with adaptive trailing edge geometry,” Proceedings of the 45th AIAA/ASME, Reno, NV, USA, 2007.

11. T. Buhl, “Stability Limits for a Full Wind Turbine Equipped with Trailing Edge Systems,” European Wind Energy Conference, Marseille, France, 16-19 March, 2009.

12. P.B. Anderson, “Load Reduction Using Pressure Difference on Airfoil for Control of Trailing Edge Flaps,” European Wind Energy Conference, Marseille, France, 16-19 March, 2009.

13. D.G. Wilson, D.E. Berg, M.F. Barone, J.C. Berg, B.R. Resor, and D.W. Lobitz, “Active Aerodynamic Blade Control Design for Load Reduction on Large Wind Turbines,” European Wind Energy Conference, Marseille, France, 26-19 March, 2009.

14. D.E. Berg, D.G. Wilson, M.F. Barone, J.C. Berg, B.R. Resor, J.A. Paquette, and J.R. Zayas, "The Impact of Active Aerodynamic Load Control on Fatigue and Energy Capture at Low Wind Speed Sites," European Wind Energy Conference, Marseille, France, 16-19 March, 2009.

15. D.E. Berg, D.G. Wilson, B.R. Resor, M.F. Barone, J.C. Berg, S. Kota, and G. Ervin, "Active Aerodynamic Blade Load Control Impacts on Utility-Scale Wind Turbines," WINDPOWER 2009, Chicago, Illinois, 5-7 May, 2009.

16. D.G. Wilson, D.E. Berg, B.R. Resor, M.F. Barone, and J.C. Berg, "Combined Individual Pitch Control and Active Aerodynamic Load Controller Investigation for the 5MW UpWind Turbine", WINDPOWER 2009, Chicago, Illinois, 5-7 May, 2009.

17. B. Resor, D. Wilson, D. Berg, J. Berg, T. Barlas, and G. van Kuik, "The Impact of Higher Fidelity Models on Active Aerodynamic Load Control Fatigue Damage Reduction," Proceedings of the 48th AIAA Aerospace Sciences Meeting, Orlando, FL, January 4-7, 2010.

18. D.G. Wilson, B.R. Resor, D.E. Berg, T.K. Barlas, and G.A.M. van Kuik, "Active Aerodynamic Blade Distributed Flap Control Design Procedure for Load Reduction on the UpWind 5MW Wind Turbine," Proceedings of the 48th AIAA Aerospace Sciences Meeting, Orlando, FL, January 4-7, 2010.

19. D.E. Berg, D. Wilson, B. Resor, J. Berg, T. Barlas, A. Crowther, and C. Halse, "System ID Modern Control Algorithms for Active Aerodynamic Load Control and Impact on Gearbox Loading," The Science of Making Torque from Wind, 2010.

20. J. Berg, B. Resor, J. Paquette, and J. White, "SMART Wind Turbine Rotor: Design and Field Test." SAND2014-0681, Sandia National Laboratories, Albuquerque, NM.

21. D. Castaignet, J.J. Wedel-Heinen, T. Kim, T. Buhl, and N.K. Poulsen, "Results from the first full scale wind turbine equipped with trailing edge flaps." (AIAA 2010-4407, Proceedings of the 28th AIAA Applied Aerodynamics Conference, Chicago, Illinois, 28 June – 1 July 2010)

22. Damien Castaignet, Thanasis Barlas, Thomas Buhl, Niels K. Poulsen, Jens Jakob Wedel-Heinen, Niels A. Olesen, Christian Bak, and Taeseong Kim, "Full-scale test of trailing edge flaps on a Vestas V27 wind turbine: active load reduction and system identification." (Journal of Wind Energy, 2013, DOI: 10.1002/we.1589)

23. J. G. Leishman. "Challenges in modelling the unsteady aerodynamics of wind turbines." *Wind Energy*, 5:85–132, 2002.

24. L. J. Vermeer, J. N. Sørensen, and A. Crespo. "Wind turbine wake aerodynamics." *Progress in Aerospace Sciences*, pages 467–510, 2003.

25. M. Lackner and G. van Kuik. "A comparison of smart rotor control approaches using trailing edge flaps and individual pitch control." AIAA Paper 2009-685, 2009.

26. H. Snel. "Survey of induction dynamics modelling within BEM-like codes: Dynamic inflow and yawed flow modelling revisited." AIAA Paper 2001-0027, 2001.

27. M. Gaunaa. "Unsteady 2D potential-flow forces on a thin variable geometry airfoil undergoing arbitrary motion." Technical Report Risø-R-1478, Risø-DTU, 2004.

28. M. P. Kinzel, M. D. Maughmer, and G. A. Lesieutre. "Miniature trailing-edge effectors for rotorcraft performance enhancement." *J. Am. Helicopter Soc.*, 52(2):146–158, 2007.

29. P. B. Andersen, M. Gaunaa, C. Bak, and M. H. Hansen. "Implementing a dynamic stall model for airfoils with deformable trailing edges." AIAA Paper 2008-1328, 2008.

30. S. Schreck and M. Robinson. "Boundary layer state and flow field structure underlying rotational augmentation of blade aerodynamic response." *J. Solar Energy Engineering – Transactions of the ASME*, 125(4):448–456, 2003.

31. H. Glauert. Airplane propellers. In W. F. Durand, editor, *Aerodynamic Theory*. Julius Springer, Berlin, Germany, 1935.

32. D. M. Pitt and D. A. Peters. "Theoretical prediction of dynamic-inflow derivatives." *Vertica*, 5(1):21–34, 1981.

33. D. A. Peters, D. D. Boyd, and C. J. He. "Finite-state induced-flow model for rotors in hover and forward flight." *J. American Helicopter Soc.*, 34(4):5–17, 1989.

34. C. J. He. *Development and application of a generalized dynamic wake theory for lifting rotors.* PhD thesis, Georgia Institute of Technology, July 1989.

35. P. J. Moriarty and A. C. Hansen. AeroDyn Theory Manual. Technical Report NREL/EL-500-36881, National Renewable Energy Laboratory, 2005.

36. M. Joglekar and R. Loewy. "An actuator-disc analysis of helicopter wake geometry and the corresponding blade response." USAAVLABS Technical Report 69-66, 1970.

37. J. G. Leishman, M. J. Bhagwat, and A. Bagai. "Free-vortex filament methods for the analysis of helicopter rotor wakes." *J. of Aircraft*, 39(5):759–775, 2002.

38. S. G. Voutsinas, V. A. Riziotis, and P. Chaviaropoulos. "Non-linear aerodynamics and fatigue loading on wind turbines operating at extreme sites." AIAA Paper 97-0935, 1997.

39. S. Gupta and J. G. Leishman. "Comparison of momentum and vortex methods for the aerodynamic analysis of wind turbines." AIAA Paper 2005-594, 2005.

40. S. Gupta and J. G. Leishman. "Validation of a free-vortex wake model for wind turbines in yawed flow." AIAA Paper 2006-389, 2006.

41. S. Gupta and J. G. Leishman. "Performance predictions of the NREL Phase VI combined experiment rotor using a free-vortex wake model." AIAA Paper 2006-390, 2006.

42. T. Sant, G. van Kuik, and G. van Bussel. “Estimating the unsteady angle of attack from blade pressure measurements on the NREL Phase VI rotor in yaw using a free-wake vortex model.” AIAA Paper 2006-393, 2006.

43. S. Cline and C. Crawford. “Comparison of potential flow wake models for horizontal-axis wind turbine rotors.” AIAA Paper 2010-463, 2010.

44. G. Xu and L. N. Sankar. “Computational study of horizontal axis wind turbines.” AIAA Paper 99-0042, 1999.

45. C. P. van Dam, J. C. Vander Kam, and J. K. Paris. “Design-oriented high-lift methodology for general aviation and civil transport aircraft.” *J. of Aircraft*, 38(6):1076–1084, 2001.

46. L. Greengard and V. Rohklin. “A fast algorithm for particle simulations.” *J. Comp. Phys.*, 73:457–487, 1987.

47. P. S. Bernard. “Vortex filament simulation of the turbulent coflowing jet.” *Phys. Fluids*, 21, 2009.

48. Chopra, A.K., Dynamics of Structures, 2nd Edition, Prentice Hall, Upper Saddle River, New Jersey, 2001

49. XFOIL 6.97 by Mark Drela and Harold Youngren. MIT Aero & Astro / Aerocraft, Inc. (http://web.mit.edu/drela/Public/web/xfoil/)

50. ACRA Control Ltd., http://www.acracontrol.com
(Landscape House, Landscape Road, Dublin 14, Ireland)
Since 2011, part of Curtiss-Wright Corporation, http://www.cwc-ae.com/acra-control

51. National Instruments Corporation, http://www.ni.com
(11500 N Mopac Expwy, Austin, TX 78759-3504 USA)

52. Micron Optics, Inc., http://www.micronoptics.com
(1852 Century Place NE, Atlanta, GA 30345 USA)

53. J.R. Zayas, P.L. Jones, and J. Ortiz-Moyet, *Accurate GPS Time-Linked Data Acquisition System (ATLAS II) User’s Manual*. SAND2004-0481, Sandia National Laboratories, Albuquerque, NM, USA.

54. Science & Engineering Applications Datentecknik GmbH (S.E.A.), http://www.sea-gmbh.com

55. L.D. Nelson, L. Manuel, H.J. Sutherland, P.S. Veers, “Statistical Analysis of Inflow and Structural Response Data from the LIST Program,” Proceedings of the 2003 ASME Wind Energy Symposium, pp. 270-282

56. S.D. Stearns and D.R. Hush, Digital Signal Processing with Examples in MATLAB. (Second Edition, CRC Press, Boca Raton, FL, 2011)

57. The MathWorks, Inc., http://www.mathworks.com
(3 Apple Hill Drive, Natick, Massachusetts 01760 USA)

58. Creaform Inc., http://www.creaform3d.com
(Quebec City Area, 5825 rue St-Georges, Levis, Quebec, G6V 4L2)

APPENDIX A: ATLAS CONFIGURATION SETTINGS

CHASSIS: GBU FRAME SAMPLE RATE (EXPECTED): 50.02 Hz

MODULE: gbu_J2_enc (KAM/ENC/004)

Index	Tx	Signal Name	Bits	Value
0	yes	gbu_J2_enc_12345	16	12345
1..7	no	<empty>		

MODULE: gbu_J3_empty (EMPTY/SPARE)

MODULE: gbu_J4_analog (KAM/ADC/005)

Index	Tx	Signal Name	Bits	Max	Min	Filter
0	no	gbu_J4_analog_0	16	10.00	-10.00	Fs/4
1	no	gbu_J4_analog_1	16	10.00	-10.00	Fs/4
2	no	gbu_J4_analog_2	16	10.00	-10.00	Fs/4
3	no	db	16	10.00	0.00	Fs/4
4	yes	BAHHATIU	16	10.00	-10.00	Fs/4
5	yes	BAHHATIV	16	10.00	-10.00	Fs/4
6	yes	BAHHATIW	16	10.00	-10.00	Fs/4
7	yes	BAHHATIT	16	10.00	-10.00	Fs/4

MODULE: gbu_J5_analog (KAM/ADC/005)

Index	Tx	Signal Name	Bits	Max	Min	Filter
0	yes	BAHHC	16	5.00	0.00	Fs/4
1	yes	BAHHV	16	5.00	0.00	Fs/4
2	yes	BATP	16	5.00	0.00	Fs/4
3	yes	BADTP	16	5.00	0.00	Fs/4
4	yes	OHHC	16	5.00	0.00	Fs/4
5	yes	OHHV	16	5.00	0.00	Fs/4
6	yes	BAROMETRIC_PRESSURE	16	5.00	0.00	Fs/4
7	yes	BA2mC	16	5.00	0.00	Fs/4

MODULE: gbu_J6_analog (KAM/ADC/005)

Index	Tx	Signal Name	Bits	Max	Min	Filter
0	yes	On_Off	16	5.00	0.00	Fs/4
1	yes	GENERATOR_POWER	16	10.00	-10.00	Fs/4
2	yes	PLC_BRAKE_M	16	10.00	0.00	Fs/4
3	yes	YAW_ANGLE	16	5.00	0.00	Fs/4
4	yes	AZIMUTH_ANGLE	16	10.00	0.00	32Fs
5	yes	ROTATIONAL_SPEED	16	10.00	0.00	Fs/4
6	no	SERI_TP	16	10.00	-10.00	Fs/4
7	yes	PLC_BRAKE_e	16	10.00	0.00	Fs/4

Table 1 of 2

CHASSIS: GBU (continued) FRAME SAMPLE RATE (EXPECTED): 50.02 Hz

MODULE: gbu_J7_analog (KAM/ADC/005)

Index	Tx	Signal Name	Bits	Max	Min	Filter
0	yes	BTNACC	16	5.00	0.00	Fs/4
1	yes	NACELLE_IMU_AX	16	5.00	0.00	Fs/4
2	yes	NACELLE_IMU_AY	16	5.00	0.00	Fs/4
3	yes	NACELLE_IMU_AZ	16	5.00	0.00	Fs/4
4	yes	NACELLE_IMU_RX	16	5.00	-5.00	Fs/4
5	yes	NACELLE_IMU_RY	16	5.00	-5.00	Fs/4
6	yes	NACELLE_IMU_RZ	16	5.00	-5.00	Fs/4
7	yes	LSS_SPEED	16	10.00	0.00	Fs/4

MODULE: gbu_J8_strain (KAM/ADC/009)

Index	Tx	Signal Name	Bits	Max	Min	Filter	ExVolt	ExOffset
0	yes	TOWER_BENDING_FA	16	0.010	-0.010	Fs/4	5.100	-0.511
1	no	gbu_J8_strain_1	16	0.010	-0.010	Fs/4	5.100	0.000
2	yes	TOWER_BENDING_SS	16	0.010	-0.010	Fs/4	5.100	0.081
3	no	gbu_J8_strain_3	16	0.010	-0.010	Fs/4	5.100	0.000
4	no	gbu_J8_strain_4	16	0.010	-0.010	Fs/4	5.100	0.000
5	no	gbu_J8_strain_5	16	0.010	-0.010	Fs/4	5.100	0.000
6	no	gbu_J8_strain_6	16	0.010	-0.010	Fs/4	5.100	0.000
7	no	gbu_J8_strain_7	16	0.010	-0.010	Fs/4	5.100	0.000

MODULE: gbu_J9_analog (KAM/ADC/005)

Index	Tx	Signal Name	Bits	Max	Min	Filter
0	yes	BAHHEC	16	5.00	0.00	Fs/4
1	yes	BAHHW_Sonic	16	5.00	0.00	Fs/4
2	yes	BARTC	16	5.00	0.00	Fs/4
3	yes	BARBC	16	5.00	0.00	Fs/4
4	no	gbu_J9_analog_0_4	16	5.00	0.00	Fs/4
5	no	gbu_J9_analog_0_5	16	5.00	0.00	Fs/4
6	no	gbu_J9_analog_0_6	16	5.00	0.00	Fs/4
7	no	gbu_J9_analog_0_7	16	10.00	0.00	Fs/4

MODULE: gbu_J10_uar2 (KAM/UAR/002)

Index	Tx	Signal Name
4	yes	TIME_GBU_GPS_Month_Day
6	yes	TIME_GBU_GPS_Year
8	yes	TIME_GBU_GPS_Hour_Minute
10	yes	TIME_GBU_GPS_Second
12	yes	TIME_GBU_GPS_Millisecond

Table 2 of 2

CHASSIS: ACRA_1 FRAME SAMPLE RATE (EXPECTED): 50.073 Hz

MODULE: ACRA__1_J2_enc (KAM/ENC/004)

Index	Tx	Signal Name	Bits	Value
0	yes	ACRA_1_J2_enc_0	16	12321
1..7	no	<empty>		

MODULE: ACRA_1_J3_strain (KAM/ADC/009)

Index	Tx	Signal Name	Bits	Max	Min	Filter	ExVolt	ExOffset
0	yes	B1_H1_Strain_0350_Z_HP	16	0.010	-0.010	Fs/4	5.100	1.166
1	yes	B1_H1_Strain_0350_Z_LP	16	0.010	-0.010	Fs/4	5.100	0.227
2	yes	B1_H1_Strain_2250_Z_HP	16	0.010	-0.010	Fs/4	5.100	0.000
3	yes	B1_H1_Strain_4500_Z_HP	16	0.010	-0.010	Fs/4	5.100	-0.300
4	yes	B1_H1_Strain_6750_Z_HP	16	0.010	-0.010	Fs/4	5.100	-0.300
5	yes	B1_H1_Strain_0350_Z_TE	16	0.010	-0.010	Fs/4	5.100	-2.000
6	yes	B1_H1_Strain_0350_Z_LE	16	0.010	-0.010	Fs/4	5.100	-0.300
7	no	empty	16	0.010	-0.010	Fs/4	5.100	0.000

MODULE: ACRA_1_J4_strain (KAM/ADC/009)

Index	Tx	Signal Name	Bits	Max	Min	Filter	ExVolt	ExOffset
0	yes	B2_H2_Strain_0350_Z_HP	16	0.010	-0.010	Fs/4	5.100	0.000
1	yes	B2_H2_Strain_0350_Z_LP	16	0.010	-0.010	Fs/4	5.100	0.000
2	yes	B2_H2_Strain_2250_Z_HP	16	0.010	-0.010	Fs/4	5.100	0.148
3	yes	B2_H2_Strain_4500_Z_HP	16	0.010	-0.010	Fs/4	5.100	0.297
4	yes	B2_H2_Strain_6750_Z_HP	16	0.010	-0.010	Fs/4	5.100	-0.241
5	yes	B2_H2_Strain_0350_Z_TE	16	0.010	-0.010	Fs/4	5.100	0.103
6	yes	B2_H2_Strain_0350_Z_LE	16	0.010	-0.010	Fs/4	5.100	0.247
7	no	empty	16	0.010	-0.010	Fs/4	5.100	0.000

MODULE: ACRA_1_J5_strain (KAM/ADC/009)

Index	Tx	Signal Name	Bits	Max	Min	Filter	ExVolt	ExOffset
0	yes	B3_H3_Strain_0350_Z_HP	16	0.010	-0.010	Fs/4	5.100	0.650
1	yes	B3_H3_Strain_0350_Z_LP	16	0.010	-0.010	Fs/4	5.100	0.390
2	yes	B3_H3_Strain_2250_Z_HP	16	0.010	-0.010	Fs/4	5.100	0.000
3	yes	B3_H3_Strain_4500_Z_HP	16	0.010	-0.010	Fs/4	5.100	0.057
4	yes	B3_H3_Strain_6750_Z_HP	16	0.010	-0.010	Fs/4	5.100	-0.481
5	yes	B3_H3_Strain_0350_Z_TE	16	0.010	-0.010	Fs/4	5.100	0.000
6	yes	B3_H3_Strain_0350_Z_LE	16	0.010	-0.010	Fs/4	5.100	0.320
7	no	empty	16	0.010	-0.010	Fs/4	5.100	0.000

MODULE: ACRA_1_J6_strain (KAM/ADC/009)

Index	Tx	Signal Name	Bits	Max	Min	Filter	ExVolt	ExOffset
0	yes	H1_Strain_Z_Flap	16	0.010	-0.010	Fs/4	5.100	1.000
1	yes	H1_Strain_Z_Edge	16	0.010	-0.010	Fs/4	5.100	0.000
2	yes	H2_Strain_Z_Flap	16	0.010	-0.010	Fs/4	5.100	0.000
3	yes	H2_Strain_Z_Edge	16	0.010	-0.010	Fs/4	5.100	0.000
4	yes	H3_Strain_Z_Flap	16	0.010	-0.010	Fs/4	5.100	0.000
5	yes	H3_Strain_Z_Edge	16	0.010	-0.010	Fs/4	5.100	0.000
6	no	empty	16	0.010	-0.010	Fs/4	5.100	0.000
7	no	empty	16	0.010	-0.010	Fs/4	5.100	0.000

Table 1 of 2

CHASSIS: ACRA_1 (continued) FRAME SAMPLE RATE (EXPECTED): 50.073 Hz

MODULE: ACRA_1_J7_analog (KAM/ADC/005)

Index	Tx	Signal Name	Bits	Max	Min	Filter
0	yes	B1_Motor1_Position	16	10.00	0.00	Fs/4
1	yes	B1_Motor1_Current	16	10.00	0.00	Fs/4
2	yes	B2_Motor1_Position	16	10.00	0.00	Fs/4
3	yes	B2_Motor1_Current	16	10.00	0.00	Fs/4
4	yes	B3_Motor1_Position	16	10.00	0.00	Fs/4
5	yes	B3_Motor1_Current	16	10.00	0.00	Fs/4
6	no	empty1	16	10.00	0.00	Fs/4
7	no	empty2	16	10.00	0.00	Fs/4

MODULE: ACRA_1_J8_analog (KAM/ADC/005)

Index	Tx	Signal Name	Bits	Max	Min	Filter
0	yes	B1_Motor2_Position	16	10.00	0.00	Fs/4
1	yes	B1_Motor2_Current	16	10.00	0.00	Fs/4
2	yes	B2_Motor2_Position	16	10.00	0.00	Fs/4
3	yes	B2_Motor2_Current	16	10.00	0.00	Fs/4
4	yes	B3_Motor2_Position	16	10.00	0.00	Fs/4
5	yes	B3_Motor2_Current	16	10.00	0.00	Fs/4
6	no	empty3	16	10.00	0.00	Fs/4
7	no	empty4	16	10.00	0.00	Fs/4

MODULE: ACRA_1_J9_analog (KAM/ADC/012)

Index	Tx	Signal Name	Bits	Max	Min	Filter
0	yes	B1_Motor3_Position	16	1.00	0.00	Fs/4
1	yes	B1_Motor3_Current	16	1.00	0.00	Fs/4
2	yes	B2_Motor3_Position	16	1.00	0.00	Fs/4
3	yes	B2_Motor3__Current	16	1.00	0.00	Fs/4
4	yes	B3_Motor3_Position	16	1.00	0.00	Fs/4
5	yes	B3_Motor3_Current	16	1.00	0.00	Fs/4
6	no	empty5	16	1.00	0.00	Fs/4
7	no	empty6	16	1.00	0.00	Fs/4
8	yes	Athena_AnalogOut1	16	1.00	0.00	Fs/4
9	yes	Athena_AnalogOut2	16	1.00	0.00	Fs/4
10	yes	Athena_AnalogOut3	16	1.00	0.00	Fs/4
11	yes	Cntrlbx_Extra1	16	1.00	0.00	Fs/4
12	yes	Cntrlbx_Extra2	16	1.00	0.00	Fs/4
13 .. 19	no	empty	16	1.00	0.00	Fs/4
20	yes	DAQ_IMU_X	16	1.00	0.00	Fs/4
21	yes	DAQ_IMU_Y	16	1.00	0.00	Fs/4
22	yes	DAQ_IMU_Z	16	1.00	0.00	Fs/4
23	yes	Impact_Hammer	16	1.00	0.00	Fs/4

MODULE: ACRA_1_J10_uar2 (KAM/UAR/002)

Index	Tx	Signal Name
4	yes	Time_GPS_Month_Day
6	yes	Time_GPS_Year
8	yes	Time_GPS_Hour_Minute
10	yes	Time_GPS_Second
12	yes	Time_GPS_Millisecond

Table 2 of 2

CHASSIS: cRIO_1 FRAME SAMPLE RATE (EXPECTED): 49.98 Hz

MODULE:		cRIO_1_J2_ctl (KAM/ENC/004)	
Index	**Tx**	**Signal Name**	**Chassis ID**
		cRIO_1_J2_ctl_Id_12345	12345

MODULE:		cRIO_1_J3_gps (RIO/SEA/GPS)
Index	**Tx**	**Signal Name**
0	yes	cRIO_1_J3_gps__Month-Day
1	yes	cRIO_1_J3_gps__Year
2	yes	cRIO_1_J3_gps__Hour-Minutes
3	yes	cRIO_1_J3_gps__Seconds
4	yes	cRIO_1_J3_gps__Milliseconds

MODULE:		cRIO_1_J4_analog (RIO/ADC/9239)						
Index	**Tx**	**Signal Name**	**Bits**	**Max**	**Min**	**Filter**	**Cutoff**	**Decimation**
0	yes	B1_H1_Accel_2000_X_HP	24	10.00	-10.00	Butterworth	Fs/4	Straight
1	yes	B1_H1_Accel_2000_Y_HP	24	10.00	-10.00	Butterworth	Fs/4	Straight
2	yes	B1_H1_Accel_2000_Z_HP	24	10.00	-10.00	Butterworth	Fs/4	Straight
3	yes	B1_H1_Accel_2000_X_TE	24	10.00	-10.00	Butterworth	Fs/4	Straight

MODULE:		cRIO_1_J5_analog (RIO/ADC/9239)						
Index	**Tx**	**Signal Name**	**Bits**	**Max**	**Min**	**Filter**	**Cutoff**	**Decimation**
0	yes	B1_H1_Accel_8000_X_HP	24	10.00	-10.00	Butterworth	Fs/4	Straight
1	yes	B1_H1_Accel_8000_Y_HP	24	10.00	-10.00	Butterworth	Fs/4	Straight
2	yes	B1_H1_Accel_8000_Z_HP	24	10.00	-10.00	Butterworth	Fs/4	Straight
3	yes	B1_H1_Accel_8000_X_TE	24	10.00	-10.00	Butterworth	Fs/4	Straight

MODULE:		cRIO_1_J6_analog (RIO/ADC/9239)						
Index	**Tx**	**Signal Name**	**Bits**	**Max**	**Min**	**Filter**	**Cutoff**	**Decimation**
0	yes	B2_H2_Accel_2000_X_HP	24	10.00	-10.00	Butterworth	Fs/4	Straight
1	yes	B2_H2_Accel_2000_Y_HP	24	10.00	-10.00	Butterworth	Fs/4	Straight
2	yes	B2_H2_Accel_2000_Z_HP	24	10.00	-10.00	Butterworth	Fs/4	Straight
3	yes	B2_H2_Accel_2000_X_TE	24	10.00	-10.00	Butterworth	Fs/4	Straight

MODULE:		cRIO_1_J7_analog (RIO/ADC/9239)						
Index	**Tx**	**Signal Name**	**Bits**	**Max**	**Min**	**Filter**	**Cutoff**	**Decimation**
0	yes	B2_H2_Accel_8000_X_HP	24	10.00	-10.00	Butterworth	Fs/4	Straight
1	yes	B2_H2_Accel_8000_Y_HP	24	10.00	-10.00	Butterworth	Fs/4	Straight
2	yes	B2_H2_Accel_8000_Z_HP	24	10.00	-10.00	Butterworth	Fs/4	Straight
3	yes	B2_H2_Accel_8000_X_TE	24	10.00	-10.00	Butterworth	Fs/4	Straight

Table 1 of 2

CHASSIS: cRIO_1 (continued) FRAME SAMPLE RATE (EXPECTED): 49.98 Hz

MODULE: cRIO_1_J8_analog (RIO/ADC/9239)

Index	Tx	Signal Name	Bits	Max	Min	Filter	Cutoff	Decimation
0	yes	B3_H3_Accel_2000_X_HP	24	10.00	-10.00	Butterworth	Fs/4	Straight
1	yes	B3_H3_Accel_2000_Y_HP	24	10.00	-10.00	Butterworth	Fs/4	Straight
2	yes	B3_H3_Accel_2000_Z_HP	24	10.00	-10.00	Butterworth	Fs/4	Straight
3	yes	B3_H3_Accel_2000_X_TE	24	10.00	-10.00	Butterworth	Fs/4	Straight

MODULE: cRIO_1_J9_analog (RIO/ADC/9239)

Index	Tx	Signal Name	Bits	Max	Min	Filter	Cutoff	Decimation
0	yes	B3_H3_Accel_8000_X_HP	24	10.00	-10.00	Butterworth	Fs/4	Straight
1	yes	B3_H3_Accel_8000_Y_HP	24	10.00	-10.00	Butterworth	Fs/4	Straight
2	yes	B3_H3_Accel_8000_Z_HP	24	10.00	-10.00	Butterworth	Fs/4	Straight
3	yes	B3_H3_Accel_8000_X_TE	24	10.00	-10.00	Butterworth	Fs/4	Straight

MODULE: cRIO_1_J10_analog (RIO/ADC/9205)

Index	Tx	Signal Name	Bits	Max	Min	Filter	Cutoff	Decimation
0	yes	B1_H1_Strain_0350_Z_HP	16	0.20	-0.20	Butterworth	Fs/4	Straight
1	yes	B1_H1_Strain_0350_Z_LP	16	0.20	-0.20	Butterworth	Fs/4	Straight
2	yes	B1_H1_Strain_2250_Z_HP	16	0.20	-0.20	Butterworth	Fs/4	Straight
3	yes	B1_H1_Strain_4500_Z_HP	16	0.20	-0.20	Butterworth	Fs/4	Straight
4	yes	B1_H1_Strain_6750_Z_HP	16	0.20	-0.20	Butterworth	Fs/4	Straight
5	yes	B1_H1_Strain_0350_Z_TE	16	0.20	-0.20	Butterworth	Fs/4	Straight
6	yes	B1_H1_Strain_0350_Z_LE	16	0.20	-0.20	Butterworth	Fs/4	Straight
7	no	empty1	16	5.00	-5.00	Butterworth	Fs/4	Straight
8	no	empty2	16	10.00	-10.00	Butterworth	Fs/4	Straight
9	no	empty3	16	10.00	-10.00	Butterworth	Fs/4	Straight
10	no	empty4	16	10.00	-10.00	Butterworth	Fs/4	Straight
11	no	empty5	16	10.00	-10.00	Butterworth	Fs/4	Straight
12	yes	DAQ_IMU_X_cRIO	16	10.00	-10.00	Butterworth	Fs/4	Straight
13	yes	DAQ_IMU_Y_cRIO	16	10.00	-10.00	Butterworth	Fs/4	Straight
14	yes	DAQ_IMU_Z_cRIO	16	10.00	-10.00	Butterworth	Fs/4	Straight
15	yes	Impact_Hammer_cRIO	16	10.00	-10.00	Butterworth	Fs/4	Straight

Table 2 of 2

DISTRIBUTION

1 Shreyas Ananthan c/o Ivette Gonzalez
Office of Wind and Water Power Technologies
EE-2B Forrestal Building, U.S. DOE
1000 Independence Ave. SW
Washington, DC 20585

1 Dale Berg
12421 Chelwood Trl NE
Albuquerque, NM 87112

1 Michael Derby c/o Ivette Gonzalez
Office of Wind and Water Power Technologies
EE-2B Forrestal Building, U.S. DOE
1000 Independence Ave. SW
Washington, DC 20585

1 Mark Higgins c/o Ivette Gonzalez
Office of Wind and Water Power Technologies
EE-2B Forrestal Building, U.S. DOE
1000 Independence Ave. SW
Washington, DC 20585

1 Jose Zayas c/o Ivette Gonzalez
Office of Wind and Water Power Technologies
EE-2B Forrestal Building, U.S. DOE
1000 Independence Ave. SW
Washington, DC 20585

1	MS0899	Technical Library	9536 (electronic copy)

Sandia National Laboratories